Multiscale Modeling of Defect Generation and Diffusion in Semiconductor Materials

Renyu Chen

A dissertation submitted in partial fulfillment
of the requirements for the degree of

Doctor of Philosophy

University of Washington

2012

Reading Committee:

Scott Dunham, Chair

Marjorie Olmstead

Manjeri Anantram

Program Authorized to Offer Degree:
Electrical Engineering

University of Washington

Abstract

Multiscale Modeling of Defect Generation and Diffusion in Semiconductor Materials

Renyu Chen

Chair of the Supervisory Committee:
Professor Scott T. Dunham
Electrical Engineering

As semiconductor device technology continues to evolve, great challenges arise in many areas. With the continuous shrinkage of the design window, a better understanding of the detailed physical processes that occur during fabrication is required. This dissertation utilizes the multiscale modeling approach to investigate such processes, focusing on the origin of these processes at the atomic scale and the collective behaviors over the large device scale.

In order to gain a fundamental understanding of the diffusion processes that occur during device fabrication, we have developed a kinetic lattice Monte Carlo (KLMC) simulator capable of simulating the self-/inter-/impurity diffusion processes. The findings demonstrate the great potential of KLMC in full scale simulation of strain and composition dependent diffusion processes in strained silicon and silicon-germanium devices.

The silicon photovoltaics industry is undergoing a continuous drive of cost reduction and efficiency improvement. The lack of fundamental understanding of the emitter deposition process poses challenges on process optimization. We have developed continuum models incorporating important physical processes during deposition, such as growth of phosphosilicate glass and transport of phosphorus across the glass

layer, and diffusion, deactivation and immobilization of phosphorus in silicon. We have simulated the diffused emitter profiles that agree well with experiments. The full modeling of the emitter deposition process allows process optimization to enhance efficiency and reduce cost.

Metals are detrimental defects in devices as they introduce traps that limit carrier lifetime. Modern devices require gettering processes to remove metals from active device region. We have built a model for the phosphorus diffusion gettering behavior of various metal species. Calculation results are in agreement with experimental gettering behavior and provide guidance on optimizing gettering efficiency for better device performance.

Lastly, we have extended our approach to wide band gap semiconductor β-Ga_2O_3, a potential candidate for future electronics devices. We have carried out *ab initio* calculations on the intrinsic vacancy and transition metal impurity defects in β-Ga_2O_3 and the results are in good agreement with experimental data. The theoretical analysis, combined with experimental observations, contributes to the fundamental understanding of nano-processes and electrical properties of β-Ga_2O_3.

ACKNOWLEDGMENTS

My debts are many as are my thanks. I count myself as very fortunate to have been working under the mentorship of my advisor Scott Dunham. His wisdom and amiability have made my doctoral studies a truly enriching and pleasant experience. Highly supportive of both my professional and personal needs, he has allowed me tremendous freedom to attend many conferences and workshops, arranging personal trips, and working off-campus in Canada and China. I have also reaped benefits from the encouragement and criticisms of other committee members. Special thanks to Marjorie Olmstead and Manjeri Anantram for their conscientious reading of my thesis and longtime support.

Many extraordinary colleagues in the nanotechnology modeling laboratory have given of their time, energy, and minds: thanks to Wenjun Jiang, Bart Trzynadlowski, Armin Yazdani, Haoyu Lai, Jason Guo, Baruch Feldman, Kjersti Kleven, Chihak Ahn and Zudian Qin.

I also wish to acknowledge the support of our collaborators that contribute to this thesis in various ways. They include a solar community in Germany (Pietro Altermatt, Hannes Wagner, Amir Dastgheib-Shirazi, and Michael Kessler) and the Heteroepitaxial Growth Group at the UW (Marjorie Olmstead, Fumio Ohuchi and Tracy Lovejoy). Part of the calculations and measurements were performed in the Enviromental Molecular Science Laboratory (EMSL), a user facility sponsored by the Department of Energy's Office of Biological and Environmental Research. Thanks to Dr. Zihua Zhu for performing the measurements and our enlightening conversations.

My doctoral projects have also been generously funded by Semiconductor Re-

search Corporation (SRC), Silicon Wafer Engineering and Defect Science (SiWEDS), Silicon Solar Consortium (SiSoc), Applied Materials, Sony Corporation, and Micron Technology Inc. Much appreciation goes to Intel and AMD for donating computing clusters, which were used for most of the calculations.

I have been blessed with many friends in Seattle during the past five years: Wenjun Jiang, Dawei Liu, Jie Liu, Dake Wang, Guilan Weng, Wei Zhang and Mingyuang Zhong. A big thank you to Hannes Wagner for his unparalleled hospitality when I was attending a workshop in Germany. The road trip with him in northern Germany was one of the most unforgettable memories in my Ph.D. years.

I owe a great debt of gratitude to my loving parents in China, Fayuan and Yalin. Finally, this and everything still to come go to my wife Minhao, whose wit and intelligence, love and care I could never fully repay.

TABLE OF CONTENTS

Page

List of Figures v

List of Tables x

Chapter 1: Introduction 1

Chapter 2: Simulation Methods 5
2.1 Density functional theory (DFT) 5
2.1.1 Formulation of DFT 5
2.1.2 Nuts and bolts of DFT 8
2.1.3 Applications of DFT 10
2.2 Kinetic Lattice Monte Carlo (KLMC) 11
2.2.1 Justification 12
2.2.2 Calculating rate constants 14
2.2.3 Picking transitions 14
2.2.4 Calculating residence time 15
2.3 Continuum modeling 16

Chapter 3: Correlation of Interstitial-Mediated Self-Diffusion in Si 18
3.1 Introduction 18
3.2 Simulation methods 21
3.3 Correlation factor of the "kick-out" mechanism 24
3.4 Correlation factor of the "stable-split" mechanism 26
3.5 Correlation factor of combined mechanisms in silicon 28
3.6 Conclusion 32

Chapter 4: Interdiffusion in SiGe alloys 33

4.1 Introduction 33
4.2 Model implementation 36
4.3 Stress analysis 38
4.4 KLMC simulations 39
4.5 Summary 46

Chapter 5: Phosphorus diffusion and deactivation in silicon 47
5.1 Introduction 47
5.2 Phosphorus-vacancy cluster model 50
5.2.1 DFT calculations 51
5.2.2 Continuum model 53
5.3 Interface trap model 55
5.4 Modeling of solid source diffusion of high phosphorus concentration diffusion 56

Chapter 6: $POCl_3$ emitter deposition process 59
6.1 Introduction 59
6.2 Experimental details 62
6.2.1 SIMS profiles of samples from the first set of samples 63
6.2.2 SIMS profiles of samples from the second set of samples 65
6.3 Analyzing SIMS data 68
6.3.1 Layer identification 68
6.3.2 Temperature dependence 69
6.3.3 Varying O_2 flow rates 69
6.3.4 Comparing drive-in under N_2 and O_2 ambients 70
6.3.5 Quantitative analysis 70
6.4 Model implementation 72
6.5 Coupling with phosphorus diffusion and deactivation models in Si . . 80
6.6 Summary 80

Chapter 7: Diffusion and gettering of metal species 82
7.1 Introduction 82
7.2 Numerical details 84
7.3 Favorable configurations and electric levels 84

7.4 Phosphorus diffusion gettering of metal species 85
7.4.1 Gettering behavior under phosphorus implants 86

Chapter 8: Intrinsic defects and impurities in β-Ga_2O_3 89
8.1 Introduction 89
8.2 β-Ga_2O_3 crystal structure 89
8.3 Numerical details 90
8.4 Intrinsic point defects in β-Ga_2O_3 91
8.5 Transition metal impurities in β-Ga_2O_3 96

Chapter 9: Summary and future directions 100
9.1 Summary 100
9.1.1 KLMC simulations of self-diffusion and interdiffusion in Si . . 100
9.1.2 DFT calculations of life-time limiting defects in Si 101
9.1.3 Numerical models for coupled PSG growth and P diffusion in $POCl_3$ diffusion process 101
9.1.4 DFT calculations of intrinsic and metal impurities in β-Ga_2O_3 101
9.2 Suggestions for future work 102
9.2.1 Kinetic lattice Monte Carlo process simulations 102
9.2.2 Phosphorus deactivation and gettering of metals 102
9.2.3 $POCl_3$ emitter diffusion 102
9.2.4 Impurities in β-Ga_2O_3 103
9.3 Final conclusion 103

Appendix A: KLMC simulator LAMOCA 104
A.1 Simulation Domain 104
A.2 Numerical Details 105

Appendix B: 5-stream pair-diffusion model 108
B.1 Model species 108
B.2 Assumptions 109
B.3 Definition of some terms 110
B.3.1 Carrier concentration 110
B.3.2 Point defect property χ_I and χ_V 110

B.3.3 Dopant-defect pair property $\pi_{\rm I}$ and $\pi_{\rm V}$ 110
B.4 Determination of flux terms 112
B.4.1 Flux of point defects 112
B.4.2 Flux of impurity-defect pairs 112
B.5 Reaction rates 113
B.5.1 $\mathrm{P}^{+} + \mathrm{X}^{i-1} \Longleftrightarrow (\mathrm{PX})^{i}$ 113
B.5.2 $\mathrm{I}^{i} + \mathrm{V}^{j} \Longleftrightarrow (i+j)h^{+}$ 113
B.5.3 $(\mathrm{PI})^{i} + \mathrm{V}^{j} \Longleftrightarrow \mathrm{P}^{+} + (i+j-1)h^{+}$ 113

Bibliography 114

LIST OF FIGURES

Figure Number Page

1.1 Multiscale modeling and simulation hierarchy. 2

1.2 Exponential chip density growth in Si technology, also known as Moore's law. Source: Gordon Moore's presentation at International Solid State Circuits Conference (ISSCC), February 10, 2003. 2

1.3 Historical plot of crystalline silicon solar cell module price showing classic experience curve behavior [1]. 3

2.1 Flowchart of the KLMC simulations. 13

2.2 A typical trajectory featuring state-to-state transitions and vibrations in the vicinity of the energy valley. 13

2.3 Energy barriers of state 1 to state 2, and vice versa. 15

3.1 Vacancy- and interstitial-mediated self-diffusion mechanisms on a 2D square lattice. 19

3.2 Correlation effects for vacancy- and interstitial-mediated self-diffusion mechanisms on a 2D square lattice. The tracer atom is denoted as blue spheres, and vacancy is the dashed empty circle. The green atom are normal silicon atoms. 20

3.3 Difference of a tracer atom and an interstitial atom in an direct diffusion hop. 22

3.4 Schematics of the "kick-out" mechanism in the (a) tetrahedral network, and (b) hexagonal network. t_0 and h_0 denote the incoming tracer. The center atom is the silicon atom being kicked out. For tetrahedral configurations t_{1-3} (red/dark spheres) are equivalent, while for hexagonal configurations, the neighbors can be divided into 3 groups: $h_{1,2}$ (red/dark, large spheres), $h_{3,4}$ (blue/dark, medium spheres), and h_{5-8} (brown/dark, small spheres). The other h sites (grey/light, medium spheres) are excluded. 25

3.5 Allowed hopping directions in the (a) split-tetrahedral and (b) split-hexagonal networks, viewed along the $\langle 1\bar{1}0 \rangle$ direction. a and b form the $\langle 110 \rangle$-split interstitial. c is the original lattice site. In (a) the small spheres denote the 4 first nearest tetrahedral neighbors of the split categorized into 2 groups, 2 in t_A and 2 in t_B. The allowed hopping destinations of the split are the 2 t_B sites only. In (b) the small spheres denote the 12 first nearest hexagonal neighbors of the split categorized into 4 groups, 2 in h_A, 4 in h_B, 4 in h_C and 2 in h_D. The allowed hopping destinations of the split are the 4 h_C sites only. Note that some nearest neighbors behind are blocked by the ones in front of them, when viewed along this direction. 27
3.6 Migration energy of different migration paths of self-interstitial diffusion in silicon. 30
3.7 Effective correlation factors of interstitial-mediated self-diffusion in silicon as a function of the probability of hopping via the direct mechanism. 31

4.1 TEM micrograph of a 45-nm p-type MOSFET. [2] 34
4.2 Cross-sectional TEM image of a Si-Ge interface annealed at 900 °C for 30 min. [3] 35
4.3 Energy profiles of the transitions. V_{tr} and GeV_{tr} denote the transition states for transition 4.2 and 4.3 respectively. 37
4.4 Schematic of simulation domain, with random alloy arrangement of 20% Ge. Ge fraction plot adapted from Ref [4]. 40
4.5 Concentration profiles as functions of the normalization factor, η, for vacancy-mediated SiGe interdiffusion with and without consideration of the stress effect. The results are obtained for temperature equal to 920 °C. "+"s are original data and lines are fitted curves. 44
4.6 Interdiffusivity values (symbols) extracted from Figure 4.5 and fittings (dashed lines) to Eq. (4.25) for pure alloy effect (w/o stress) and alloy effect combined with stress effect (w/stress) of Ge in the system. The results are obtained for a temperature of 920 °C. 45

5.1 Simulated phosphorus solid state diffusion profiles using the pair-diffusion model fitted against experimental data, from Ref. [5]. 48
5.2 Schematic of the sputtering of sample surface by a primary beam during SIMS measurements, from Ref. [6]. 50
5.3 Schematic of a P_4V cluster containing 4 phosphorus atoms (pink/dark) and a vacancy (grey/light). 51

5.4 Equilibrium substitutional phosphorus P_S (active) concentration and P_4V (inactive) concentration as functions of the total phosphorus concentration at 840 °C. The concentrations of P_nV with $n \leq 3$ are negligible and fall out of the plotting range. 54
5.5 Illustration of the trapping process in the interface trap region. 55
5.6 Simulation (lines) of the ECV profile (electrically active phosphorus) and the SIMS profile (total phosphorus) as compared to the experimental data (symbols) from University of Hannover. 58
5.7 Simulation of the time dependence of P dose as active, clustered, trapped species. 58

6.1 Schematic of a solar cell in operation. [7] 61
6.2 $POCl_3$ predeposition in an open tube furnace with a bubbler set-up. [8] 61
6.3 SIMS profiles of ^{28}Si, ^{31}P, and ^{18}O ions for varying predeposition and drive-in temperatures. 63
6.4 SIMS profiles of ^{28}Si, ^{31}P, and ^{18}O ions for varying O_2 flow rates. . . 64
6.5 SIMS profiles of ^{28}Si, ^{31}P, and ^{18}O ions for varying drive-in times under N_2 ambient. 64
6.6 SIMS profiles of ^{28}Si, ^{31}P, and ^{18}O ions for varying drive-in times under O_2 ambient. 65
6.7 ToF-SIMS profiles of ^{28}Si, ^{31}P, and ^{18}O ions for varying $POCl_3$ flow rates at a predeposition time of 10 min. 66
6.8 ToF-SIMS profiles of ^{28}Si, ^{31}P, and ^{18}O ions for varying $POCl_3$ flow rates at a predeposition time of 20 min. 67
6.9 ToF-SIMS profiles of ^{28}Si, ^{31}P, and ^{18}O ions for varying $POCl_3$ flow rates at a predeposition time of 40 min. 67
6.10 SIMS profiles of ^{28}Si, ^{31}P, and ^{18}O ions for $POCl_3$ flow rate of 500 sccm and predep time of 40 min. The two interfaces are determined by deconvolution of SIMS profiles. The systematic decrease of the profiles towards the surface is due to the SIMS transient artifacts. 69
6.11 Matching SIMS data with ECV data for several different flow and predep time conditions. The two profiles were matched in the concentration regions of 1×10^{19} cm^{-3} to 2×10^{20} cm^{-3}. Left: predeposition times of 10, 20 and 40 min with a flow rate of 250 sccm. Right: Flow rates of 250, 500, and 1000 sccm with a predeposition time of 10 min. 71

6.12 Growth of (a) PSG thickness, (b) total P dose in Si, and (c) SiO_2 thickness under different $POCl_3$ flow rates, as extracted from Figures 6.7, 6.8, 6.9 and 6.11. The data point for flow rate of 250 sccm and 10 min in (c) has large uncertainty as a result of uncertainties in the interface locations due to low dose. Solid lines are a guide to the eyes. 72

6.13 Model schematic with critical concentrations at interfaces. Subscripts denote atom species, and superscripts denote the associated regions (G stands for PSG and X stands for oxide). An apostrophe in the subscript is added to distinguish the concentration at the bottom interface from that at the top. Arrows denote the net flows of P (brown) and O (blue). J_D, J_S, and J_R denote fluxes of diffusion, segregation and reaction respectively. 73

6.14 Growth of PSG thickness and phosphorus dose under different $POCl_3$ flow rates. Points: data from SIMS, dashed lines: fit from the simple linear-parabolic model, solid lines: fit from the improved model. . . . 78

6.15 Comparison between simulated (lines) and experimental values measured by ECV (symbols) of phosphorus profiles for a $POCl_3$ flow rate of 250 sccm and deposition times of 10, 20, 40 min. 81

7.1 Periodic table including the transition metals included in this study (shaded). 84

7.2 SIMS depth profiles of silicon wafers implanted with phosphorous followed by annealing [9]. 87

8.1 20 atom unit cell of β-Ga_2O_3 (twice the primitive cell) showing two distinct gallium sites (big, green spheres) and three distinct oxygen sites (small, red spheres). 90

8.2 Formation energy of vacancy defects Ga-rich and O-rich conditions as a function of Fermi level. The slope of a given line segment corresponds to the charge state. 95

8.3 DFT:GGA band structure plot for relaxed, neutral, 40-atom cell of undefected β-Ga_2O_3. Filled states are shown in green dots (lighter) and unfilled states in red dots (darker). 98

8.4 DFT:GGA band structure plot for relaxed, neutral, 40-atom cell of β-Ga_2O_3 with one Cr replacing an octahedral Ga . Filled states are shown in green dots (lighter) and unfilled states in red dots (darker). 98

8.5 Energy band diagram of β-Ga_2O_3 under Cr or Mn doping. 99

A.1 Illustration of the augmented lattice sites in the silicon conventional unit cell. A substitutional site (light/yellow) is simply the silicon lattice site. A tetrahedral site (dark/red, upper left) is at the center of a tetrahedron formed by four substitutional sites. A hexagonal site (dark/brown, right) is at the center of a hexagonal ring formed by six substitutional sites. A bond-centered site (dark/blue, lower left) is at the center of a Si-Si bond. Reduced lattice coordinates for typical substitutional, tetrahedral, hexagonal, and bond-centered sites are (0, 0, 0), (1/4, 1/4, 3/4), (5/8, 3/8, 3/8), and (1/8, 1/8, 1/8), respectively. . 105

A.2 Change of migration barrier due to change of formation energies of initial and final states. 107

LIST OF TABLES

Table Number | Page

3.1 Correlation factors for the "kick-out" mechanism in the tetrahedral and hexagonal hopping networks. The mechanism in the hexagonal network is categorized into 3 groups based on the kick-out direction. The brackets denote the corresponding destinations after the kick-out. The $\overline{\cos\theta}^I$ value is fixed for each mechanism, and the $\overline{\cos\theta}^{tr}$ value is calculated from the KLMC approach. The uncertainty of the correlation factor is the standard error of the mean. 26

3.2 Correlation factor values for the tetrahedral and hexagonal hopping networks. The $\overline{\cos\theta}^I$ value is calculated analytically, and the $\overline{\cos\theta}^{tr}$ value is calculated via the KLMC approach. The uncertainty of the correlation factor is the standard error of the mean. 28

3.3 Migration barriers of various migration paths of self-interstitials in silicon. 29

4.1 DFT parameters for V mediated interdiffusion. 36

4.2 Induced strain vectors of point defects/impurities which are associated with the energies of the initial and the final states of a hop. 38

4.3 Fitted values of B in exponential model for SiGe interdiffusion due to different effects of Ge concentration. 45

5.1 Formation and binding energy of P_nV clusters. Formation energy is referenced to neutral and substitutional phosphorus. Binding energy of P_nV is calculated against isolated $P_{n-1}V$ and substitutional phosphorus. 52

6.1 Determination of partial pressure from gas flow rates. 66

6.2 Definition and values of lumped parameters for the simple and improved models obtained by fitting the experimental data via the least square method. The simple model has 3 lumped parameters: K_0, K_1, and K_2. The improved model has 3 additional parameters: K_3, K_4, and K_5. H_P and H_O are Henry constants associated with $POCl_3$ and O_2 respectively. The phosphorus and oxygen concentration at the top PSG surface is calculated as $C_P^G = H_P\ p_{\mathrm{POCl_3}}$, $C_O^G = H_O\ p_{\mathrm{O_2}}$, where p denotes the partial pressure (in atm) of the gases. k_P^R is the equilibrium constants for the reaction at the PSG-SiO_2 interface as defined in Eq. (6.5), and k_O^R is the corresponding constant for oxygen. r_P^{S1} and r_P^{S2} are segregation coefficients of P at the PSG-SiO_2 and SiO_2-Si interfaces respectively. Diffusivities are denoted by D, with subscript indicating species (P, O) and superscript indicating region (G stands for PSG and X stands for oxide). x_X is the thickness of the oxide (treated as a fixed parameter). λ is the ratio of the P dose in Si to the peak P concentration in Si. N_P is the number of P atoms incorporated per unit volume of PSG grown, with a value of 6.5×10^{21} cm^{-3} extracted from our RBS measurements. 77

7.1 Calculated deep transition levels of the metal interstitials in comparison with experimental values (unit: eV). d, dd, and a denote donor, double donor, and acceptor levels respectively. Donor levels are referenced to the valence band maximum and acceptor levels are referenced to the condution band minimum. 86

7.2 Binding energy of metals to various phosphorus species (unit: eV). When a metal binds with a P_nV cluster, it occupies the vacancy site. The values are referenced to isolated tetrahedral metal and neutral phosphorus species. Negative values indicate binding, while positive values indicate repulsion. 87

7.3 Comparison of binding to P_4V and dislocation cores for various metal species (unit: eV). Calculations of binding to dislocation cores were done by Bart Trzynadlowski. 88

8.1 Gallium and oxygen chemical potentials under extreme Ga-rich and O-rich conditions. 93

A.1 The augmented lattice sites and their numbers per unit cell. 104

A.2 The augmented lattice sites and their numbers per unit cell. 106

B.1 Species in the 5-stream model. 108

Chapter 1

INTRODUCTION

Modern semiconductor industry relies on fabrication techniques to turn silicon into functional devices. Due to the growing cost of experimental-based R&D as devices become more complicated, computational modeling and simulation is playing an increasingly important role in technology advancement, especially in microelectronics and photovoltaics industries. There are a wide variety of modeling and simulation techniques, with varying spatial and temporal scales. Common continuum process and device simulation techniques, also known as TCAD (technology computer aided design), is a very powerful method to study process and device physics at the macroscopic level, but it sacrifices all atomic details. On the other hand, *ab initio* approaches such as the density functional theory (DFT) solves fundamental quantum many-body equations and provide theoretical basis for higher level models. Bridging the gap between the above two approaches, molecular dynamics (MD) and kinetic lattice Monte Carlo (KLMC) focus on nano-scale processes and at the same time can simulate dynamic processes at an extended time-scale. This dissertation adopts the so-called *multiscale modeling and simulation* approach, combining all available modeling techniques together to achieve comprehensive understandings of processes from the atomic scale to the device scale. Figure 1.1 illustrates the multiscale modeling and simulation hierarchy. For a brief introduction of all the multiscale modeling and simulation approaches, see Chapter 2.

Ever since the invention of the first integrated circuit, the silicon microelectronics industry has been growing exponentially. The continuous technology improvement has followed the empirical observation of Moore's Law (Figure 1.2), which states that

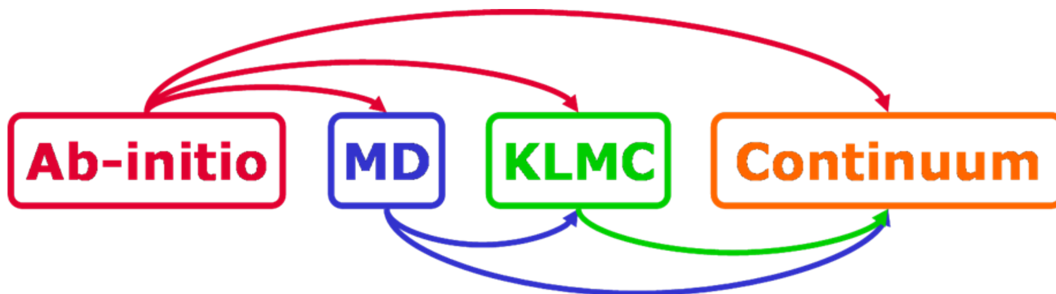

Figure 1.1: Multiscale modeling and simulation hierarchy.

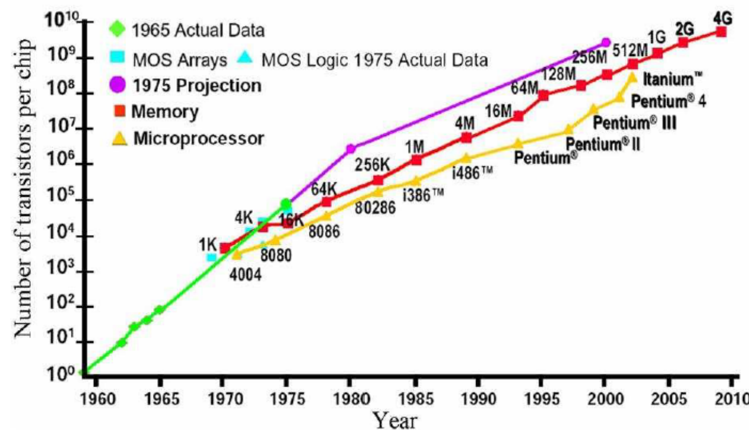

Figure 1.2: Exponential chip density growth in Si technology, also known as Moore's law. Source: Gordon Moore's presentation at International Solid State Circuits Conference (ISSCC), February 10, 2003.

the number of transistors that can be placed on an integrated circuit doubles every 18 months. In 2011, Intel announced its first microprocessor "Ivy Bridge" using the 3-D Tri-Gate Transistor Technology [10]. This breakthrough has lead industry into the sub-22 nm regime, with chips featuring unprecedented performance improvement and power reduction.

The development of the microelectronics industry has benefited the silicon photovoltaics industry, resulting in a continuous drive of lower cost and higher efficiency.

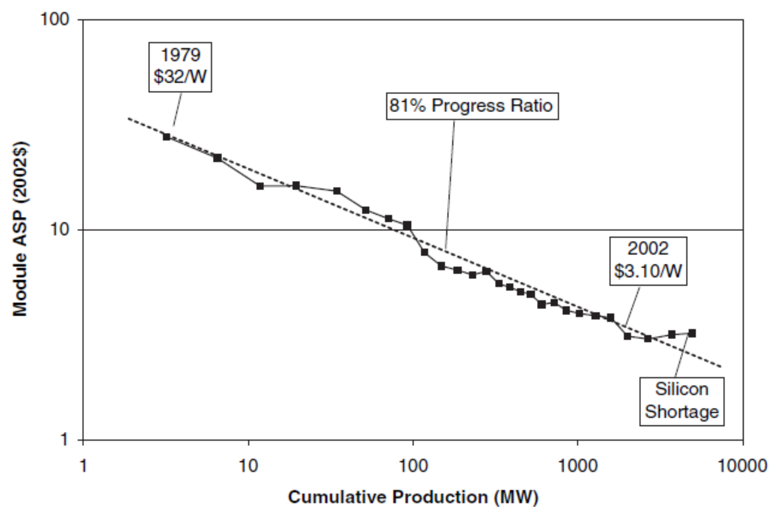

Figure 1.3: Historical plot of crystalline silicon solar cell module price showing classic experience curve behavior [1].

Even today, silicon still dominates the photovoltaics technology, with a more than 85% market share. It is estimated that crystalline silicon solar cells are likely to continue to advance in both efficiency enhancement and cost reduction for the next two decades.

Modern silicon-based devices commonly undergo a series of fabrication processes. A key question for both microelectronics and silicon photovoltaics is: how do fabrication processes affect the distribution of various atomic and molecular species, including intentional dopants and unintentional contaminants? These species have a profound impact on the device performance. Dopants such as phosphorus and boron control the electrical property of the active device region. Germanium introduces strain that can enhance channel mobility of transistors. Lifetime limiting defects such as metals can degrade device performance if their concentrations are not well controlled. A thorough understanding of how fabrication processes affect the distribution of these atom species provides a link between process recipe and device characteristics, and is thus crucial for process design optimization. In Chapters 3 and 4, we

have combined DFT and KLMC approaches to address several aspects of self-diffusion and inter-diffusion processes, which contributes to understanding the atomistic fundamentals of the diffusion processes in strained silicon and silicon germanium devices. In Chapter 5, we have performed DFT calculations and built continuum models for the phosphorus diffusion gettering behaviors of various metal species. The calculation and simulation results provide useful insights on the optimization of gettering efficiency for better device performance. In Chapters 6 and 7, we have built a set of continuum models for the $POCl_3$ doping process, a common method for n-type emitter formation of crystalline silicon solar cells. These models include critical processes during deposition such as phosphosilicate glass (PSG) layer formation, diffusion of phosphorus in PSG and silicon, and deactivation and immobilization of phosphorus in silicon. The models were calibrated against experimental data and can be used to predict the diffused emitter profiles under various doping conditions.

While silicon still dominates the semiconductor industry, it is necessary to explore novel semiconductor materials that may be incorporated into traditional Si-based devices to achieve better device performance. Wide band gap semiconductors, with many superior electronic, magnetic, and optical properties, show great potential in future generation semiconductor devices. β-Ga_2O_3, with a large band gap and thermal stability up to its melting point, has attracted wide interests. However, there still exist many puzzles regarding the basic nano-processes in the material. In Chapter 8 we have performed DFT calculations on the properties of intrinsic vacancies and transition metal impurities in β-Ga_2O_3. The DFT results agree well with experimental observations and contribute to the fundamental understandings of nano-processes and electrical properties of β-Ga_2O_3.

Chapter 2

SIMULATION METHODS

2.1 Density functional theory (DFT)

Density functional theory is a widely used approach in physics and materials science to attack the many-electron problem in solids and molecules. It provides a systematic way to calculate from first principles (*ab initio*) the properties of materials on the atomic scale. Here we briefly go through the basic formulation of DFT. A thorough discussion of DFT can be found in various review papers and books [11, 12].

2.1.1 Formulation of DFT

2.1.1.1 Born-Oppenheimer approximation

To fundamentally understand material properties we need to solve the time-independent Schrödinger equation

$$H\Psi = E\Psi \tag{2.1}$$

where H and Ψ are the Hamiltonian and wavefunction of all particles in the system including electrons and nuclei. Solving this equation exactly is formidable, since we are dealing with a degree of freedom on the order of 10^{23}. Therefore, approximations are needed. The first approximation applied is the Born-Oppenheimer approximation, which considers the fact that the electrons are much lighter than nuclei and thus move much faster. Thus, electrons can be thought of as following the motion of the nuclei instantaneously, while always retaining in the same stationary state of the electronic Hamiltonian. We can thus separate the wavefunction into a nucleus part and an

electron part

$$\Psi(\mathbf{R},\mathbf{r}) = \Psi_n(\mathbf{R})\psi_e(\mathbf{R},\mathbf{r}) \tag{2.2}$$

and the Schrödinger equation can be transformed into a simple one where only electron coordinates are involved

$$H_e\psi_e(\mathbf{R},\mathbf{r}) = E_e(\mathbf{R})\psi_e(\mathbf{R},\mathbf{r}) \tag{2.3}$$

The Hamiltonian of N electrons is

$$H_e = -\sum_{i=1}^{N}\frac{\hbar^2}{2m}\nabla_i^2 + \sum_{i=1}^{N}V_{ext}(\mathbf{r}_i) + \frac{1}{2}\sum_{i\neq j=1}^{N}\frac{e^2}{|\mathbf{r}_i - \mathbf{r}_j|} \tag{2.4}$$

The three terms are kinetic energy, nuclear potential energy, and electron-electron potential energy operators respectively. The nuclear potential energy is a superposition of all the M positive ions

$$V_{ext}(\mathbf{r}) = \sum_{k=1}^{M}\frac{Z_k}{|\mathbf{R}_k - \mathbf{r}|} \tag{2.5}$$

2.1.1.2 Electron Density–Kohn Sham Theory

Density functional theory is based on the Hohenberg-Kohn theorem which states that

1. The ground state density uniquely determines all properties of the system, i.e. system energy is a *functional* of density,

2. The true ground state density minimizes the energy functional.

Based on these conclusions, we can write the energy functional as

$$E[\rho(\mathbf{r})] = T_0[\rho(\mathbf{r})] + \int V(\mathbf{r})\rho(\mathbf{r})d\mathbf{r} + \frac{1}{2}\int\int\frac{\rho(\mathbf{r})\rho(\mathbf{r}')}{|\mathbf{r} - \mathbf{r}'|}d\mathbf{r}d\mathbf{r}' + E_{xc}[\rho(\mathbf{r})] \tag{2.6}$$

where the first three terms on the right hand side are the kinetic energy of a non-interacting electron gas that has the same density as the system we are solving, the

potential energy term, and the classical electron-electron Coulomb interaction term (also known as the Hartree term). The extra energy caused by correlation effects are all lumped into the last term, i.e. the exchange-correlation energy.

By applying the variation principle, we can reduce the many-electron problem to a single-electron Schrödinger equation, known as the Kohn-Sham equation

$$\left[-\frac{\hbar^2}{2m}\nabla^2 + V_{eff}(\mathbf{r})\right]\phi_i(\mathbf{r}) = \epsilon_i\phi_i(\mathbf{r}) \tag{2.7}$$

where the effective potential is defined as

$$V_{eff}(\mathbf{r}) = V_{ext}(\mathbf{r}) + \int \frac{\rho(\mathbf{r}')}{|\mathbf{r}-\mathbf{r}'|}d\mathbf{r}' + \frac{\delta E_{xc}[\rho(\mathbf{r})]}{\delta\rho(\mathbf{r})} \tag{2.8}$$

with the density given by:

$$\rho(\mathbf{r}) = \sum_{i=1}^{N}|\phi_i(\mathbf{r})|^2 \tag{2.9}$$

With a given form of exchange correlation potential, the Kohn-Sham equation can be solved self-consistently.

2.1.1.3 Exchange correlation functionals

The success of the equations above depends on the choice of exchange-correlation functionals. During the past years, many choices have been proposed. The simplest one is the local density approximation (LDA), which assumes that the exchange-correlation energy density, ϵ_{xc}, depends solely upon the value of the electronic density ρ at each point. This leads to

$$E_{xc}[\rho(\mathbf{r})] = \int \epsilon_{xc}(\rho(\mathbf{r}))\rho(\mathbf{r})d\mathbf{r}$$

Another approach is the general gradient approximation (GGA), which assumes

that ϵ_{xc} is also dependent on the gradient of density.

$$E_{xc}[\rho(\mathbf{r})] = \int \epsilon_{xc}(\rho(\mathbf{r}), \nabla\rho(\mathbf{r}))\rho(\mathbf{r})d\mathbf{r}$$

These two forms can be directly plugged in to the variation formula to get the expressions for the exchange correlation potential:

$$V_{xc}(\mathbf{r}) = \frac{\delta E_{xc}[\rho(\mathbf{r})]}{\delta\rho(\mathbf{r})} = \begin{cases} \epsilon_{xc}(\rho) + \rho \cdot \frac{\partial\epsilon_{xc}(\rho)}{\partial\rho}, & \text{LDA} \\ \epsilon_{xc}(\rho) + \rho \cdot \frac{\partial\epsilon_{xc}(\rho,\nabla\rho)}{\partial\rho} - \nabla \cdot \left(\rho\frac{\partial\epsilon_{xc}(\rho,\nabla\rho)}{\partial\nabla\rho}\right), & \text{GGA} \end{cases}$$

2.1.2 Nuts and bolts of DFT

In DFT, the Kohn-Sham single electron Schrodinger equation should be solved self-consistently to find the ground state of a system. There are many different DFT codes available. Depending on the basis sets used to describe electronic wave functions, they can be categorized into two major groups: plane-wave basis sets and local basis sets. The former is often suitable for calculations of solids while the latter is mostly used in studying molecules. In plane-wave basis calculations, the core electrons are treated as part of the ions in order to achieve basis-set convergence with a practical number of basis functions, and the electron-ion interactions are described by pseudopotentials. In our study, we use the plane-wave basis code VASP (Vienna Ab-initio Simulation Package) [13, 14, 15, 16] for all DFT calculations.

In order to obtain sensible results, convergence tests have to be carried out with respect to the supercell size, energy cut-off, and k-point sampling.

2.1.2.1 Supercell size

Plane-wave basis methods use the periodic supercell structure. Therefore, the system under consideration is a three-dimensional periodic array of the unit cell. The size of the supercell should be large enough so that the defect in the unit cell does not interact

with its neighboring images. For example, we use a 64-atom cell for all calculations in Si.

2.1.2.2 *Energy cut-off*

The energy cut-off determines the number of plane waves used for the expansion. The cut-off value should be large enough to maintain the accuracy of the calculations, however the larger its value, the longer the calculation time. The required value of the energy cut-off depends on the constituent atomic species of the structure under the calculation. Generally, smaller atoms require a larger energy cut-off. A reasonable value the energy cut-off would be the maximum `ENMAX` value of constituent atomic species (`ENMAX` is specified in the POTCAR file of each atom species). In our studies, the energy cutoff has been chosen through convergence tests such that the change of total energy differences is within 0.02 eV. For example, we use values of 320 eV for phosphorus-related defects in silicon and 400 eV for Ga_2O_3. The energy cut-off for Ga_2O_3 is much larger due to the oxygen involved in the calculations. It is suggested in the VASP manual to specify the cut-off manually and keep it constant throughout a set of calculations [17].

2.1.2.3 *k-point sampling*

In order to perform integrations over the Brillioun zone, a set of sampling points in the reciprocal space should be specified. A starting point is to use only the Γ point as the sample point. More k-points lead to more accurate results, but place larger demand on memory and CPU time. The Monkhorst-Pack sampling scheme is an efficient scheme to generate an array of k-points in the reciprocal space [18]. The distribution of k-points is suggested to be even over the three dimensions of the Brillioun zone [17]. For calculations in silicon, we use a $2 \times 2 \times 2$ mesh of Monkhorst-Pack k-points.

A well known limitation of DFT is its systematic underestimation of the band gap of a given material. For example, GGA gives a Si band-gap of 0.59 eV, much smaller

than the experimental value of 1.12 eV. For β-Ga_2O_3 GGA predicts a value of 2.13 eV, while the experimental value is 4.9 eV. Special care much be taken when the band gap error possibly enters the calculated energies (See Chapters 7 and 8).

2.1.3 Applications of DFT

2.1.3.1 Calculating formation energy

DFT can be used to calculate the formation energy of a given defect configuration. For example, the formation energy of a neutral vacancy or interstitial in silicon can be calculated as

$$\begin{aligned} E_f[\mathrm{I}^0, \mathrm{V}^0] &= E_{tot}[\mathrm{I}^0, \mathrm{V}^0] - E_{tot}[\mathrm{bulk}] \pm \frac{1}{N} E_{tot}[\mathrm{bulk}] \\ &= E_{tot}[\mathrm{I}^0, \mathrm{V}^0] - \frac{N \pm 1}{N} E_{tot}[\mathrm{bulk}] \end{aligned} \tag{2.10}$$

where plus and minus corresponds to interstitial and vacancy respectively. $E_{tot}[\mathrm{I}^0, \mathrm{V}^0]$ is the calculated total energy for the supercell containing the vacancy (interstitial), and $E_{tot}[\mathrm{bulk}]$ is the calculated total energy for the supercell of the perfect bulk structure.

For impurities in silicon, the formation energy is usually referenced to the lowest energy configuration of the constituent species. For example, the formation energy of a carbon-pair is defined relative to the substitutional carbon in silicon

$$E_f[\mathrm{CV}^0] = E_{tot}[\mathrm{CV}^0] - E_{tot}[\mathrm{C}_\mathrm{S}^0] - \frac{1}{N} E_{tot}[\mathrm{bulk}] \tag{2.11}$$

The formation energy can be directly related to the stability of the defect configuration. The higher the formation energy, the more energy cost to form the defect, and thus the less stable the defect configuration.

2.1.3.2 Calculating migration energy

DFT can also be used to identify transition events and calculate the associated migration barriers. This is done by the nudged elastic band (NEB) method [19, 20] implemented in VASP. Given an initial and final state, a set of intermediate configurations are obtained by linear interpolation of the two end points. This forms a string of states, and energy is optimized along the direction perpendicular to the string. This technique is efficient in finding the energy paths and identifying transition state of the migration.

2.2 Kinetic Lattice Monte Carlo (KLMC)

Kinetic Monte Carlo is a method for the atomic-scale simulation of dynamical processes, such as diffusion, deposition, clustering and dissociation. A common approach in simulating this class of processes is molecular dynamics (MD), in which the system trajectories are determined by numerically integrating Newton's equations of motion of all particles. However, in order to give an accurate description of system trajectories, the time integration step should be on the order of 1 picosecond, the characteristic time-scale of atomic vibrations, or even less. The total simulation time is thus usually limited to less than one microsecond, far less than the time-scale of practical dynamical processes such as diffusion. This time-scale problem is the inherent limitation of molecular dynamics.

In contrast to MD, the kinetic Monte Carlo (KMC) approach ignores atomic vibrations and treats diffusion as stochastic transitions between locally metastable states. As these state-to-state transitions are rare events that happen at a much larger time-scale than atomic vibrations, KMC is capable of simulating practical processes at much longer time scales, usually on the order of seconds and beyond.

Kinetic lattice Monte Carlo (KLMC) is a variation of KMC. In KLMC, all atoms are mapped onto a discrete lattice. This simplifies the processes of identifying state-to-

sate transitions and calculating the associated rate constants. Generally, the atoms do not always stay on a fixed lattice. In the presence of lattice defects such as interstitials and vacancies, the atoms around the defects will undergo relaxations to minimize the formation energy. However, if the mapping of the atoms onto the lattice points does not change during the relaxation, then the mapping is safe. KLMC is capable of simulating atomic processes in crystalline materials, but it is generally not applicable to processes in amorphous materials.

Generally, the KLMC approach works as follows. A rate catalog storing the rate constants of all the allowed transitions is maintained. The rate of a given transition is directly related to its associated energy barrier, which is given as an input to KLMC. At each KLMC iteration, a particular transition is picked with the probability proportional to its rate. Next, the chosen transition is performed; the rate catalog is updated according to the new configuration and system clock advances. Applying the iteration repeatedly, the evolution of the system can be tracked at large time scales. The flowchart of KLMC is shown in Figure 2.1.

Now we discuss the detailed formulation of KLMC. More in-depth description of this method can be found in Ref [21].

2.2.1 Justification

If we use a point to represent the system status on the potential energy surface, then this point constantly vibrates in the energy valleys for a while and performs infrequent jumps to the neighboring valleys via the saddle points. Figure 2.2 illustrates a typical trajectory on the potential energy surface. As long as it stays in each valley for time period much longer times than one vibration period (~1ps), the system will lose its memory of the trajectory prior to the last transition. Thus the rate constant (probability per unit time) of the current transition is independent of the previous one. Therefore, the state-to-state transition events can be thought of as a Markov process. This justifies the use of Monte Carlo statistical methods to propagate the

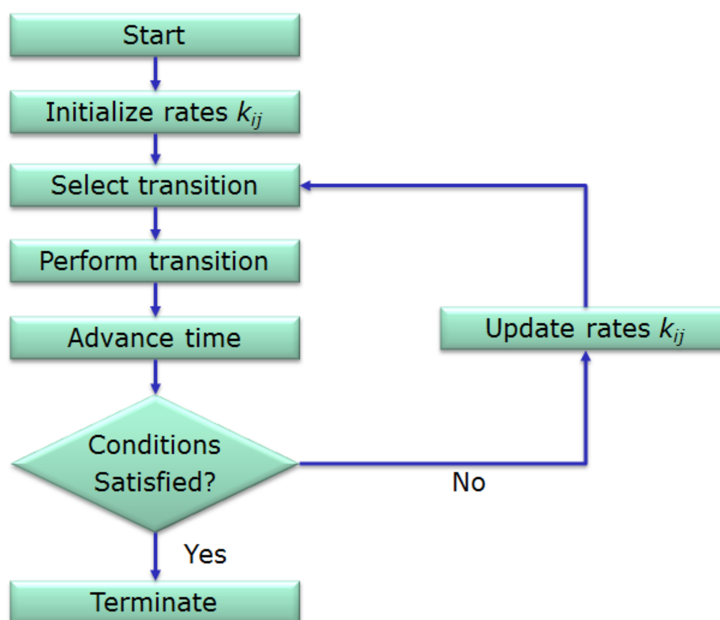

Figure 2.1: Flowchart of the KLMC simulations.

trajectories of system evolution.

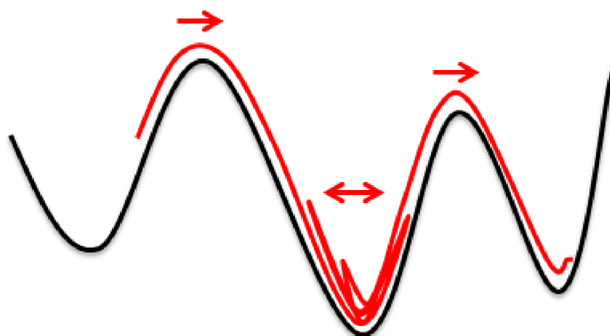

Figure 2.2: A typical trajectory featuring state-to-state transitions and vibrations in the vicinity of the energy valley.

2.2.2 Calculating rate constants

In KLMC, a *state* corresponds to a local minimum (valley) of the potential energy surface, and a transition is the event of migrating from one state to another via the saddle point. The harmonic transition state theory (hTST) [22, 23, 24] allows us to determine the rate constant of a given transition systematically. Figure 2.3 shows a typical transition on the potential energy landscape. Each transition is associated with an energy barrier, which is the energy difference between the saddle point and the initial point. According to hTST, the rate constant of a given transition from state i to state j is related to the associated energy barrier E_{ij}^m by

$$k_{ij} = \nu_{ij} \exp\left(-\frac{E_{ij}^m}{kT}\right) \tag{2.12}$$

where k is the Boltzmann constant, and T is the system temperature. ν_{ij} is a pre-exponential factor, defined by the ratio of the product of $3N$ normal mode frequencies of the initial point to the product of $3N-1$ real normal mode frequencies of the saddle point (excluding the mode with a imaginary frequency)

$$\nu_{ij} = \frac{\prod_{l=1}^{3N} \nu_l^{ini}}{\prod_{l=1}^{3N-1} \nu_l^{sad}} \tag{2.13}$$

In practice, the values of the energy barriers are generally extracted from first-principles quantum mechanical calculations such as DFT and fed into the KLMC simulator as an input. The value of the pre-exponential factor is often chosen as a fixed value during the KLMC simulations in order to save computation time. The value is usually in the range of $10^{12} \sim 10^{13}$ s^{-1}.

2.2.3 Picking transitions

Suppose the system is currently in state i, by using Eq. (2.12), we can calculate the set of rate constants $\{k_{ij}\}$ associated with the possible transition pathways. The

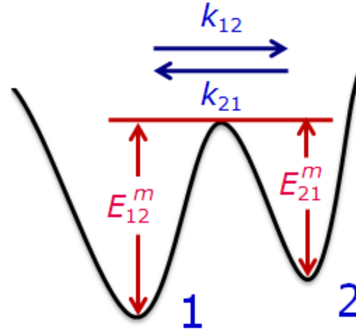

Figure 2.3: Energy barriers of state 1 to state 2, and vice versa.

next task is to pick a pathway with a probability proportional to the associated rate constant. The probability of picking the q-th transition is

$$P_{\text{pick}}(q) = \frac{k_{iq}}{k_{tot}} = \frac{k_{iq}}{\sum_j k_{ij}} \tag{2.14}$$

where the associated rate constant is normalized against the total rate constant summed over all possible pathways. To realize this, first imagine that for each of the pathways there's a line segment with a length equal to the associated rate constant. Aligning these line segments end to end gives a line of total length k_{tot}. We then generate a random number uniformly distributed over the length of this line. The corresponding pathway of the line segment that this number falls on is the one that we choose for the systems to follow. This rejection-free procedure is the BKL algorithm, first invented by Bortz, Kalos, and Lebowitz [25].

2.2.4 Calculating residence time

To advance the system clock, we have to calculate the residence time that the system spends in states i before the escape. Due to the memoryless property, the transition can be modeled as Poisson process. Given the total rate of transition from state i to any of the possible neighboring states k_{tot}, the probability density function of the

residence time t is

$$p(t) = k_{tot} e^{-k_{tot} t} \tag{2.15}$$

which is an exponential random variable [26]. This variable can be drawn as

$$t = \frac{-\ln \rho}{k_{tot}} \tag{2.16}$$

where ρ is a uniformly distributed random variable on $(0, 1)$. The system clock is then advanced by t.

Another way to calculate this residence time is to use the expectation value [21], where no random number needs to be generated.

$$\langle t \rangle = \int_0^\infty t p(t) dt = \frac{1}{k_{tot}} \tag{2.17}$$

2.3 *Continuum modeling*

The continuum modeling approach describes the system with continuum concentration fields and tracks system evolution using a set of continuity equations. The continuity equation of a given species X can be written as

$$\frac{\partial C_{\mathrm{X}}}{\partial t} = -\nabla \cdot J_{\mathrm{X}} + R_{\mathrm{X}}^{+} - R_{\mathrm{X}}^{-}$$

where R_{X}^{+} and R_{X}^{-} are the net rate of generation and consumption of X. J_{X} is the flux of X, including diffusion and drift terms. If the species is immobile, this term is zero.

In general, the reaction between two species X and Y can be written as

$$\mathrm{X} + \mathrm{Y} \Longleftrightarrow \mathrm{Z} \tag{2.18}$$

with the reaction rate per unit volume given as

$$R_{\mathrm{X/Y}} = k_f \left(C_{\mathrm{X}} C_{\mathrm{Y}} - K^* C_{\mathrm{Z}} \right) \tag{2.19}$$

where C's are the concentrations, K^* is the equilibrium constant. k_f is the reaction coefficient. Assuming the reaction are diffusion limited, this term can be expressed as

$$k_f = 4\pi a \left(d_{\mathrm{X}} + d_{\mathrm{Y}} \right) \tag{2.20}$$

where d's are the diffusivities of the two species, and a is the capture cross section of the reaction, usually on the order of 0.5 nm. Chapter 6 describes the continuum models for phosphorus diffusion and activation in detail.

Chapter 3

CORRELATION OF INTERSTITIAL-MEDIATED SELF-DIFFUSION IN SI

This chapter is adapted from a letter published in *Physical Review B* [27]. We have performed extensive analysis of the correlation factors for interstitial-mediated self-diffusion via various possible mechanisms and hopping networks in the diamond lattice using the kinetic lattice Monte Carlo approach. The correlation factor for the kick-out mechanism in the tetrahedral hopping network is calculated to be 0.73, in agreement with previous results; and the value for the hexagonal hopping network is 0.47 for the dominant mechanism. For the mechanism where a split interstitial is stable ("stable-split" mechanism), the correlation factor for the tetrahedral network stays the same while that for the hexagonal network increases to 0.62. We then performed simulations for the diffusion process of silicon involving multiple mechanisms. The choice of mechanisms is justified by *ab initio* calculations. We conclude that unlike vacancy diffusion, interstitial self-diffusion has a temperature-dependent correlation factor. This conclusion holds in general for diffusion processes involving multiple mechanisms with different activation energies. The correlation factor obtained from ab initio results for interstitial-mediated self-diffusion in silicon at 1000-1100 °C is 0.64-0.80, compared to the value of 0.6 extracted from the experiment.

3.1 Introduction

Self-diffusion is the most fundamental process in crystals. Under intrinsic conditions, it is caused by point defects such as vacancies and interstitials. Figure 3.1 illustrates the vacancy-mediated and interstitial-mediated self-diffusion mechanisms. Experi-

mentally, self-diffusion is usually measured by the usage of stable isotopes as tracers. Assuming the diffusion correlation factors of all charge states are equal [28, 29], the tracer diffusivity can be related to the self-diffusion coefficients via [30, 31, 32]

$$D_T = f_I D_I \frac{C_I^*}{C_S} + f_V D_V \frac{C_V^*}{C_S} \tag{3.1}$$

The symbols f, D, and C^* on the right-hand side denote the diffusion correlation factors, the diffusivity of interstitials (I) and vacancies (V), and the equilibrium concentrations, respectively. C_S is the concentration of the native lattice atom. The correlation factor enters the equation because although the movement of the point defects alone can be treated as uncorrelated random walks, the successive jumps of a tracer atom are correlated, due to interactions with intrinsic point defects [32, 33]. Figure 3.2 illustrates the correlation effects for vacancy and interstitial self-diffusion mechanisms. For the vacancy mechanism, once the tracer has made one jump via exchanging with a nearby vacancy, its next jump will be more likely to return to the previous location due to the vacancy nearby; and less likely to move in other directions, which requires a vacancy to approach it from the other directions. For the interstitial mechanism, once the tracer kicks out a silicon atom and becomes a substitutional atom, its next jump will be more likely to be kicked back by the interstitial nearby.

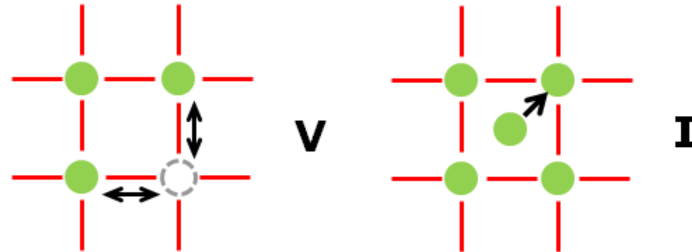

Figure 3.1: Vacancy- and interstitial-mediated self-diffusion mechanisms on a 2D square lattice.

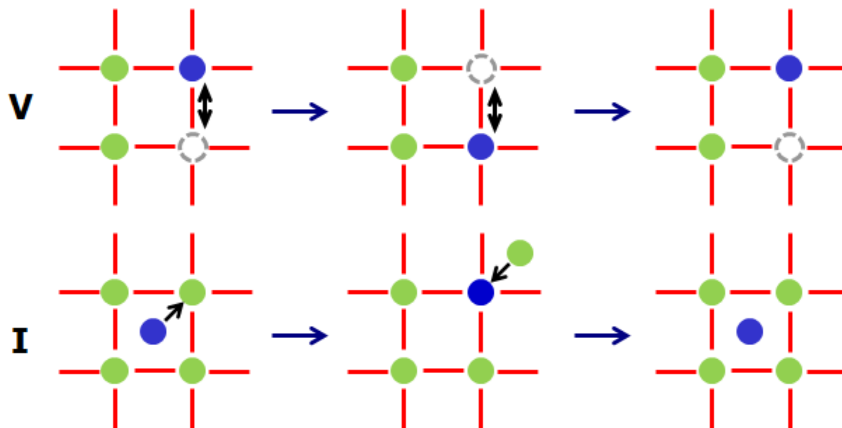

Figure 3.2: Correlation effects for vacancy- and interstitial-mediated self-diffusion mechanisms on a 2D square lattice. The tracer atom is denoted as blue spheres, and vacancy is the dashed empty circle. The green atom are normal silicon atoms.

The correlation factor is generally different for different crystals. Here, we limit the analysis to the diamond lattice structure, with representative materials including the group IV elements (C, Si, Ge, α-Sn, and Pb). In the diamond lattice, the correlation factor for the vacancy-mediated self-diffusion was calculated to be 0.5 by Compaan and Haven [34] using electric network theory. Since the vacancy mechanism is simple and only involves the vacancy-silicon exchange, this value is widely accepted [30]. However, the situation is much more complicated when it comes to the correlation factor for interstitial-mediated diffusion, since there are many possible mechanisms. In another paper, Compaan and Haven also calculated the correlation factor for interstitial diffusion as 0.7273, assuming a tetrahedral configuration for interstitials and a kick-out mechanism [33]. However, their analysis is limited to just one interstitial configuration, and the process of constructing and appropriately truncating resistive networks is quite tedious.

Over the past 50 years, due to the pervasive applications of silicon technology, the self-diffusion phenomenon in silicon has been investigated by many researchers. Experimental data show that the value of f_I must be about 0.6 in order to match

phosphorus diffusion data in silicon [35]. Meanwhile, various *ab initio* investigations on self-diffusion in silicon report values of 0.56 [36], 0.59 [37], 0.69 [37], and 0.75 [38]. Generally, for a simple mechanism, the correlation factor depends only on the geometric aspects of the hopping transitions. However, for real situations such as interstitial self-diffusion in silicon, where multiple mechanisms are present, the correlation factor also depends on the energetics of the formation and migration of the interstitial defects. We have first performed extensive analysis of various possible mechanisms and hopping networks of interstitial self-diffusion in the diamond lattice. We then identify the possible mechanisms involved in self-diffusion in silicon based on *ab initio* calculation results and calculate the effective correlation factor for the combined diffusion mechanism in silicon.

3.2 Simulation methods

According to the statistical diffusion theory [22, 23, 24], the tracer diffusion correlation factor is related to the square displacements of the tracer and interstitial by

$$f = \frac{\overline{\Delta r^2/N}^{tr}}{\overline{\Delta r^2/N}^{I}} \tag{3.2}$$

where Δr^2 and N are the square displacement and total hopping steps, and the superscripts tr and I denote tracer and interstitial properties, respectively. Figure 3.3 illustrates the difference between a tracer and an interstitial in a diffusion hop. When a tracer atom on an interstitial site[1] A kicks a silicon atom on site B into another interstitial site C, the tracer atom has moved from A to B, while the interstitial atom has moved from A to C. Note that the role of interstitial is played by different atoms

---

[1]It is necessary to clarify "interstitial site" versus "interstitial". An "interstitial site" is a site that is not a regular diamond lattice site. Some of the high symmetry interstitial sites are the tetrahedral (t) and hexagonal (h) sites. An interstitial (I_i) is a configuration where an atom occupies an interstitial site. Some common types of interstitials are the tetrahedral interstitial (I_t), hexagonal interstitial (I_h), and split-interstitial (I_x) in which two atoms share a lattice site.

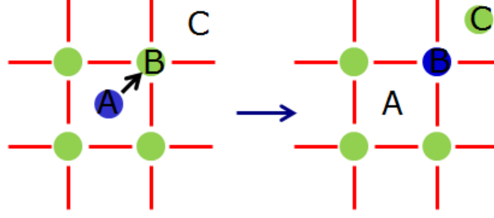

Figure 3.3: Difference of a tracer atom and an interstitial atom in an direct diffusion hop.

during the kick-out process (first the tracer, then the regular atom). For diffusion hops involving the substitutional sites (indirect process), the movement of the interstitial is always larger than that of the tracer, resulting in a correlation factor value that is less than 1. For the diffusion hops that take place only on interstitial sites (direct process), the two quantities are equal, and the correlation is 1 (i.e. no correlation effect).

For a single mechanism in a given hopping network, the quantity on the right hand side of Eq. (3.2) can be calculated by the average cosine value of the angles between successive jumps

$$f = \frac{1 + 2\overline{\cos\theta_{i,i+1}}^{tr} + 2\overline{\cos\theta_{i,i+2}}^{tr} + \cdots}{1 + 2\overline{\cos\theta_{i,i+1}}^{I} + 2\overline{\cos\theta_{i,i+2}}^{I} + \cdots} \tag{3.3}$$

For the mechanisms discussed below, all of the non-successive jumps are uncorrelated (i.e. $\overline{\cos\theta_{i,j}} = 0$, for $j > i + 1$). Besides, half of the successive jumps are also uncorrelated (i.e. $\overline{\cos\theta_{i,i+1}} = 0$, for every second i). Therefore, we can simplify Eq. (3.3) as [34]

$$f = \frac{1 + \overline{\cos\theta}^{tr}}{1 + \overline{\cos\theta}^{I}} \tag{3.4}$$

where the terms $\overline{\cos\theta}$ without subscripts (i) denote the average of the non-zero cosine values corresponding to the angles between the vectors of correlated hops.

Since the correlation factor does not depend on tracer concentration, we have used

in our simulation only one tracer, which starts off at an interstitial site and moves randomly in the domain. We also track the trajectory of the interstitial, which is just the extra atom (either a tracer or a native atom) in the domain. For a single mechanism in a given hopping network, we use Eq. (3.4) to calculate the correlation factor. For combined mechanisms, Eq. (3.2) is used; and the ratio is determined via a linear fit to the Δr^2-N data.

We have carried out kinetic lattice Monte Carlo (KLMC) simulations of the diffusion processes of tracers and interstitials. The simulation domain consists of a three-dimensional array of native lattice atoms. We have performed tests on different domain sizes and found that the influence of the domain size on the results is negligible. Periodic boundary conditions are used, but the times of crossing through periodic boundaries are included in the calculation of displacements. The rate constants are determined by the migration barriers, which are determined by *ab initio* calculations.

All the *ab initio* calculations were done using the density functional theory (DFT) code VASP [13, 14, 15, 16] with the Perdew-Wang 1991 generalized gradient approximation functional [39] and ultrasoft Vanderbilt-type pseudopotentials [40, 41]. All the calculations were were performed in a nominally 64 atom supercell with periodic boundary conditions and $2 \times 2 \times 2$ Monkhorst-Pack [18] k-point sampling. Calculations have also been carried out for 216-atom supercells and the change of total energy differences is within 0.02 eV. An energy cutoff of 250 eV was used to achieve required accuracy. The structures were fully relaxed to a maximal force of less than 0.005 eV/Å per atom. The climbing image nudged elastic band (NEB) method [19, 20] was used to identify transition paths between two given stable configurations, with the stopping criterion being a maximum force less than 0.005 eV/Å per atom for each image.

3.3 *Correlation factor of the "kick-out" mechanism*

Over the past years, many interstitial self-diffusion mechanisms have been proposed. Some argue a direct mechanism, in which interstitials make a sequence of direct hops between interstitial sites. In this case, the tracer and the interstitial are always the same atom, and the jumps will, in general, be uncorrelated [33]. Another set of mechanism involves atoms on lattice sites and is called the indirect "kick-out" mechanism [42]. In this mechanism, a tracer atom on an interstitial site A approaches a native atom at the lattice site B and kicks it out onto an interstitial site C, after which the tracer takes the lattice site B. If we think of the split-interstitial I_x as the intermediate state, the kick-out process actually consists of two processes: $I_i \rightarrow I_x$ and $I_x \rightarrow I_i$. In this kick-out process, the tracer has made one hop from A to B; while the interstitial has made two successive hops, from A to B and then to C. This kick-out mechanism assumes that the processes $I_i \rightarrow I_x$ and $I_x \rightarrow I_i$ happen in cascades. This kick-out mechanism will generally be correlated since, in the next move of the tracer on site B, it will have a higher probability of being kicked back by the new interstitial atom nearby (on site C). Once the tracer atom is kicked out again to an interstitial site, the next step will generally be uncorrelated with the previous step. Thus, by tracking the average cosine values of the incoming and outgoing hop directions during the kick-out processes, we can determine the correlation factor via Eq. (3.4).

Compaan determines the $\overline{\cos\theta}$ values in Eq. (3.4) for the kick-out mechanism using resistive network theory and calculates the correlation factor to be 0.7273 for the tetrahedral network ($I_t \leftrightarrow I_x \leftrightarrow I_t$). Apart from considering the tetrahedral network, we extend the analysis to include the hexagonal network, as both tetrahedral and hexagonal interstitials have been reported in various DFT studies as the low energy structures in silicon and germanium [43, 44, 45, 46]. Consider a typical kick-out process where an interstitial atom kicks a native atom on the lattice site out onto a

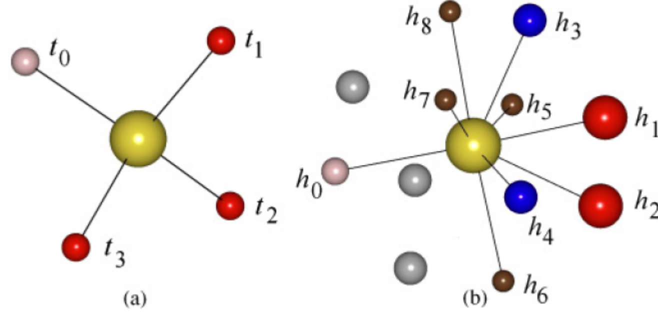

Figure 3.4: Schematics of the "kick-out" mechanism in the (a) tetrahedral network, and (b) hexagonal network. t_0 and h_0 denote the incoming tracer. The center atom is the silicon atom being kicked out. For tetrahedral configurations t_{1-3} (red/dark spheres) are equivalent, while for hexagonal configurations, the neighbors can be divided into 3 groups: $h_{1,2}$ (red/dark, large spheres), $h_{3,4}$ (blue/dark, medium spheres), and h_{5-8} (brown/dark, small spheres). The other h sites (grey/light, medium spheres) are excluded.

new interstitial site. In the tetrahedral network, shown in Figure 3.4(a), the tracer atom starts at one of the tetrahedral sites t_0 and kicks the silicon atom onto one of the neighboring interstitial sites t_i (i = 1, 2, 3). During this process, the tracer moves from t_0 to the lattice site; while the interstitial moves from t_0 to t_i. Due to symmetry, these three t_i sites are equivalent, with $\cos\theta^I$ equal to 1/3. In the hexagonal hopping network, shown in Figure 3.4(b), the tracer atom starts at one of the interstitial sites h_0 and kicks the silicon atom onto one of the neighboring interstitial sites h_i (is = 1, 2, ..., 9) on the other side of the lattice site (3 sites have been excluded since they are on the same side as h_0). We break the possible hexagonal destinations into 3 groups, with $\cos\theta^I$ equal to 9/11, 5/11, and 1/11 respectively. Correspondingly, we have three sub-mechanisms for the hexagonal hopping network. We argue that for geometry reasons the mechanism with $\cos\theta^I = 9/11$ is the dominant process, which is also supported by *ab initio* calculations. For the sake of completeness, we include all three sub-mechanisms in our analysis.

We have calculated the correlation factor values for the kick-out mechanism in

Table 3.1: Correlation factors for the "kick-out" mechanism in the tetrahedral and hexagonal hopping networks. The mechanism in the hexagonal network is categorized into 3 groups based on the kick-out direction. The brackets denote the corresponding destinations after the kick-out. The $\overline{\cos\theta}^I$ value is fixed for each mechanism, and the $\overline{\cos\theta}^{tr}$ value is calculated from the KLMC approach. The uncertainty of the correlation factor is the standard error of the mean.

Network	$\overline{\cos\theta}^I$	$\overline{\cos\theta}^{tr}$	f
Tetrahedral (t_{1-3})	4/12	-0.0299	0.7276±0.0001
Hexagonal ($h_{1,2}$)	9/11	-0.1475	0.4690±0.0001
Hexagonal ($h_{3,4}$)	5/11	-0.0731	0.6372±0.0001
Hexagonal (h_{5-8})	1/11	-0.0073	0.9099±0.0001

the tetrahedral and hexagonal networks. The results are listed in Table 3.1. The value for the tetrahedral network (0.7276±0.0001) is very close to Compaan and Haven's value (0.7273) [33]. Actually we believe that our value is more accurate than Compaan and Haven's which is derived from truncating infinite resistive networks. This result demonstrates the validity of the KLMC approach. The value for the hexagonal hopping network decreases as $\cos\theta^I$ increases. For all the mechanisms, the $\overline{\cos\theta}^{tr}$ values are negative, consistent with the argument that after the tracer kicks out an atom, it will have a higher probability of being kicked back.

3.4 Correlation factor of the "stable-split" mechanism

The above analysis assumes that the $I_i \rightarrow I_x$ and $I_x \rightarrow I_i$ processes happen in cascades, which implies that the transition state, which is the split-interstitial configuration, is unstable. However, it has been proposed based on various *ab initio* results that there exists a stable split interstitial oriented along the $\langle 110 \rangle$ direction [46]. Therefore, in this part we drop the assumption of the kick-out mechanism and consider the situation where the split-interstitial is stable (denoted as "stable-split" mechanism hereafter). In this case, either of the atoms comprising the split can hop onto neighboring interstitial sites. In turn, the atom on interstitial sites can hop onto

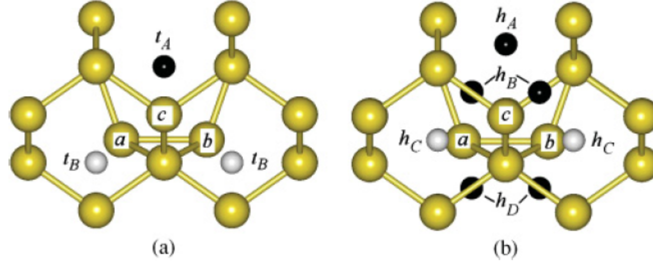

Figure 3.5: Allowed hopping directions in the (a) split-tetrahedral and (b) split-hexagonal networks, viewed along the $\langle 1\bar{1}0 \rangle$ direction. a and b form the $\langle 110 \rangle$-split interstitial. c is the original lattice site. In (a) the small spheres denote the 4 first nearest tetrahedral neighbors of the split categorized into 2 groups, 2 in t_A and 2 in t_B. The allowed hopping destinations of the split are the 2 t_B sites only. In (b) the small spheres denote the 12 first nearest hexagonal neighbors of the split categorized into 4 groups, 2 in h_A, 4 in h_B, 4 in h_C and 2 in h_D. The allowed hopping destinations of the split are the 4 h_C sites only. Note that some nearest neighbors behind are blocked by the ones in front of them, when viewed along this direction.

a lattice site and form a split interstitial with the lattice atom.

We again consider the tetrahedral and hexagonal hopping networks. For split interstitials, we limit our analysis to $\langle 110 \rangle$-split interstitials, which have been found to be the most stable structure in Si and Ge [46]. Due to the fact that the $\langle 110 \rangle$-split interstitial has an orientation, certain orientation constraints have to be imposed on the migration paths. Figure 3.5 illustrates the constraints for the split hopping onto tetrahedral and hexagonal sites. By intuition we can see that only the sites that are located along the direction most aligned with the split orientation are favored (t_B in (a) and h_C in (b)). The others are located in a roughly orthogonal (t_A in (a) and h_A, h_B, h_D in (b)) direction and are therefore unfavorable. Similarly, when a tetrahedral (hexagonal) interstitial hops onto the lattice site and forms a split interstitial, only 3 (2) out of the 6 $\langle 110 \rangle$-split orientations are allowed. These orientation constraints are verified by the migration barrier results from NEB calculations.

We have calculated the correlation factor values for the stable-split mechanism in the tetrahedral and hexagonal network with the above orientation constraints im-

Table 3.2: Correlation factor values for the tetrahedral and hexagonal hopping networks. The $\overline{\cos\theta}^{I}$ value is calculated analytically, and the $\overline{\cos\theta}^{tr}$ value is calculated via the KLMC approach. The uncertainty of the correlation factor is the standard error of the mean.

Network	$\overline{\cos\theta}^{I}$	$\overline{\cos\theta}^{tr}$	f
Tetrahedral	-1/3	-0.5150	0.7275±0.0001
Hexagonal	-1/11	-0.4357	0.6207±0.0001

posed. The results are listed in Table 3.2. Using statistical diffusion theory, the $\overline{\cos\theta}^{I}$ value can be calculated analytically by constructing allowed hopping networks of the interstitial. The average cosine values become smaller than the kick-out mechanism due to the fact that here more choices of $I_x \rightarrow I_i$ hop directions are allowed after an $I_i \rightarrow I_x$ hop. In other words, not only "kick-out", but also "bounce-back" are allowed. The correlation factor for the tetrahedral network is the same as the previous value, simply because when the tracer is bounced back, it returns to the previous interstitial site and has no net displacement, giving no contribution to the total correlation effect. The situation is different for hexagonal sites, since when bounced back, the tracer atom can be on a different interstitial site (e.g. In Figure 3.5 (b) jumping between two h_C sites on the left via atom a).

3.5 Correlation factor of combined mechanisms in silicon

In this part, we perform a case study for interstitial-mediated self-diffusion in silicon. The lowest-energy structures as well as the migration barriers of self-interstitials in silicon have been studied extensively [43, 44, 45, 46]. The general consensus is that the hexagonal, tetrahedral, and ⟨110⟩-split interstitials have relatively lower formation energies than other configurations [46]. We have performed *ab initio* calculations which confirmed that the lowest-energy structures are the ⟨110⟩-split and hexagonal interstitials,with formation energies of 3.70 and 3.79 eV, respectively; while the

tetrahedral interstitial has a slightly higher formation energy of 3.97 eV. Using the NEB method, we have identified several migration paths and calculated the associated barriers, which are shown in Table 3.3 and Figure 3.6. The tetrahedral interstitial is found to be an intermediate state, which relaxes to a hexagonal interstitial. The direct (uncorrelated) mechanism, $I_h \leftrightarrow I_h$ via I_t, has a lower barrier than the indirect mechanism $I_x \leftrightarrow I_h$. Previously a fourfold interstitial defect has been reported [47]. However, due to the high migration barrier of the concerted exchange [45], they are less likely to migrate and thus not included in our analysis. The +2 charge state interstitials reported in a recent paper [48] are also excluded due to their high migration barriers.

Table 3.3: Migration barriers of various migration paths of self-interstitials in silicon.

Migration path	Forward barrier (eV)	Reverse barrier (eV)
$I_x \leftrightarrow I_h$	0.34	0.25
$I_x \leftrightarrow I_t$	0.38	0.11
$I_h \leftrightarrow I_h$	0.17	0.17
$I_h \leftrightarrow I_t$	0.17	0.00

From the analysis above, there are two major hopping mechanisms for self-diffusion in silicon: $I_h \leftrightarrow I_x$, and $I_h \leftrightarrow I_h$. The former is the indirect mechanism in the hexagonal hopping network. The latter is the direct mechanism, with a correlation factor of 1. In the presence of both mechanisms, the hexagonal interstitial can diffuse either directly or indirectly. If we denote the corresponding probabilities as P_{direct} and P_{indirect}, then we have $P_{\text{direct}} = 1 - P_{\text{indirect}}$ and the effective correlation factor f_{eff} should be a function of P_{direct}. To determine the relationship between f_{eff} and P_{direct}, we have performed KLMC simulations with P_{direct} varying from 0 (pure indirect) to 1 (pure direct). The f_{eff} value is extracted via Eq. (3.2). For the indirect mechanism, we consider the dominant kick-out mechanism with $\overline{\cos\theta}^I = 9/11$ ($f = 0.4690$) and the stable-split mechanism ($f = 0.6207$). The results are plotted in Figure 3.7. As can be

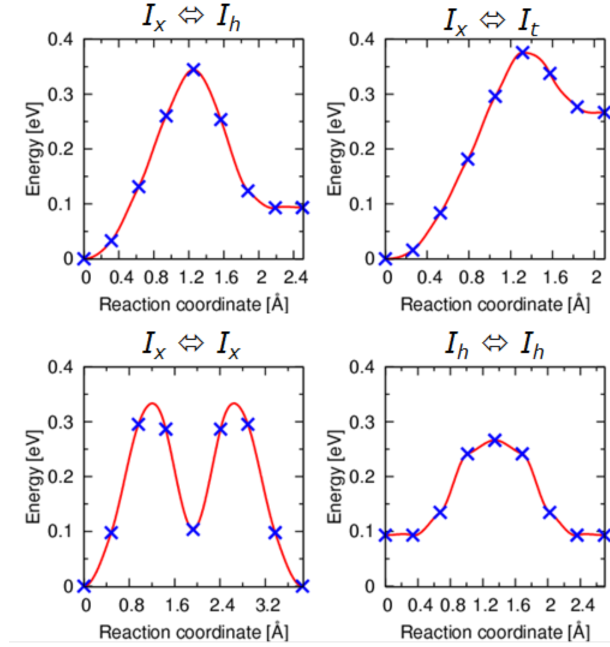

Figure 3.6: Migration energy of different migration paths of self-interstitial diffusion in silicon.

seen, the total effective correlation factor increases monotonically as the probability of direct mechanism increases, with values approaching unity when the direct mechanism is more favorable, rendering the diffusion more uncorrelated. The correlation factor for the stable-split mechanism is higher than for the kick-out mechanism for a given P_{direct}. The actual correlation factor for a certain P_{direct} value should lie somewhere between the two curves when the kick-out and stable-split mechanisms are both present.

According to the transition state theory the probability P_{direct} can be expressed as

$$P_{\text{direct}} = \frac{\Omega_{\text{direct}} \exp\left(-E^m_{\text{direct}}/kT\right)}{\Omega_{\text{direct}} \exp\left(-E^m_{\text{direct}}/kT\right) + \Omega_{\text{indirect}} \exp\left(-E^m_{\text{indirect}}/kT\right)} \tag{3.5}$$

where Ω is the entropy factor associated with the mechanisms, and E^m is the corresponding migration barrier. Once the migration barriers are determined, the only variable that controls the probability P_{direct}, and therefore f_{eff}, is the temperature.

Therefore, unlike in vacancy diffusion, here the effective correlation factor for the combined mechanisms of interstitial-mediated self-diffusion in silicon is temperature dependent, which may be the reason for the different correlation values reported in literature [35, 36, 37, 38].

Assuming that the entropy factors are the same for the two mechanisms, the correlation factor at 1000-1100 °C is calculated to be 0.64 for the kick-out mechanism and 0.80 for the stable-split mechanism using the values in Table 3.3. This estimate is higher than the reported experimental value of 0.6 for the same temperature range [35]. Sources for the differences include uncertainties in values extracted experimentally and the energetics of the mechanisms predicted by the DFT calculations which results in overestimation of the probability of the direct mechanism. Another possible source of error comes from the neglect of the entropy difference of the two mechanisms. Better quantification of the entropy factors requires *ab initio* studies of the vibrational frequencies of the transition states of the two mechanisms.

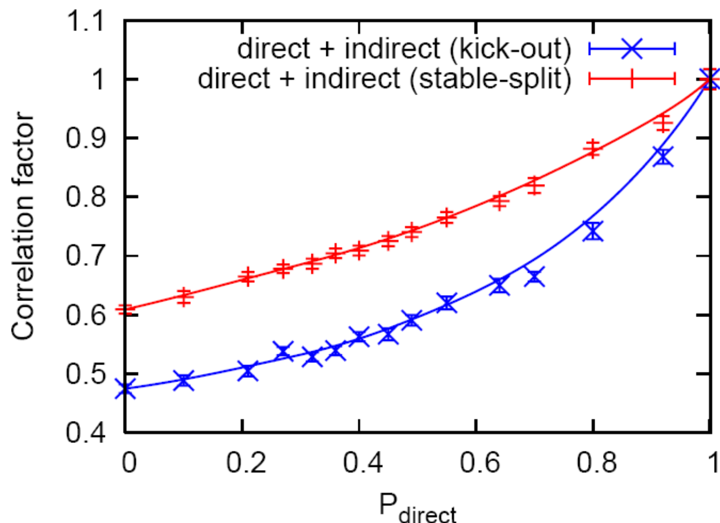

Figure 3.7: Effective correlation factors of interstitial-mediated self-diffusion in silicon as a function of the probability of hopping via the direct mechanism.

3.6 Conclusion

Using the kinetic lattice Monte Carlo approach, we have performed extensive analysis of the correlation factor values of interstitial self-diffusion for various possible mechanisms and hopping networks in the diamond lattice. The correlation factor for the kick-out mechanism in the tetrahedral hopping network is 0.72, which is in agreement with previous results; and the value for the hexagonal hopping network is 0.47 for the dominant mechanism. For the mechanism where a split interstitial is stable (stable-split mechanism), the correlation factor for the tetrahedral network stays the same while that for the hexagonal network increases to 0.62. We then identify the possible mechanisms involved in interstitial-mediated self-diffusion in silicon based on *ab initio* calculation results and calculate the effective correlation factor for the combined mechanism. Unlike vacancy diffusion, interstitial-mediated self-diffusion has a temperature-dependent correlation factor. This conclusion in general holds for diffusion processes involving multiple mechanisms with different activation energies. The correlation value obtained from *ab initio* results at 1000-1100 °C is 0.64, higher than the experimental value of 0.6.

Chapter 4

INTERDIFFUSION IN SIGE ALLOYS

This chapter is adapted from a letter published in *Journal of Vacuum Science and Technology B* [49]. Point-defect-mediated diffusion processes are investigated in strained SiGe alloys using kinetic lattice Monte Carlo KLMC simulation technique. The KLMC simulator incorporates an augmented lattice domain and includes defect structures, atomistic hopping mechanisms, and the stress dependence of transition rates obtained from density functional theory calculation results. Vacancy-mediated interdiffusion in strained SiGe alloys is analyzed, and the stress effect caused by the induced strain of germanium is quantified separately from that due to germanium-vacancy binding. The results indicate that both effects have substantial impact on interdiffusion.

4.1 Introduction

The silicon-germanium alloy is commonly used in many applications, mainly in electronics such as metal oxide semiconductor field effect transistors (MOSFETs) [2, 50, 51, 52], heterojunction bipolar transistors [53], and optoelectronic devices such as quantum-well optical modulators [54, 55, 56]. SiGe presents several advantages compared with traditional Si-based devices. The Si-Ge lattice mismatch of 4.17% induces strain to the device. Application of strain modifies the band structure which leads to a reduced carrier scattering and thus an increase in electron mobility. Applied strain can also modify the effective mass of holes and has a potential to increase hole mobility. Figure 4.1 shows a transmission electron micrograph of p-type MOSFET with SiGe as source and drain, where uniaxial strain increases the hole mobility by

50% [2].

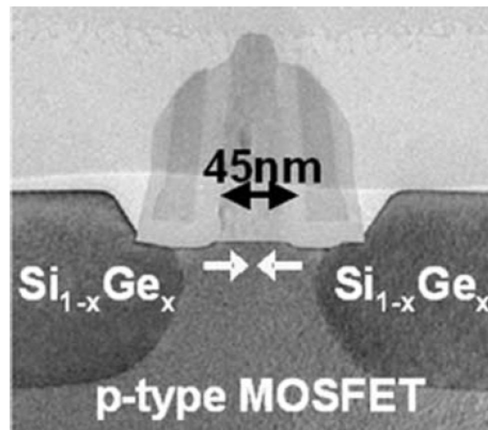

Figure 4.1: TEM micrograph of a 45-nm *p*-type MOSFET. [2]

Ideally, the concentrations of Ge in the device should vary abruptly to achieve better strain and band gap control. However, interdiffusion, which occurs at the interface, is a big challenge to these specifics. Interdiffusion during the thermal anneals will effectively decrease the thickness of strained channel [57], and also increase the impurity scattering [58, 59]. It can also lead to highly unwanted modification of E field in optoelectronics devices [60]. Figure 4.2 shows a TEM image of the Si-Ge interface after thermal annealing, with SIMS measured Ge concentration imposed [3].

SiGe Interdiffusion is believed to be mediated by point defects, predominantly vacancies [3, 61, 62, 63]. Generally, interdiffusivity depends on both temperature and germanium content in the material. Xia *et al.* found that interdiffusivity is proportional to the exponential of Ge content and has a constant activation energy for Ge fractions between 0 and 0.56 over the temperature range of 770-920 °C [4]. A

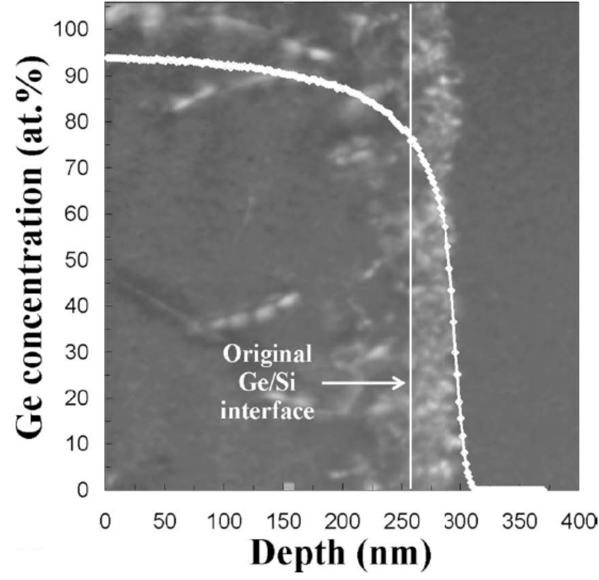

Figure 4.2: Cross-sectional TEM image of a Si-Ge interface annealed at 900 °C for 30 min. [3]

piece-wise model for interdiffusivity is constructed as

$$D = \begin{cases} 310 \exp\left(-\frac{4.66\text{ eV}}{kT}\right) \exp\left(8.1 x_{\text{Ge}}\right), & x_{\text{Ge}} < x_0 \\ 310 \exp\left(-\frac{4.66\text{ eV}}{kT}\right) \exp\left(8.1 x_{\text{Ge}}\right) \exp\left[14.9\left(x_{\text{Ge}} - x_0\right)\right], & x_{\text{Ge}} > x_0 \end{cases} \tag{4.1}$$

The presence of Ge has two effects on interdiffusion: (a) the stress effect due to the lattice mismatch between Ge and Si, in which replacing a Si atom with Ge contributes an extra strain energy term to the total energy of the system, and (b) the alloy effect, in which Ge causes perturbation to the ideal silicon lattice. To build general predictive models, it is necessary to separate stress effect from alloy effect. However, it is difficult to do so experimentally. The KLMC approach, capable of capturing explicitly the local variations in alloy distribution and stress tensor and how they affect the diffusion processes, has great potential for simulating interdiffusion in strained SiGe alloys. In this chapter, we use a KLMC simulator to investigate vacancy-mediated SiGe

Table 4.1: DFT parameters for V mediated interdiffusion.

Quantity	Value (eV)
Migration for V-Si exchange	0.34
Migration for V-Ge exchange	0.17
Ge-V binding energy	-0.31

interdiffusion in strained SiGe alloys. The inputs of the KLMC model, such as the activation energies for atomic hops and the induced strain values of point defects, are obtained from DFT calculations summarized in previous works [64, 65, 66].

4.2 Model implementation

In our model, we treat silicon as the perfect atom and substitutional Ge and vacancy as defects. Interstitials are ignored as SiGe interdiffusion is predominately vacancy mediated [3]. A Ge-V binding of -0.31 eV has been included, which is obtained from DFT calculations [65]. Binding among other species are significantly lower [67] and are thus neglected in the current analysis. We assume that diffusion occurs through the following two transitions:

$$\mathrm{V} + \mathrm{Si} \iff \mathrm{Si} + \mathrm{V} \tag{4.2}$$

$$\mathrm{V} + \mathrm{Ge} \iff \mathrm{Ge} + \mathrm{V} \tag{4.3}$$

The migration barriers of these transitions, which are simply the associated energy difference between the transition and initial states, are determined from DFT calculations [64]. The energy values used as inputs to the KLMC simulation are listed in Table 4.1 and the energy profiles of the transitions are plotted in Figure 4.3.

The actual migration barrier of a transition can be expressed as the sum of E_0^m, the unbiased barrier (as shown in Table 4.1) plus the change in the barrier due to other effects such as pair binding and external stress. The change in the migration

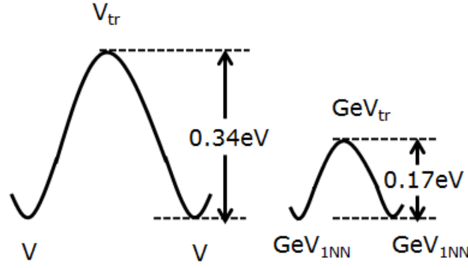

Figure 4.3: Energy profiles of the transitions. V_{tr} and $\mathrm{GeV}_{\mathrm{tr}}$ denote the transition states for transition 4.2 and 4.3 respectively.

barrier can be expressed as a combination of the formation energy changes of states that satisfies detailed balance

$$E^m = E_0^m + \left(\Delta E_{\mathrm{tr}}^f - \Delta E_{\mathrm{in}}^f + \frac{\Delta E_{\mathrm{fi}}^f - \Delta E_{\mathrm{in}}^f}{2} \right) \tag{4.4}$$

where ΔE^f is the change in formation energies, and the subscripts in, tr, and fi represent initial, transition, and final states, respectively. The formation energy change due to applied stress and pair binding can be expressed as

$$\Delta E = \Delta E_{\mathrm{stress}} + \Delta E_{\mathrm{binding}} = -V_0 \left(\Delta \boldsymbol{\epsilon} \cdot \boldsymbol{\sigma} \right) + \Delta E_{\mathrm{binding}} \tag{4.5}$$

where V_0 is the atomic volume of the silicon lattice, $\Delta\boldsymbol{\epsilon}$ is the induced strain of the point defects/impurities, and $\boldsymbol{\sigma}$ is the applied stress to the system. Both stress and strain tensors are written in the contracted notation [68]. The second term is the sum of all pair energies of the system, extending from first nearest neighbors (1NNs) to nth nearest neighbors (nNNs). In our analysis here we simply consider interactions among 1NNs. Table 4.2 lists induced strain vectors that are used to calculate $\Delta E_{\mathrm{stress}}$ via Eq. (4.5).

Eq. (4.5) includes the two effects of Ge on interdiffusion. The binding energy of

Table 4.2: Induced strain vectors of point defects/impurities which are associated with the energies of the initial and the final states of a hop.

Quantity	V	Ge_S	V_{tr}	Ge_{tr}
$\Delta\epsilon_{xx}$	-0.22	0.05	-0.42	-0.37
$\Delta\epsilon_{yy}$	-0.22	0.05	-0.42	-0.37
$\Delta\epsilon_{zz}$	-0.22	0.05	-0.42	-0.37

-0.31 eV enters represents the second term and contributes to the alloy effect, while the induced strain values enters the first term and contributes to the strain effect.

4.3 Stress analysis

Here we describe the theoretical background for stress analysis.

A three-dimensional stress-strain relation is:

$$\sigma = \mathbf{C} : \epsilon \tag{4.6}$$

where σ and ϵ are called stress and strain tensors, which are both 2nd order symmetric tensors, with 6 independent entries. $\mathbf{C}$ is the 4th order stiffness tensor, with 21 independent entries. Ignoring shear stress and strain components, the stress and strain tensors reduced to vectors and the stiffness tensor have dimension of 3×3. For materials with cubic symmetry, when coordinates are along the (100) axes, the stiffness tensor have only two independent components. Thus the stress-strain relation simplifies to

$$\begin{pmatrix} \sigma_1 \\ \sigma_2 \\ \sigma_3 \end{pmatrix} = \begin{pmatrix} C_{11} & C_{12} & C_{12} \\ C_{12} & C_{11} & C_{12} \\ C_{12} & C_{12} & C_{11} \end{pmatrix} \begin{pmatrix} \epsilon_1 \\ \epsilon_2 \\ \epsilon_3 \end{pmatrix} \tag{4.7}$$

The strain energy, is given by:

$$E_{st} = \frac{V}{2}\epsilon^T\sigma = \frac{V}{2}\epsilon^T\mathbf{C}\epsilon \tag{4.8}$$

In a supercell regime, a defect will induce a shift of equilibrium lattice spacing. First define a normalized induced strain for a N-atom supercell with one defect.

$$\Delta\epsilon_i = \frac{a_i - a_{0i}}{a_{0i}} N \tag{4.9}$$

The N is equivalent to dividing by $1/N$, which is the concentration of the defect. Thus the strain energy of a defect under any applied strain relative to the bulk Si is

$$E = \frac{V}{2}\left(\epsilon - x\Delta\epsilon\right)^T \sigma = \frac{V}{2}\left(\epsilon - x\Delta\epsilon\right)^T \mathbf{C}\left(\epsilon - x\Delta\epsilon\right) \tag{4.10}$$

Expanding the terms and ignoring the quadratic terms of ϵ, we get:

$$\begin{aligned} E(\epsilon) &= \frac{V}{2}\Delta\epsilon^T\mathbf{C}\Delta\epsilon - Vx\Delta\epsilon^T\mathbf{C}\epsilon && (4.11)\\ &= E(0) - Vx\Delta\epsilon^T\mathbf{C}\epsilon && (4.12)\end{aligned}$$

Thus the energy of a defect has a linear dependence on the applied strain of the system. The formation energy of a simple defect, such as I, V, as a function of applied strain is

$$E_f\left(\epsilon\right) = E_f(0) - Vx\Delta\epsilon^T\mathbf{C}\epsilon \tag{4.13}$$

4.4 KLMC simulations

We have applied the KLMC simulation approach described above to investigate the effect of Ge on the vacancy-mediated SiGe interdiffusion in strained SiGe alloys. The simulation domain contains a $5 \times 5 \times 64$ array of silicon unit cells, corresponding to a slab of depth of about 320 Å and cross section of about 27×27 Å^2. Initially, the Ge concentration profile is a step function, with a Ge fraction of 0 on one side and 20% on the other. The domain and initial Ge distribution closely resembles the step structure called “BM20” in Ref. [4]. Figure 4.4 shows an initial configuration of the SiGe alloy system, where Ge atoms are confined to the right side. We have divided

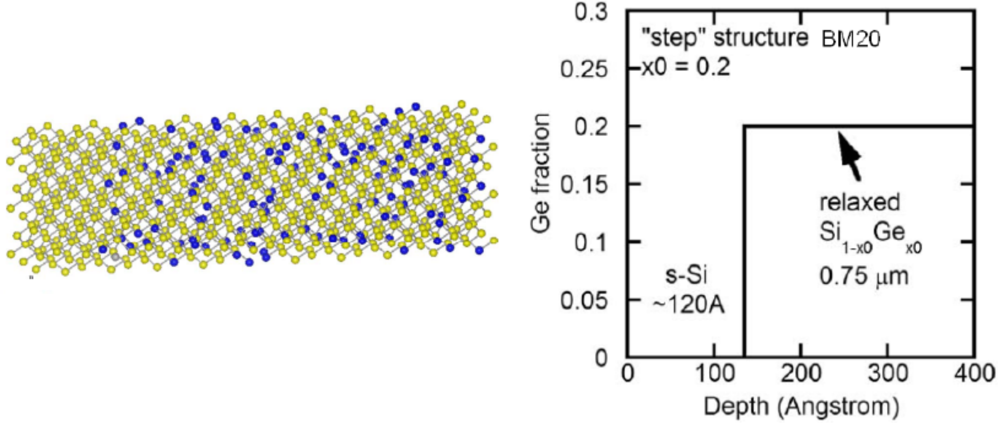

Figure 4.4: Schematic of simulation domain, with random alloy arrangement of 20% Ge. Ge fraction plot adapted from Ref [4].

the simulation domain into mono-layer slabs, and the Ge concentration in each slab is monitored. During the simulation, Ge atoms are tracked and the Ge concentration in each slab is updated. From this, the strain energy in each slab is calculated assuming that stress energy is only a function of Ge concentration.

The external applied stress can be related to the applied strain in a three-dimensional vector form

$$\boldsymbol{\sigma} = \mathbf{C} \cdot \boldsymbol{\epsilon} \tag{4.14}$$

where $\mathbf{C}$ is the stiffness tensor of Si and $\boldsymbol{\epsilon}$ is the external normal strain. Shear components can be neglected as they are zero for configurations considered,The structure that we have simulated is an epitaxial layer of pure Si grown on top of a relaxed $\mathrm{Si}_{1-x0}\mathrm{Ge}_{x0}$ layer. Due to the positive induced strain of Ge atoms, the equilibrium lattice constant of $\mathrm{Si}_{1-x}\mathrm{Ge}_{x}$ is larger than that of Si, a_0, with a relation given by [65]

$$a(x) = a_0 + 0.194x + 0.035x^2 \tag{4.15}$$

Considering the fact that the underlying SiGe layer is relaxed, the external strain of

a point in the interface region with a Ge fraction of x is expressed as

$$\epsilon_{\parallel}(x) = \frac{a(x) - a(x_0)}{a(x_0)} \tag{4.16}$$

$$\epsilon_{\perp}(x) = -\nu\epsilon_{\parallel}(x) \tag{4.17}$$

where $\epsilon_{\parallel}$ and $\epsilon_{\perp}$ denote the strain components within and perpendicular to the interface plane, respectively, ν is Poisson's ratio, and x_0 is the germanium fraction in the underlying SiGe layer. Plugging Eq. (4.15) into Eqs. (4.16) and (4.17) results in a biaxial tensile stress for the silicon and interdiffusion region.

To avoid clustering effects, only one vacancy is initialized randomly in the system. This implies that the vacancy concentration under the simulation condition is not necessarily the vacancy concentration under equilibrium conditions. In order to compare the simulated results with experimental data, the simulated results have to be scaled to yield behavior for equilibrium vacancy concentrations. In our analysis, we use free vacancy concentration, which is the vacancy concentration in the Ge-free region, to normalize the vacancy concentration since it can be readily compared to a simple calculation. Once we determine the free vacancy concentration under the simulation condition, we can scale the result to the equilibrium case. If the total elapsed time to reach the final profile is calculated to be t in the simulation, then the elapsed time to reach the same profile for the vacancy concentration under the equilibrium condition, t^*, is calculated as

$$t^* = \frac{C_{\mathrm{V}}}{C_{\mathrm{V}}^*}t \tag{4.18}$$

where C_{V}^* and C_{V} are the free vacancy concentrations under the equilibrium and the simulation conditions, respectively. It can be seen that the elapsed time and the vacancy concentration have an inverse relation. This is consistent with the physical intuition that the higher the vacancy concentration, the faster the vacancy-mediated

interdiffusion process, and thus the shorter time required to obtain a given profile. Another way to interpret this for $C_{\mathrm{V}}^{*} < C_{\mathrm{V}}$ as in our simulations is to think of the equilibrium case as if the system is attached to a huge reservoir which it equilibrates with. The difference between t^{*} and t represents the expected time during which the system is expected to not have any vacancies present, and thus no changes will occur in the system.

Before we proceed to the analysis of the equilibrium diffusivity as function of the Ge fraction, the determination of the free vacancy concentrations under both the equilibrium and simulation conditions should be elucidated. The free vacancy concentration under the equilibrium condition is a strain-dependent property and is closely related to the formation energy change due to strain [66]

$$\frac{C_{\mathrm{V}}^{*}(\boldsymbol{\epsilon})}{C_{\mathrm{V}}^{*}(0)} = \exp\left(-\frac{\Delta E_{f}^{\mathrm{V}}(\boldsymbol{\epsilon})}{kT}\right) \tag{4.19}$$

where $C_{\mathrm{V}}^{*}(\boldsymbol{\epsilon})$ and $C_{\mathrm{V}}^{*}(0)$ represent the equilibrium free vacancy concentration with and without strain, respectively. $\Delta E_{f}^{\mathrm{V}}(\boldsymbol{\epsilon})$ is calculated from Eq. (4.5) with induced strain values of vacancy from Table 4.2. $C_{\mathrm{V}}^{*}(\boldsymbol{\epsilon})$ corresponds to the equilibrium free vacancy concentration for the case where stress effect due to Ge is included, while $C_{\mathrm{V}}^{*}(0)$ corresponds to that for the case where the stress effect is absent. Since we are not interested in their absolute values, the ratio in Eq. (4.19) is enough to make the comparison between the two cases.

To obtain the free vacancy concentration under the simulation condition, we calculate the free time ratio R as the ratio of the average time the vacancy spends on any one site in the Ge-free region to the total elapsed time

$$R = \frac{\bar{t}_0}{t} = \frac{(1/N_0)\sum_{i=1}^{N_0} t_i}{\sum_{i=1}^{N} t_i} \tag{4.20}$$

where t_i is the cumulative time that vacancy is on site i during the simulation, N

is the total number of sites in the simulation, and N_0 is the total number of sites in the Ge-free region. From the probability perspective, each site within that region has a probability of R to be occupied by a vacancy at any given time. Thus, the free vacancy concentration can be derived from the concentration of sites, C_{S} in that region, which is simply the silicon lattice site density (5×10^{22} cm^{-3}),

$$C_{\mathrm{V}} = RC_{\mathrm{S}} \tag{4.21}$$

Thus, we are able to scale the results from Eqs. (4.19)-(4.21) and then perform Boltzmann–Matano analysis [69, 70] of the system behavior under equilibrium vacancy concentration, which gives the diffusivity as

$$D\left(C'\right) = -\frac{1}{2t^*}\left(\frac{dz}{dC}\right)_{C'} \int_0^{C'} \left(z - z_m\right) dC \tag{4.22}$$

where z is the depth within the simulation, z_m is the Boltzmann-Matano plane defined in Ref. [4], and C is the Ge concentration. To factor out the time variable, we carried out the following substitution:

$$\eta = \frac{z - z_m}{\sqrt{t^*}} \tag{4.23}$$

giving

$$D\left(C'\right) = -\frac{1}{2}\left(\frac{d\eta}{dC}\right)_{C'} \int_0^{C'} \eta dC \tag{4.24}$$

As we discussed before, the presence of Ge has two effects on interdiffusion process. From an atomistic perspective, on the one hand Ge enhances V-mediated diffusion due to Ge-V binding, as Ge on neighboring sites lowers V formation energy; and on the other hand, since vacancy and germanium have opposite induced strain values, vacancies are more likely to be close to Ge atoms to compensate the strain energy. These two effects both lead to interdiffusivity values increasing as increased Ge concentration. In order to separate these two effects, we have performed simulations with

and without stress effect present (no formation energy changes due to stress effect). Plotting diffusivity as a function of η for both cases allows us to compare the results directly. Figure 4.5 shows the calculated data and smoothed curve based on fitting to a constrained cubic spline function [71] for the Ge profile after simulation.

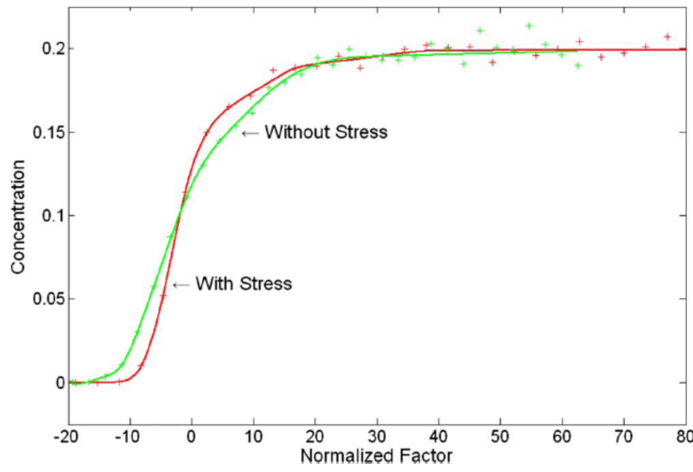

Figure 4.5: Concentration profiles as functions of the normalization factor, η, for vacancy-mediated SiGe interdiffusion with and without consideration of the stress effect. The results are obtained for temperature equal to 920 °C. "+"s are original data and lines are fitted curves.

Using the fitted curve of Figure 4.5, we can perform Boltzmann–Matano analysis which yields the diffusivity versus concentration relationship shown in Figure 4.6. Fitting the data with an exponential relation between diffusivity and germanium concentration Fitting the data with an exponential relation between diffusivity and germanium concentration:

$$D\left(x_{\mathrm{Ge}}\right)/D_0 = \exp\left(B x_{\mathrm{Ge}}\right) \tag{4.25}$$

we have extracted the fitted values of B for both alloy and stress effects of Ge, which are shown in Table 4.3.

In our analysis, the exponential factor B of the total effect is extrapolated to be

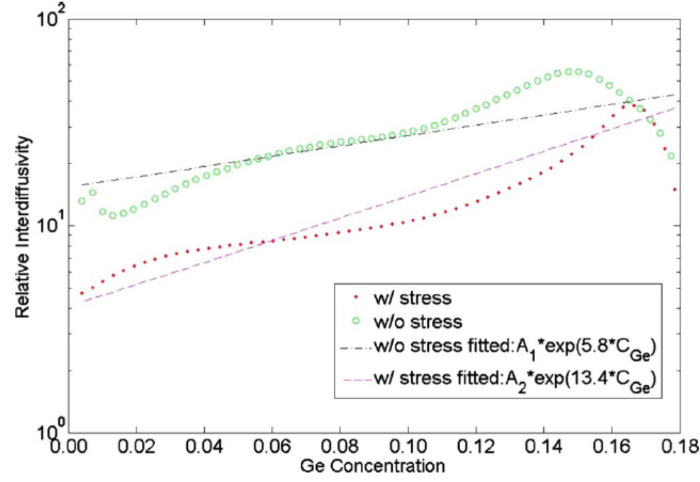

Figure 4.6: Interdiffusivity values (symbols) extracted from Figure 4.5 and fittings (dashed lines) to Eq. (4.25) for pure alloy effect (w/o stress) and alloy effect combined with stress effect (w/stress) of Ge in the system. The results are obtained for a temperature of 920 °C.

Table 4.3: Fitted values of B in exponential model for SiGe interdiffusion due to different effects of Ge concentration.

Stress effect	Alloy effect	Total effect
7.6	5.8	13.4

13.4. This can be compared to the extracted values of experimental results from Xia *et al.* [4]. In their paper, interdiffusivity is modeled in a piecewise exponential form with B of 8.1 and 23 in the tensile and compressive strain regime respectively. Our analysis does not consider the different regimes of applied strain and gives a value that is close to the average of the two values in their paper. Also note that the extracted value of B under tensile strain in the experiment appears to underestimate the experimentally observed dependence. Using a stronger Ge concentration dependence under tensile strain leads to extraction of a weaker dependence under compressive strain conditions, thus bringing both values closer to our result extracted from the simulation.

In general, Ge enhances V-mediated diffusion due to Ge-V binding, as Ge on

neighboring sites lowers V formation energy. In addition, the lower concentration of Ge leads to tensile stress in the interdiffusion region that retards vacancy-mediated diffusion. Vacancies have a negative induced strain for the initial, final, and transition states, but the one for the transition state has a larger absolute value. A tensile stress will not only reduce the equilibrium vacancy concentration but also increase the formation energy difference between the transition state and the initial state, and therefore increase the migration barrier of the hop in Eq. (4.5) thus making vacancy-mediated migration less energetically favorable. This is consistent with Figure 4.5, where the Ge profile is broader when stress effect is not present, which indicates that tensile stress on Si side retards vacancy-mediated diffusion.

4.5 Summary

We have presented kinetic lattice Monte Carlo simulations to investigate interdiffusion in strained SiGe alloys, with input values including induced strains and migration barriers obtained from DFT calculations. Simulation of the SiGe alloy structure has separated stress and alloy effects caused by the presence of germanium. The application of KLMC approach to investigate interdiffusion processes indicates its potential for simulating full multistep annealing of strained SiGe devices.

Chapter 5

PHOSPHORUS DIFFUSION AND DEACTIVATION IN SILICON

5.1 Introduction

Diffusion of phosphorus below the solid solubility limit has been studied extensively in the past. The diffusion behavior under various experimental conditions is well characterized by models with a pair-diffusion scheme [5, 29, 72, 73, 74, 75]. These models assume that phosphorus substitutional atoms (active phosphorus) is immobile itself and can only migrate via pairing with point defects, i.e. interstitials or vacancies. The point defects can have multiple charge states, whose concentrations depend on the position of the Fermi level. The Fermi level position is in turn a function of active phosphorus concentration. In this way, the effective diffusivity of phosphorus is dependent on the Fermi level [76]

$$D_{eff} = D^0_{\text{int}} + D^-_{\text{int}}\left(\frac{n}{n_i}\right) + D^=_{\text{int}}\left(\frac{n}{n_i}\right)^2 + D^+_{\text{int}}\left(\frac{n}{n_i}\right)^{-1} + D^{++}_{\text{int}}\left(\frac{n}{n_i}\right)^{-2}$$

where D^i_{int} is the intrinsic diffusivity associated with point defects of charge state i, with i varying from -2 to +2. The Fermi level dependence is included as $\frac{n}{n_i}$, which is simply $e^{\frac{E_f - E^i_f}{kT}}$ assuming Boltzmann statistics. Figure 5.1 shows the simulation results of phosphorus solid source diffusion for several peak phosphorus concentrations fitted against experimental data. It can be seen that the model predictions and experimental observations are in excellent agreement with each other. At low phosphorus concentrations, the charge state effect is negligible and the diffusivity is close to the intrinsic value everywhere in the region; thus the diffused profile closely resembles a

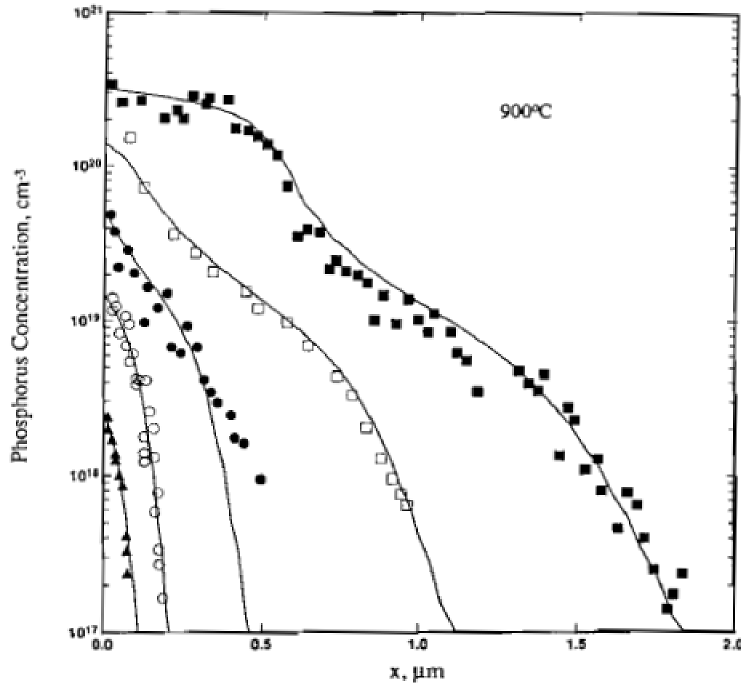

Figure 5.1: Simulated phosphorus solid state diffusion profiles using the pair-diffusion model fitted against experimental data, from Ref. [5].

Gaussian function. At higher phosphorus concentrations, additional features of the diffused profile are present: a plateau region near the interface, a long tail at the end, and a kink in between. The enhanced diffusion of the plateau is due to the increased concentration of negatively charged vacancies at high Fermi level, which facilitates phosphorus-vacancy paring and enhances phosphorus diffusion. The enhanced tail diffusion is caused by the supersaturation of interstitials in the tail region due to the so-called *chemical pumping effect* [76]. A detailed description of the pair-diffusion model is in Appendix B.

The above models only consider phosphorus species that are electrically active. In real situations, phosphorus can become inactive, mainly due to two mechanisms: high doping and interface segregation. When phosphorus is very heavily doped such that the concentration exceeds its solubility, it forms complexes devoid of any electrical

activity. Experimental data [77] indicate that the solubility value varies from 2×10^{20} cm^3 to 4×10^{20} cm^3 when temperature increases from 700 °C to 1100 °C. During the annealing cycle, phosphorus can also deactivate by interface segregation, in which mobile phosphorus species get trapped in a thin layer of oxide near the interface. The trap sites capture phosphorus and reduce the total dose of phosphorus in silicon. The surface density of the trap sites is estimated to be on the order of the silicon lattice density ($\sim 1 \times 10^{15}$ cm^3). It is observed that at least a dose of approximately 2×10^{14} cm^3 can get trapped at the interface for a 30 min annealing at 800 °C [78].

There are several experimental methods to characterize the concentration of both active and total phosphorus as functions of depth in a given sample. Here we briefly describe two methods, the secondary ion mass spectroscopy (SIMS) and electrochemical capacitance-voltage (ECV) profiling.

SIMS can detect the total phosphorus concentration, both active and inactive. This is done by sputtering the surface of the sample with a focused primary ion beam and collecting and analyzing ejected secondary ions. These secondary ions are measured with a mass spectrometer based on the charge-mass ratio. Thus the measured ion count is directly related to the total concentrations, regardless of their chemical states in the sample. For phosphorus in silicon, the ^{31}P isotope is usually measured. Due to the interference of ^{30}Si^{1}H, the detection limit of of ^{31}P is on the order of 10^{15} cm^{-3} [79]. During the SIMS analysis, the sample surface is sputtered away slowly, allowing continuous analysis of composition as a function of depth. Figure 5.2 illustrates the sputtering of sample surface by a primary beam during SIMS measurements [6].

ECV detects electrically active phosphorus profiles. The technique makes a depletion region in the sample and measures its small-signal capacitance, which is directly related to the doping profile and electrically active defect densities. To reach the inner depth of a sample, the sample is chemically etched. Since this approach probes electrical properties in nature, it detects only the electrically active phosphorus. The

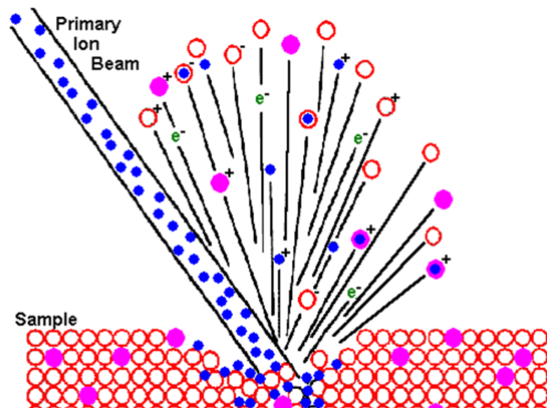

Figure 5.2: Schematic of the sputtering of sample surface by a primary beam during SIMS measurements, from Ref. [6].

limitation of ECV lies in the smearing of the edge of the depletion region. Rather than an abrupt change of carrier concentration from the depletion region to the neutral region, as assumed by the depletion approximation, in the real situation, the concentrations vary slowly at the edge of the depletion region for a length on the order of L_D, the *Debye length*. Since L_D is inversely proportional to the doping concentration, this effect is more severe in probing lightly-doped regions near the metallurgical junction [80].

5.2 Phosphorus-vacancy cluster model

For common dopants in silicon, several models have been proposed for the deactivation mechanism. Deactivation of arsenic in silicon is known to be dominated by the vacancy cluster mechanism based on both theoretical and experimental evidences [81, 82, 83, 84, 85, 86]. The deactivation mechanism of phosphorus is still under debate due to the lack of conclusive experimental observations. While some propose the formation of SiP precipitates as the major deactivation mechanism [77] , others suggest a similar cluster model as arsenic deactivation based on the similarities of phosphorus and arsenic in silicon [87, 88]. Our DFT calculations support the vacancy

cluster model. In this model, phosphorus deactivates through the formation of small phosphorus-vacancy clusters, each containing up to several phosphorus atoms and a vacancy. These clusters can be written as P_nV, denoting a vacancy paring with n of its first nearest neighbors ($1 \leq n \leq 4$). Figure 5.3 illustrates the structure of P_nV cluster with $n = 4$.

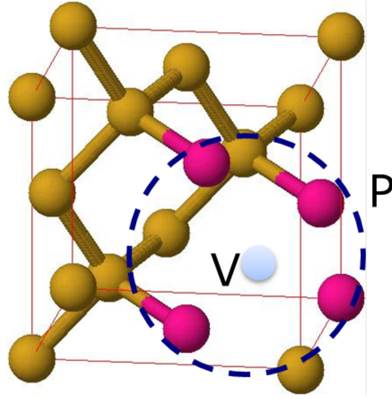

Figure 5.3: Schematic of a P_4V cluster containing 4 phosphorus atoms (pink/dark) and a vacancy (grey/light).

5.2.1 DFT calculations

In this part we present DFT calculation results of the energetics of P_nV clusters. All the *ab initio* calculations were done using the density functional theory (DFT) code VASP [13, 14, 15, 16] with the Perdew-Wang 1991 generalized gradient approximation functional [39] and ultrasoft Vanderbilt-type pseudopotentials [40, 41].Calculations are performed in a supercell consisting of 64 lattice sites with a $2 \times 2 \times 2$ mesh of Monkhorst-Pack [18] k-points for integrations over the Brillioun zone, and a 320 eV cutoff in the plane-wave expansions. The GGA equilibrium lattice constant of 5.4566 Å[65] were used and kept fixed throughout the calculations. Energy gain due to stress relaxation is quite small (< 0.02 eV).

The calculated formation and binding energy of the clusters are listed in Table 5.1. The formation energy of P_nV are calculated against neutral and substitutional

phosphorus

$$E^f_{\mathrm{P}_n\mathrm{V}} = E^{tot}_{\mathrm{P}_n\mathrm{V}} - nE^{tot}_{\mathrm{P_S}} + \left(n - \frac{63}{64}\right) E^{tot}_{\mathrm{Si64}} \tag{5.1}$$

And the binding energy of $\mathrm{P}_n\mathrm{V}$ is calculated against isolated $\mathrm{P}_{n-1}\mathrm{V}$ and substitutional phosphorus

$$E^b_{\mathrm{P}_n\mathrm{V}} = E^f_{\mathrm{P}_n\mathrm{V}} - E^f_{\mathrm{P}_{n-1}\mathrm{V}} - E^f_{\mathrm{P_S}} \tag{5.2}$$

The above two equations are for $n = 0, 1, \cdots, 4$, where $n = 0$ corresponds to a single vacancy.

From the calculated values, we can see that there is large binding between phosphorus and vacancy. The energy gain of adding a phosphorus to the cluster is more than 1 eV. This makes the formation of $\mathrm{P}_n\mathrm{V}$ exothermic for $n \geq 3$.

Table 5.1: Formation and binding energy of $\mathrm{P}_n\mathrm{V}$ clusters. Formation energy is referenced to neutral and substitutional phosphorus. Binding energy of $\mathrm{P}_n\mathrm{V}$ is calculated against isolated $\mathrm{P}_{n-1}\mathrm{V}$ and substitutional phosphorus.

	$\mathrm{P}_1\mathrm{V}$	$\mathrm{P}_2\mathrm{V}$	$\mathrm{P}_3\mathrm{V}$	$\mathrm{P}_4\mathrm{V}$
E^f (eV)	2.31	0.97	-0.18	-1.68
E^b (eV)	-1.19	-1.34	-1.15	-1.50

Based on the *ab initio* calculations we estimate the equilibrium concentrations of various phosphorus species as functions of total phosphorus concentration. Ignoring entropy factors, the equilibrium concentration of the clusters are calculated by

$$C_{\mathrm{P}_n\mathrm{V}} = C_{\mathrm{Si}} \left(\frac{C_{\mathrm{P_S}}}{C_{\mathrm{Si}}}\right)^n \left(\frac{C_{\mathrm{V}}}{C^*_{\mathrm{V}}}\right) \exp\left(-\frac{E^f_{\mathrm{P}_n\mathrm{V}}}{kT}\right) \tag{5.3}$$

where $E^f_{\mathrm{P}_n\mathrm{V}}$ is the associated formation energy as obtained in Table 5.1, and C_{Si} is the silicon lattice density. C_{V} and C^*_{V} are actual and equilibrium vacancy concentrations

respectively. The total phosphorus concentration is thus given as

$$C_{\mathrm{P}}^{tot} = C_{\mathrm{P_S}} + n \sum_{n=1}^{4} C_{\mathrm{P}_n\mathrm{V}} \tag{5.4}$$

The concentrations of phosphorus species under equilibrium vacancy concentrations as functions of total phosphorus concentration at 840 °C (a common temperature for phosphorus emitter diffusion in crystalline silicon solar cells) are plotted in Figure 5.4. For low phosphorus concentrations, virtually all phosphorus takes the substitutional form. As soon as total phosphorus concentration exceeds 10^{20} cm^{-3}, $\mathrm{P_4V}$ concentration increases steeply and quickly becomes comparable to that of $\mathrm{P_S}$. When P concentration further increases, $\mathrm{P_4V}$ becomes the dominant species, while the active phosphorus concentration remains at around 2×10^{20} cm^{-3}. For all concentration ranges, the concentrations of $\mathrm{P}_n\mathrm{V}$ with $n \leq 3$ are negligible and thus don't show up in the plot. This simple analysis gives the right "ball-park" of the solubility of phosphorus and is consistent with experimental observations on the active and deactive phosphorus concentrations [32].

5.2.2 Continuum model

We have built a continuum model that simulates the deactivation process by the kinetics of cluster formation. The reactions that lead to clustering are

$$\mathrm{PV} + \mathrm{P_S} \Longleftrightarrow \mathrm{P_2V} \tag{5.5}$$

$$\mathrm{PV} + \mathrm{PV} \Longleftrightarrow \mathrm{P_2V} + \mathrm{V} \tag{5.6}$$

$$\mathrm{PV} + \mathrm{P_2V} \Longleftrightarrow \mathrm{P_3V} + \mathrm{V} \tag{5.7}$$

$$\mathrm{PV} + \mathrm{P_3V} \Longleftrightarrow \mathrm{P_4V} + \mathrm{V} \tag{5.8}$$

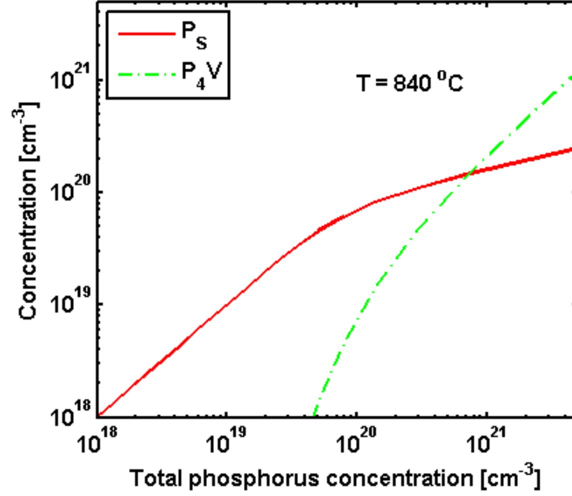

Figure 5.4: Equilibrium substitutional phosphorus P_S (active) concentration and P_4V (inactive) concentration as functions of the total phosphorus concentration at 840 °C. The concentrations of P_nV with $n \leq 3$ are negligible and fall out of the plotting range.

where P_S is the substitutional active phosphorus. Since PV is the mobile species, it can react with other P-containing species, facilitating cluster growth to P_4V.

The associated reaction rates are

$$R_{PV/P_S} = 4\pi a \cdot d_{PV} \left[C_{PV} C_{P_S} - K_{PV/P_S} \cdot C_{P_2V} \right] \tag{5.9}$$

$$R_{PV/PV} = 4\pi a \cdot 2d_{PV} \left[C_{PV} C_{PV} - \cdot K_{PV/PV} \cdot C_{P_2V} C_V \right] \tag{5.10}$$

$$R_{PV/P_2V} = 4\pi a \cdot d_{PV} \left[C_{PV} C_{P_2V} - K_{PV/P_2V} \cdot C_{P_3V} C_V \right] \tag{5.11}$$

$$R_{PV/P_3V} = 4\pi a \cdot d_{PV} \left[C_{PV} C_{P_3V} - K_{PV/P_3V} \cdot C_{P_4V} C_V \right] \tag{5.12}$$

where K_{PV/P_S}, $K_{PV/PV}$, K_{PV/P_2V} and K_{PV/P_3V} are equilibrium constants that have Arrhenius dependences on temperature. These constants are related to the binding energy of the clusters defined as in Table 5.1 but also contain entropy terms that are neglected in the previous equilibrium thermodynamics analysis and additional terms

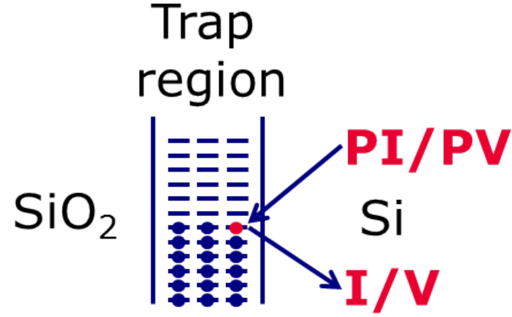

Figure 5.5: Illustration of the trapping process in the interface trap region.

to account for charge state dependencies. The activation energies for K's are chosen to be close to the binding energy values from DFT calculations, and the prefactors are used as fitting parameters.

5.3 Interface trap model

The segregation of P into the SiO_2-Si interface is modeled by mobile phosphorus species (phosphorus point defect pairs) entering empty interface traps and releasing free point defects, as seen in Figure 5.5. We assume that a thin trap region exists between the SiO_2-Si interface, with thickness x_T on the order of a nanometer.

The reactions that describe the trapping process are

$$\mathrm{PI} + \mathrm{T_e} \Longleftrightarrow \mathrm{P_T} + \mathrm{I} \tag{5.13}$$

$$\mathrm{PV} + \mathrm{T_e} \Longleftrightarrow \mathrm{P_T} + \mathrm{V} \tag{5.14}$$

where $\mathrm{T_e}$ is an empty trap site not filled by phosphorus; $\mathrm{P_T}$ is a trapped phosphorus, neither mobile nor active. The trapping reactions are

$$R_\mathrm{T}^\mathrm{I} = 4\pi a d_\mathrm{PI}\left[C_\mathrm{PI}\left(N_\mathrm{T} - C_{\mathrm{P_T}}\right) - \frac{\pi_\mathrm{I}}{\chi_\mathrm{I}} K_\mathrm{T}^\mathrm{I} \cdot C_{\mathrm{P_T}} C_\mathrm{I}\right] \tag{5.15}$$

$$R_{\mathrm{T}}^{\mathrm{V}} = 4\pi a d_{\mathrm{PV}} \left[C_{\mathrm{PV}} \left(N_{\mathrm{T}} - C_{\mathrm{P_T}} \right) - \frac{\pi_{\mathrm{V}}}{\chi_{\mathrm{V}}} K_{\mathrm{T}}^{\mathrm{V}} \cdot C_{\mathrm{P_T}} C_{\mathrm{V}} \right] \tag{5.16}$$

where N_{T} is concentration of traps, and $C_{\mathrm{P_T}}$ is the concentration of trapped phosphorus. $K_{\mathrm{T}}^{\mathrm{I}}$ and $K_{\mathrm{T}}^{\mathrm{V}}$ are the equilibrium constant for the reactions controlling the actual capacity of the trap sites and can be used as fitting parameters. The π and χ terms take care of charge state dependencies (Definitions of these terms are in Appendix B). The forward rate is proportional to the number of empty trap sites in the trap region $(N_{\mathrm{T}} - C_{\mathrm{P_T}})$, while the reverse rate is proportional to the number of filled trap sites $(C_{\mathrm{P_T}})$.

The surface density of the trap sites is usually set to be the surface density of silicon, e.g. at the (100) surface $\sigma_{\mathrm{T}} = (5 \times 10^{22})^{2/3} = 1.357 \times 10^{15}\ \mathrm{cm}^{-2}$. The concentration of the trap sites is simply the surface density divided by the region thickness, i.e. $N_{\mathrm{T}} = \sigma_{\mathrm{T}} / x_{\mathrm{T}}$. It turns out that varying the thickness of the trap region does not alter the diffused profile, as long as the surface density is kept fixed.

5.4 Modeling of solid source diffusion of high phosphorus concentration diffusion

We have applied these models to simulate phosphorus solid state diffusion experiments in silicon, in which is diffused from a P-rich oxide layer at 840 °C for 40 min. We assume a constant phosphorus concentration in the oxide and a segregation boundary across the oxide-silicon boundary, where the flux across the boundary depends on the phosphorus concentrations on both sides of the interface [89]:

$$J = k^S \left(C_P^{\mathrm{ox}} - \frac{C_P^{\mathrm{Si}}}{r^S} \right) \tag{5.17}$$

where k^S is the kinetic factor for segregation, usually chosen rather large so that equilibrium of the phosphorus concentrations on both sides is quickly established. This implies that diffusion through the interface is fast enough so that the choice of kseg has little influence on the diffusion profile in silicon. r^S is the segregation coefficient

of phosphorus between the two regions. Figure 5.6 shows the model predictions and experimental measurements from SIMS and ECV. The difference of SIMS and ECV profiles at the top region indicates that a large fraction of phosphorus is deactivated. When phosphorus concentration drops below 2×10^{20} cm^{-3}, SIMS profiles overlap with ECV, suggesting that all phosphorus are active phosphorus. The discrepancy of SIMS and ECV data at the tail is due to the systematic error of ECV measurements. ECV tends to underestimate the tail due to the depletion effect, as mentioned in 5.1. The simulated total and active phosphorus profiles match SIMS and ECV data respectively. At the peak region, P_4V clusters account for the difference between total (pink) and active (blue) phosphorus profiles. From the inset, we can also see a sharp increase of total P profile at the first several nanometers towards the interface, which consists of a high concentration of trapped phosphorus at the interface trap region.

Figure 5.7 shows the dose of various phosphorus species as functions of annealing time. The dose of trapped phosphorus gets saturated quickly at 30 s, while the doses for the active and clustered phosphorus grow as phosphorus diffuses into Si. The active phosphorus is only a small portion of the total phosphorus, which consists mostly of deactivated P_4V.

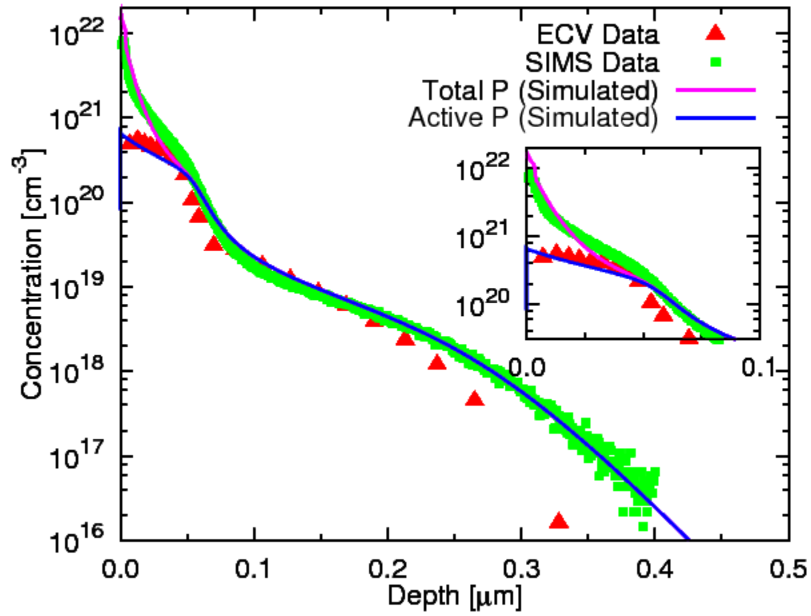

Figure 5.6: Simulation (lines) of the ECV profile (electrically active phosphorus) and the SIMS profile (total phosphorus) as compared to the experimental data (symbols) from University of Hannover.

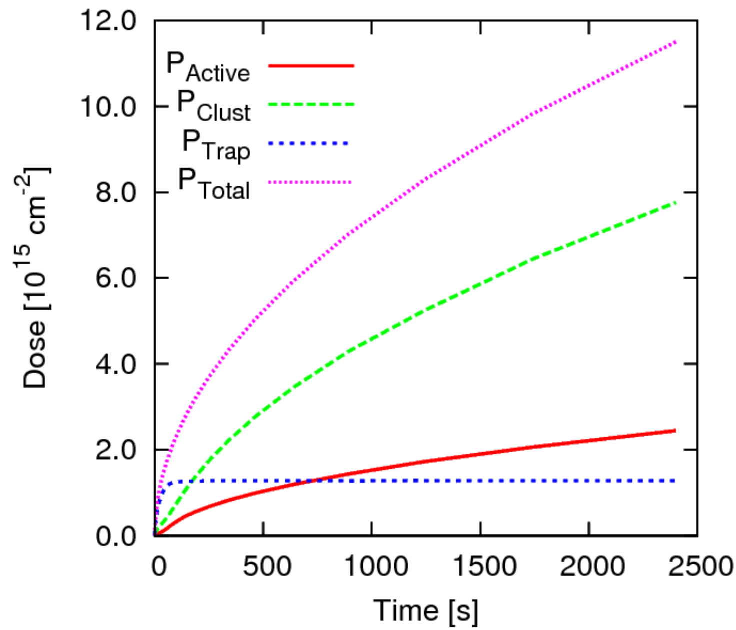

Figure 5.7: Simulation of the time dependence of P dose as active, clustered, trapped species.

Chapter 6

$POCL_3$ EMITTER DEPOSITION PROCESS

This chapter is adapted from a manuscript submitted to *Progress in Photovoltaics: Research and Applications*. We measure concentration profiles within the deposited phosphosilicate glass (PSG) layer for a range of $POCl_3$ doping conditions and find that (i) its composition is nearly independent of process conditions and (ii) it is separated from Si by a thin SiO_2 layer. We also find strong accumulation of P at the SiO_2-Si interface. As common linear-parabolic models cannot fully explain the observed kinetics of PSG thickness and phosphorus dose in Si, we present an improved model including oxygen depletion and dose saturation. This explains the experiments far better. We further couple this growth model with phosphorus diffusion and deactivation models in silicon, providing full modeling of the $POCl_3$ doping process.

There are two sets of samples analyzed in this chapter. The first set was prepared by Leibniz University of Hannover and University of Konstanz in Germany, and the second by Applied Materials Xi'an Solar Research Center. Dr. Zihua Zhu and Dr. Vaithiyalingam Shutthanandan in the Pacific Northwest National Laboratory took the SIMS and RBS data respectively. Hannes Wagner, Amir Dastgheib-Shirazi and Michael Kessler contributed to preparing the samples and conducting the ECV measurements. I have analyzed the data and built the continuum models.

6.1 Introduction

A solar cell typically consists of a p-n junction that is formed by a base and a emitter with opposite doping. Figure 6.1 illustrates the schematic of a solar cell in operation. Currently, solar cells with a p-type base and an n-type emitter dominate the market.

The emitter region of most crystalline Si solar cells is composed of phosphorus dopants, which are commonly introduced by forming a phosphorus rich glass layer via a $POCl_3$ source [90].

The phosphorus profile in the emitter region should be carefully controlled in order to achieve high-efficiency solar cells. On the one hand, a high surface concentration of phosphorus is required to reduce contact resistance; but on the other hand, the high surface concentration increases the surface recombination rate and thus produces a "dead layer", where light generated carriers can hardly be collected. Since blue light can't penetrate deep into the cell and is predominantly absorbed near the surface, the surface dead layer causes a poor "blue response". To overcome this design limitation, the selective emitter design was proposed before and has already been introduced to commercial production (e.g. Applied Materials, Dupont). This extra degree of freedom allows additional efficiency gain but also poses more challenges on process design optimization. Currently, new process conditions are usually found empirically, and it has proven to be very delicate to achieve a lower peak dopant density without sacrificing sheet resistivity and homogeneity. In this work the fundamental understanding of the $POCl_3$ doping process is improved by a combination of measurements and a newly developed theory. This enables us to support the change in processing conditions for high performance, high yield, and low cost.

When Si wafers are exposed to an atmosphere of $POCl_3$, O_2, and N_2, phosphosilicate glass (PSG) is formed. The glass is a mixture of P_2O_5 and SiO_2 [90]. This step is usually called *predeposition*, and the resulting PSG glass provides a source of phosphorus that diffuses into the Si wafer. Most commonly, an additional step, called *drive-in*, follows the predeposition. During drive-in, the supply of $POCl_3$ is disconnected, and a further amount of P diffuses into the wafer. Drive-in is commonly performed in a N_2 ambient, but some recipes also use O_2. The schematic of the deposition process is illustrated in Figure 6.2.

The experimental conditions of $POCl_3$ deposition can be characterized by four

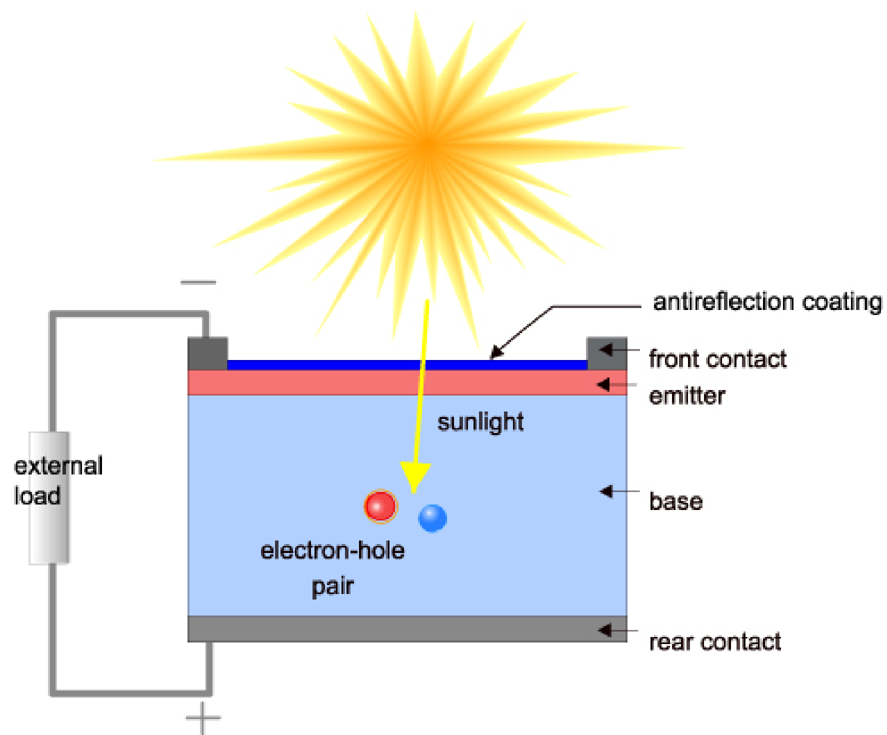

Figure 6.1: Schematic of a solar cell in operation. [7]

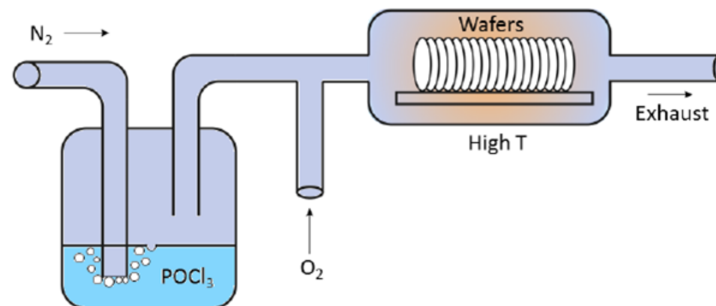

Figure 6.2: $POCl_3$ predeposition in an open tube furnace with a bubbler set-up. [8]

parameters: temperature, time, $POCl_3$ partial pressure, and O_2 partial pressure. The N_2 partial pressure does not directly affect the deposition process as N_2 is not the reacting gas species. Commonly, the partial pressures are not measured directly and are found by the corresponding gas flow rates, assuming a proportional relation between pressure and flow rate.

The growth behavior of PSG under ordinary conditions is commonly described as parabolic, with reported thickness values of 10-300 nm [91, 92]. We have performed investigations on PSG growth in the 5-40 nm thickness range, which is typical of current fabrication processes for improved emitters. Working closely with specialists in sample fabrication and characterization, we have analyzed doping profiles of samples under different deposition conditions and developed a set of models to fully describe the $POCl_3$ deposition process. The first set of samples provides a qualitative understanding of the deposition process. The second set of samples are used to calibrate model parameters to account for the profile dependence on two important parameters, predeposition time and $POCl_3$ partial pressure. Characterization of a third set of samples, fabricated by Applied Materials, is underway. This will allow further calibration of model parameters for accurate predictions of temperature and oxygen partial pressure dependence.

6.2 Experimental details

The chemical profiles in the wafer were measured with a time-of-flight secondary ion mass spectrometer (ToF-SIMS), using a 1 keV Cs^+ sputtering beam and a 25 keV Bi^+ analysis beam. We have mainly measured ion counts for ^{28}Si, ^{31}P, and ^{18}O. The observed ion count for ^{35}Cl is negligible, excluding any direct role of Cl_2 in PSG formation. Cl_2 forms volatile species and is transported out of the tube by the gas flow.

6.2.1 SIMS profiles of samples from the first set of samples

The first set of samples were doped by the standard $POCl_3$ process including predeposition and drive-in. Several splits have been generated, with variations of temperature, drive-in time, drive-in gas ambient, and drive-in gas flow rates. The SIMS profiles are shown in Figures 6.3, 6.4, 6.5, and 6.6.

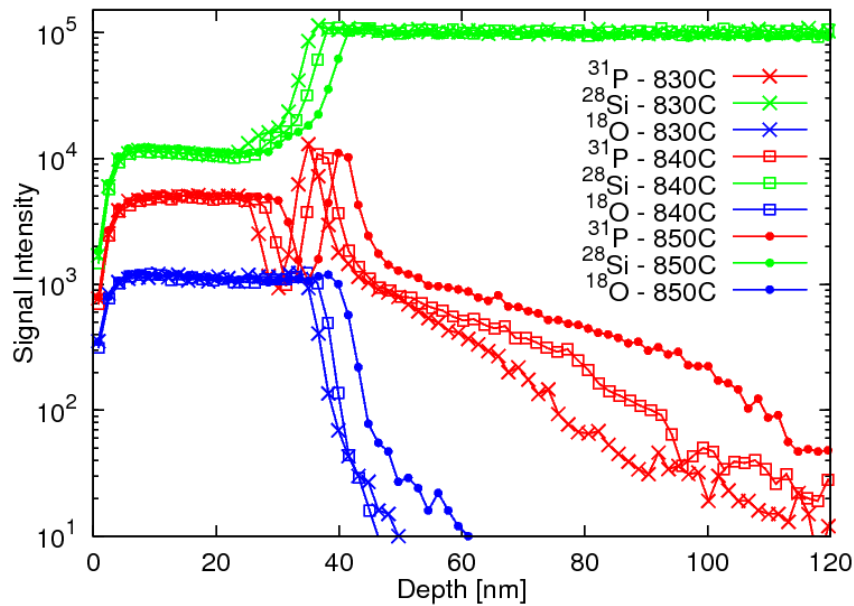

Figure 6.3: SIMS profiles of ^{28}Si, ^{31}P, and ^{18}O ions for varying predeposition and drive-in temperatures.

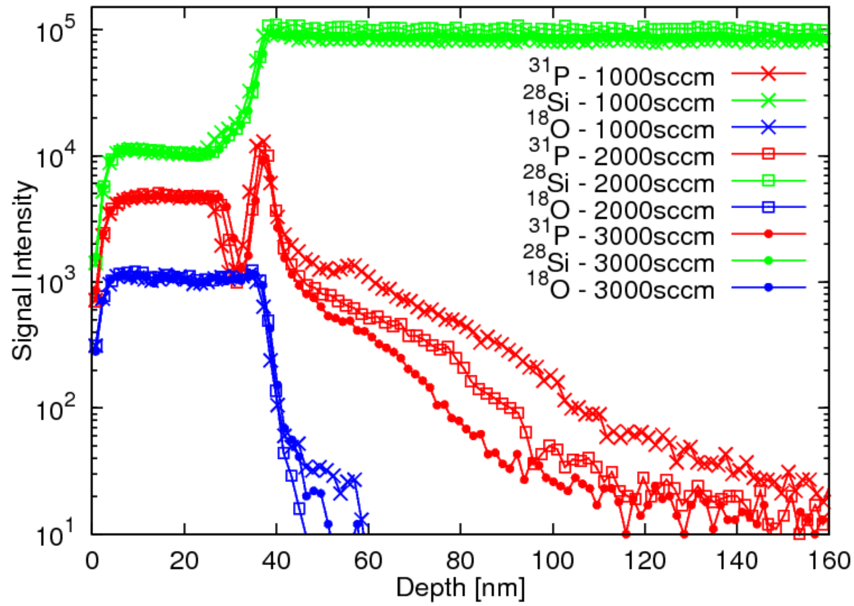

Figure 6.4: SIMS profiles of ^{28}Si, ^{31}P, and ^{18}O ions for varying O_2 flow rates.

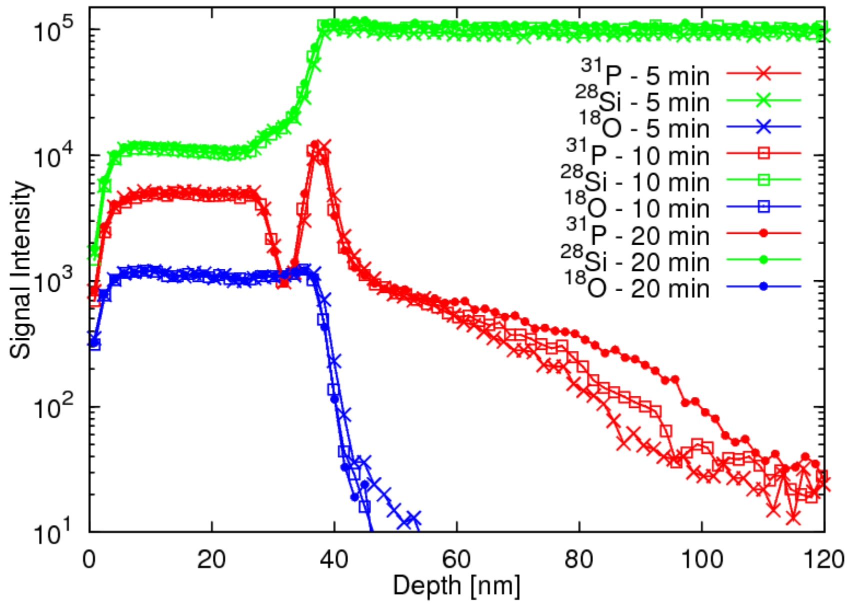

Figure 6.5: SIMS profiles of ^{28}Si, ^{31}P, and ^{18}O ions for varying drive-in times under N_2 ambient.

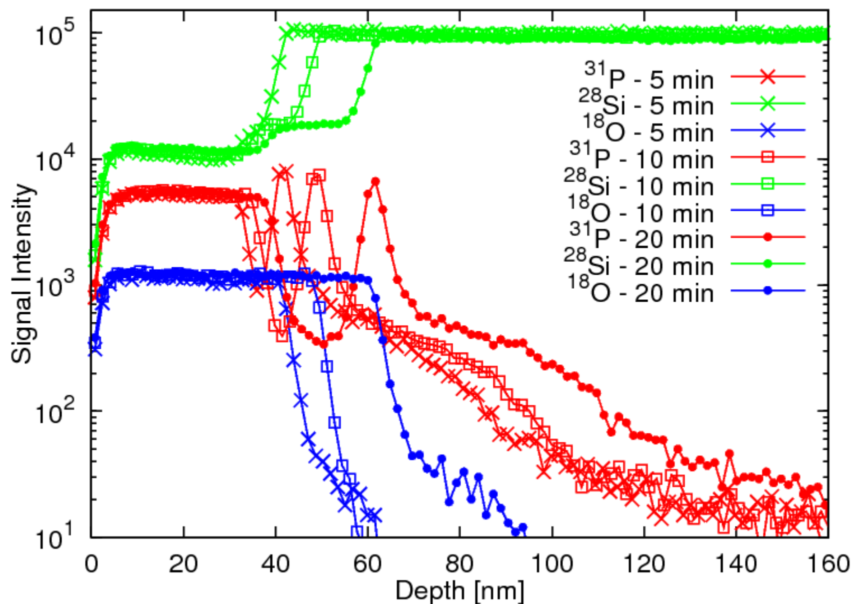

Figure 6.6: SIMS profiles of ^{28}Si, ^{31}P, and ^{18}O ions for varying drive-in times under O_2 ambient.

6.2.2 SIMS profiles of samples from the second set of samples

For the second set of samples, predeposition experiments were carried out at a fixed temperature of 840 °C in an atmosphere of O_2, N_2 and $POCl_3$ in a tube furnace, with $POCl_3$ supplied by a bubbler system kept at 20 °C under 1 atm. The O_2 flow rate is kept fixed at 250 sccm, while the $POCl_3$-carrying N_2 flow rate is varied among 250, 500, and 1000 sccm. A third N_2 flow is tuned to keep the total flow rate fixed at 10750 sccm. Predeposition time is varied among 10, 20, and 40 min. After predeposition, the samples were quickly removed from the furnace; hence no drive-in was performed. The signals are analyzed in three groups and are shown in Figures 6.7, 6.8, and 6.9.

The partial pressures of the reacting gases are assumed to be proportional to the gas flow rates. p_{O_2} is simply the ratio of O_2 flow rate to total gas flow rate. p_{POCl_3} is calculated as the product of the ratio of $POCl_3$-carrying N_2 flow rate to total gas flow rate and the saturated vapor pressure of $POCl_3$, which is 28 Torr (0.037 atm) at

Table 6.1: Determination of partial pressure from gas flow rates.

Flow rate (sccm)			Partial pressure (atm)		
$POCl_3$-carrying N_2	O_2	N_2	$POCl_3$	O_2	N_2
250	250	10250	9.76×10^{-1}	2.33×10^{-2}	8.88×10^{-4}
500	250	10000	9.75×10^{-1}	2.33×10^{-2}	1.78×10^{-3}
1000	250	9500	9.73×10^{-1}	2.33×10^{-2}	3.55×10^{-3}

20 °C [93]. Table 6.1 lists the partial pressures of gas species calculated from gas flow rates.

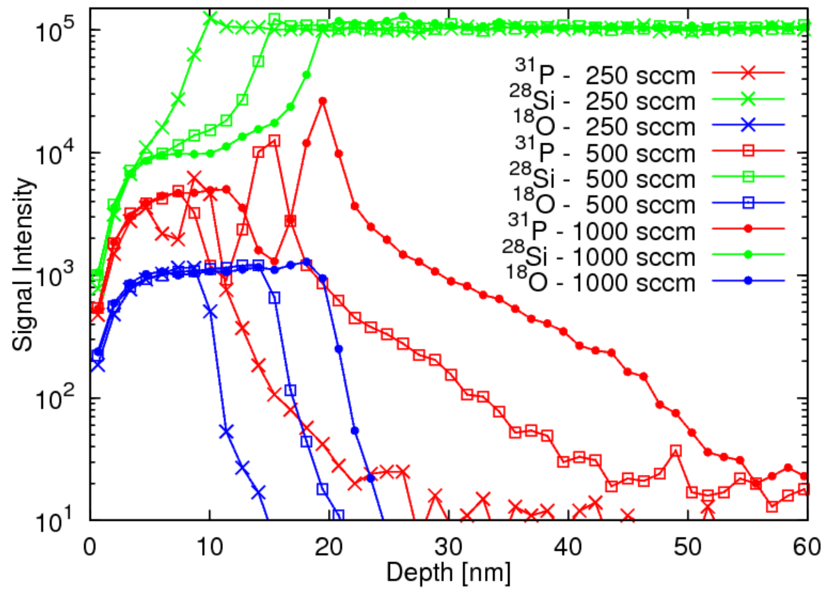

Figure 6.7: ToF-SIMS profiles of ^{28}Si, ^{31}P, and ^{18}O ions for varying $POCl_3$ flow rates at a predeposition time of 10 min.

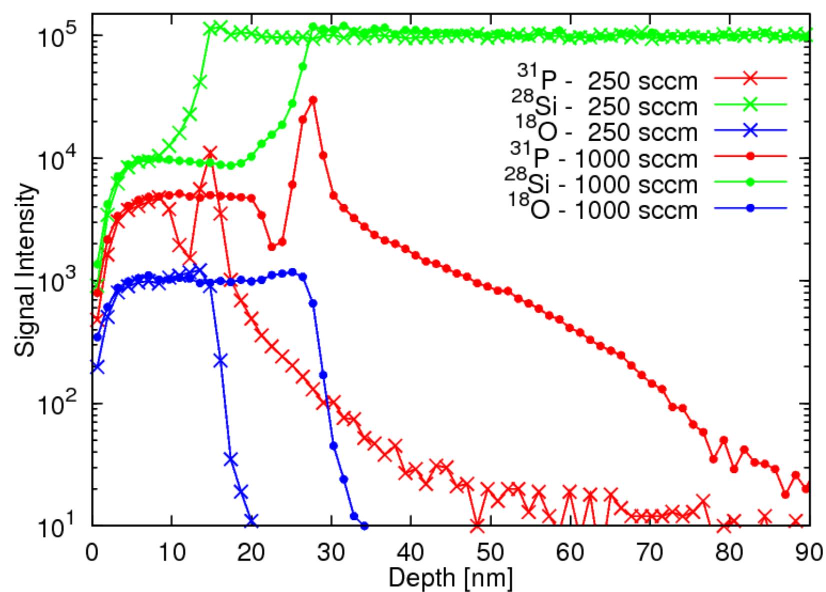

Figure 6.8: ToF-SIMS profiles of ^{28}Si, ^{31}P, and ^{18}O ions for varying $POCl_3$ flow rates at a predeposition time of 20 min.

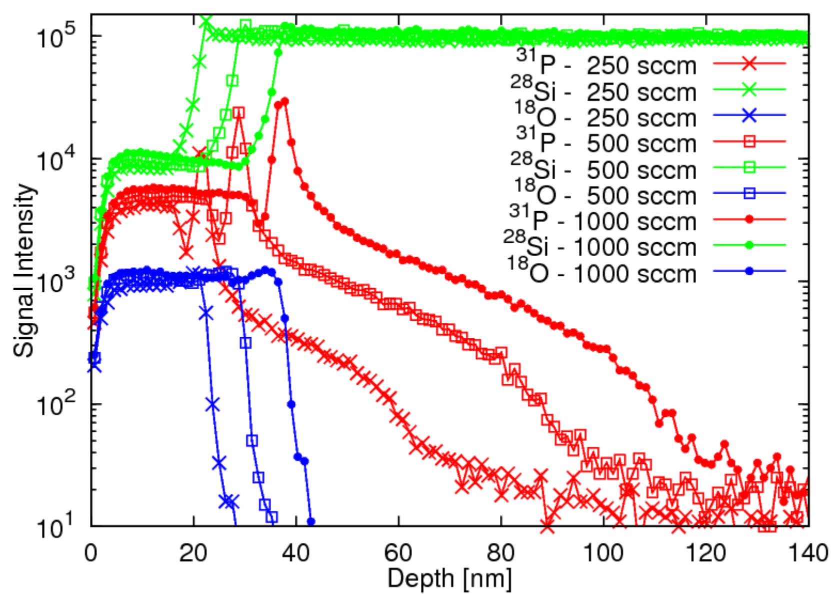

Figure 6.9: ToF-SIMS profiles of ^{28}Si, ^{31}P, and ^{18}O ions for varying $POCl_3$ flow rates at a predeposition time of 40 min.

6.3 Analyzing SIMS data

6.3.1 Layer identification

From the SIMS data, it appears that $POCl_3$ processing gives a bilayer structure, with a nearly uniform composition in the PSG region near the surface and a thin P-doped SiO_2 layer sandwiched between PSG and Si. This bilayer structure is confirmed by etch rate measurements in Ref. [92], where two different etch rates have been observed when etching the surface glass layer. Figure 6.10 plots a typical set of data with the layer boundaries indicated. The interface locations are determined by deconvolving the SIMS profiles with a Gaussian function having a standard deviation of roughly 1 nm.Comparing the relative signal strengths of ^{28}Si, ^{31}P, and ^{18}O for all samples, we found that the nearly uniform composition of the PSG is virtually independent of process conditions varied in this study (i.e. predeposition time and $POCl_3$ flow rate), despite the large impact of these process parameters on the P profiles in Si. Rutherford backscattering spectrometry (RBS) measurements give an average of 2.47 Si atoms for each P in the PSG, suggesting a formula approaching $(P_2O_5) \cdot 5(SiO_2)$. The formation of a bilayer in the P-doped glass grown from $POCl_3$ suggests phase separation. It has been found that for a wide temperature range (800 $\sim$ 1200 °C), the PSG composition falls onto the liquidus curve of the P_2O_5-SiO_2 phase diagram [92]. In the same reference, the composition of liquidus was reported to be 2P/5Si at around 850 °C, very close to our RBS measurements. This suggests that the PSG in our samples forms a eutectic liquidus. Another notable feature of the SIMS profiles is a large accumulation of P at the SiO_2-Si interface, which broadens into a Gaussian-like profile in Figure 6.10 due to surface roughness of samples and the SIMS broadening effect.

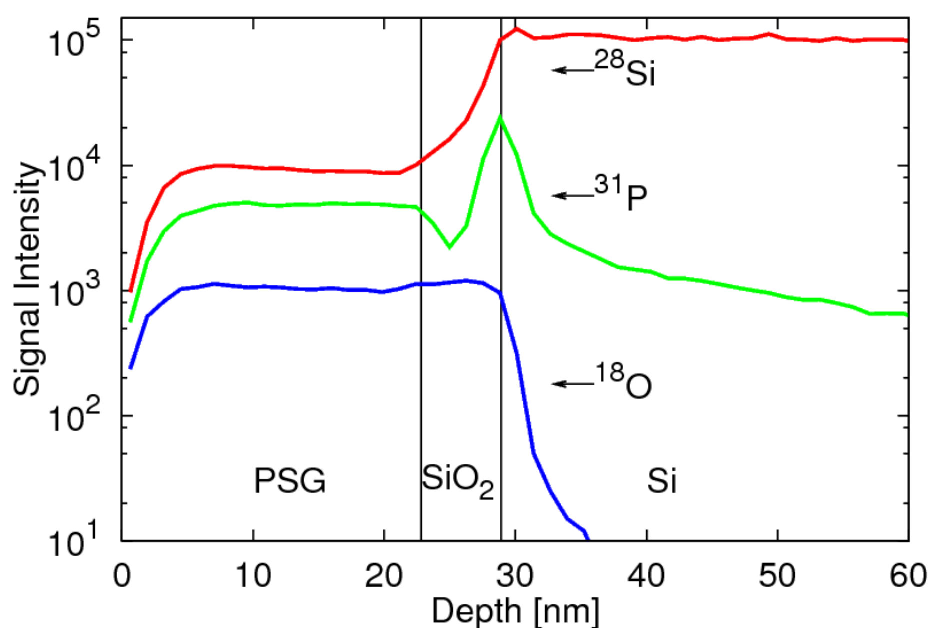

Figure 6.10: SIMS profiles of ^{28}Si, ^{31}P, and ^{18}O ions for $POCl_3$ flow rate of 500 sccm and predep time of 40 min. The two interfaces are determined by deconvolution of SIMS profiles. The systematic decrease of the profiles towards the surface is due to the SIMS transient artifacts.

6.3.2 Temperature dependence

Figure 6.3 shows the profiles for deposition with 3 different temperatures. It can be seen that the higher temperatures lead to faster PSG growth (thicker PSG) and more P diffused into Si. This indicates that the reactions rates for the PSG formation and phosphorus diffusion are both higher at higher temperatures. The composition of the PSG does not change as temperature varies.

6.3.3 Varying O_2 flow rates

Figure 6.4 shows the profiles for deposition with 3 different oxygen flow rates. It can be seen that higher oxygen flow leads to faster PSG growth, but less P diffusion. This looks surprising at first glance, but it can be explained by considering the role of

oxygen in PSG formation. If oxygen is involved in the PSG formation process, then higher oxygen flow will allow faster PSG growth, which consumes more phosphorus to form PSG, reducing the amount of phosphorus that further diffuses into Si. The composition of the PSG does not change as O_2 flow rate varies.

6.3.4 Comparing drive-in under N_2 and O_2 ambients

It is interesting to compare the behavior of PSG growth for drive-in under N_2 and O_2 ambients, as shown in Figures 6.5 and 6.6. Under N_2 drive-in ambient, with O_2 and $POCl_3$ supplies switched off, the PSG ceases to grow, and P in PSG diffuses into the Si region. However, under O_2 ambient, the PSG continues to grow even the $POCl_3$ supply is turned off. Also, the middle SiO_2 layer also grows. Comparison of the drive-in behavior under N_2 and O_2 ambients suggests that oxygen is directly involved in the reaction leading to PSG formation at the PSG-SiO_2 interface.

6.3.5 Quantitative analysis

Before using the second set of samples to quantitatively calibrate our model parameters, we need to convert SIMS ion count data to absolute concentrations. The SIMS profiles in the PSG are quantified based on the RBS measurements. The concentrations of P in the plateau region of the PSG is calculated to be 6.5×10^{21} cm^{-3}, using a PSG density of 2.36 g/cm^3 from Ref. [92]. Quantification of the SIMS profiles in Si is done by matching the SIMS profile in Si with that of the electrically active P measured by ECV. This leads to the following conversion formula

$$C_{\mathrm{P}} = \frac{I(^{31}\mathrm{P})}{I(^{28}\mathrm{Si})} \cdot 7 \times 10^{22}\ \mathrm{cm}^{-3} \tag{6.1}$$

where C_{P} is the total phosphorus concentration, $I(^{31}\mathrm{P})$ and $I(^{28}\mathrm{Si})$ are the SIMS ion counts for the associated species. Figure 6.11 illustrates the matching of SIMS profiles with ECV data.

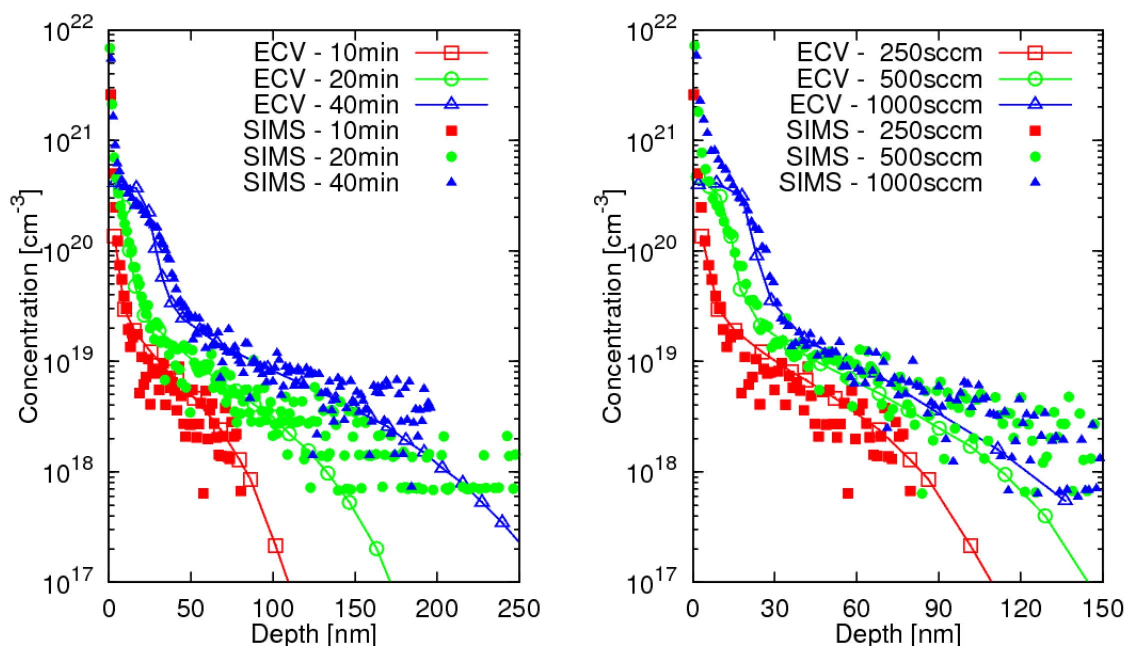

Figure 6.11: Matching SIMS data with ECV data for several different flow and predep time conditions. The two profiles were matched in the concentration regions of 1×10^{19} cm^{-3} to 2×10^{20} cm^{-3}. Left: predeposition times of 10, 20 and 40 min with a flow rate of 250 sccm. Right: Flow rates of 250, 500, and 1000 sccm with a predeposition time of 10 min.

The thicknesses of the PSG and SiO_2 layers are extracted from the SIMS profiles. The total P dose in Si is calculated by integration of the calibrated SIMS profiles over depth. The extracted PSG and oxide thickness and total dose are plotted in Figure 6.14 versus the square root of predeposition time for several $POCl_3$ flow rates. Both PSG thickness and total P dose show a roughly parabolic growth, consistent with previous findings [91, 92]; however, the lines do not extrapolate to the origin. Higher $POCl_3$ flows lead to thicker PSG and larger dose, but note that the dose depends more strongly than the thickness on the $POCl_3$ flow. The thickness of the SiO_2 layer remains near 6 nm for all the process conditions observed. It is possible that initially the oxide grows very fast, and then its thickness stays relatively the same due to a balance between reactions at the front and back interfaces.

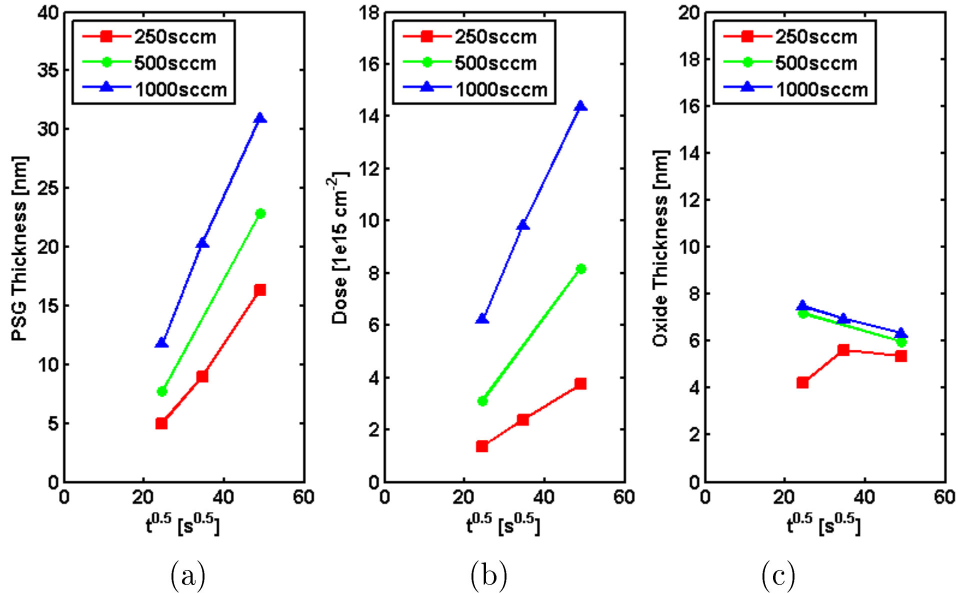

Figure 6.12: Growth of (a) PSG thickness, (b) total P dose in Si, and (c) SiO_2 thickness under different $POCl_3$ flow rates, as extracted from Figures 6.7, 6.8, 6.9 and 6.11. The data point for flow rate of 250 sccm and 10 min in (c) has large uncertainty as a result of uncertainties in the interface locations due to low dose. Solid lines are a guide to the eyes.

6.4 Model implementation

Based on the above analysis, we present steady-state models to quantitatively understand the growth behavior of PSG thickness and the dose of phosphorus in Si. We assume that there are two parallel processes, one for phosphorus and the other for oxygen. The schematic of the model is shown in 6.13. There are two parallel processes in the system: one for P and the other for O. At the PSG-SiO_2 interface, part of P and O react to form PSG at the expense of dissolving SiO_2 underneath. The rest of P and O segregate across the interface and continue to diffuse. At the SiO_2-Si interface, oxygen completely reacts with the Si layer below and forms SiO_2, while P either gets trapped into the surface or diffuses further into Si. The net SiO_2 growth is the growth at its back side by the reaction of O_2 and Si, subtracted by the

consumption of SiO_2 at its front side to form the PSG layer.Arrows denote the net flows of P (brown) and O (blue). J_D, J_S, and J_R denote fluxes of diffusion, segregation and reaction respectively. Also shown in the schematic are critical interface concentrations, in which atom species (P and O) are denoted by subscripts, and the associated regions are denoted by superscripts (G stands for PSG and X stands for oxide). An apostrophe in the superscript is added to distinguish the concentration at the bottom interface from that at the top. For the sake of simplicity, we do not include the kinetics of the SiO_2 growth; rather, we assume a constant SiO_2 thickness as measured.

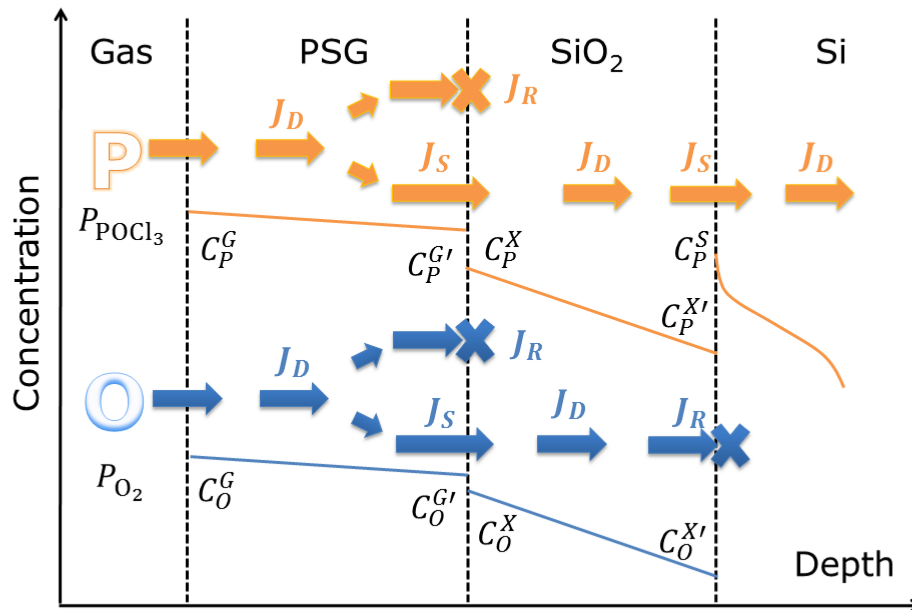

Figure 6.13: Model schematic with critical concentrations at interfaces. Subscripts denote atom species, and superscripts denote the associated regions (G stands for PSG and X stands for oxide). An apostrophe in the subscript is added to distinguish the concentration at the bottom interface from that at the top. Arrows denote the net flows of P (brown) and O (blue). J_D, J_S, and J_R denote fluxes of diffusion, segregation and reaction respectively.

1. Simple linear-parabolic growth model

A simple linear-parabolic growth model of the PSG layer can be derived as follows. Assuming a complete reaction of $POCl_3$ and O_2, then according to Henry's law, the phosphorus and oxygen concentrations at the top PSG surface are proportional to the partial pressures of $POCl_3$ and O_2 respectively:

$$C_P^G = H_P p_{\mathrm{POCl_3}} \tag{6.2}$$

$$C_O^G = H_O p_{\mathrm{O_2}} \tag{6.3}$$

where H_P and H_O are Henry constants for $POCl_3$ and O_2 respectively. Eq. (6.3) implies that the diffusing O species is molecular rather than atomic. The partial pressures of the reacting gases are calculated in Table 6.1.

The mobile phosphorus species diffuses through the PSG and reaches the PSG-SiO_2 interface, where part of the excess phosphorus reacts with SiO_2 to form PSG, while the rest segregates into the SiO_2 and continues to diffuse. Based on the conservation principle, the diffusion flux across PSG should equal the reaction flux at the PSG-SiO_2 interface plus the diffusion flux across SiO_2:

$$J^D_{P(PSG)} = J^D_{P(Ox)} + J^R_{P(PSG/Ox)} \tag{6.4}$$

Under steady state conditions, the concentration of excess phosphorus inside PSG and SiO_2 varies linearly with depth. The reaction flux at the PSG-SiO_2 interface is proportional to the the phosphorus and oxygen contents on the PSG side, denoted $C_P^{G'}$ and $C_O^{G'}$ respectively. We can thus write Eq. (6.4) as

$$D_P^G \frac{C_P^G - C_P^{G'}}{x_G} = D_P^X \frac{C_P^X - C_P^{X'}}{x_X} + k_P^R C_P^{G'} C_O^{G'} \tag{6.5}$$

where k_P^R is the equilibrium constant for the reaction, D_P^G and D_P^X are phosphorus diffusivities in PSG and oxide, x_G and x_X are the thickness of PSG and oxide. Remember that an apostrophe in the superscript is added to distinguish the concentrations on the two sides of the film.

The phosphorus in SiO_2 crosses the SiO_2-Si interface, and then either gets trapped beneath the interface, or diffuses further into Si. Assuming perfect sink at the interface, the flux across the SiO_2-Si interface can be written as $k_P^{S2} C_P^{X'}$, where k_P^{S2} is the kinetic factor of P segregation at the SiO_2-Si interface. Again based on conservation principle, this quantity should equal the diffusion flux in SiO_2:

$$D_P^X \frac{C_P^X - C_P^{X'}}{x_X} = k_P^{S2} C_P^{X'} \tag{6.6}$$

Assuming rapid segregation across the PSG-SiO_2 interface, the phosphorus concentrations of phosphorus at the two sides of the interface are proportional throughout the entire deposition process:

$$C_P^X = r_P^{S1} C_P^{G'} \tag{6.7}$$

where r_P^{S1} is by definition the segregation coefficient at the PSG-SiO_2 interface. Combining Eqs. (6.5) - (6.7) we can solve $C_P^{G'}$ in terms of C_P^G

$$C_P^{G'} = \frac{C_P^G}{\left(\frac{k_P^R}{D_P^G} C_O^{G'} + \frac{r_P^{S1} D_P^X}{x_G D_P^G} \right) x_G + 1} \tag{6.8}$$

To efficiently incorporate Henry constants into the lumped parameters, we define "pressure" terms $p_P^{'}$ and $p_O^{'}$ such that

$$C_P^{G'} = H_P p_P^{'} \tag{6.9}$$

$$C_O^{G'} = H_O p_O^{'} \tag{6.10}$$

With this change of variables from $C_P^{G'}$ and $C_O^{G'}$ to $p_P^{'}$ and $p_O^{'}$ respectively, we can rewrite Eq. (6.8) in terms of $p_P^{'}$ and $p_O^{'}$:

$$p_P^{'} = \frac{p_{\mathrm{POCl_3}}}{\left(K_1 p_O^{'} + K_2\right) x_G + 1} \tag{6.11}$$

where K_1 and K_2 are lumped fitting parameters as defined in Table 6.2. The time derivative (growth) of the dose and the PSG thickness are proportional to the first and second terms on the right hand side of Eq. (6.5) respectively:

$$\frac{dx_G}{dt} = K_0 p_P^{'} p_O^{'} \tag{6.12}$$

$$\frac{dQ_P}{dt} = \left(\frac{K_0 K_2}{K_1} N_P\right) p_P^{'} \tag{6.13}$$

where K_0 is another lumped parameter. N_P is a constant, being the number of P atoms incorporated per unit volume of PSG grown, with a value of 6.5×10^{21} cm^{-3} extracted from our RBS measurements. The definitions of all model parameters are shown in Table 6.2, with values obtained by the least square fitting method.

Assuming that oxygen diffuses fast enough through PSG, we have $C_O^{G'} = C_O^G$, and thus $p_O^{'} = p_{\mathrm{O_2}}$, independent of the PSG thickness x_G. Integration of Eqs. (6.8, 6.12) leads to a linear-parabolic growth model for both the PSG thickness and the dose, with the growth rates ($\frac{dx_G}{dt}$, $\frac{dQ_P}{dt}$) both proportional to $p_{\mathrm{POCl_3}}$, which is in turn proportional to the $POCl_3$ flow rate. This implies that the PSG thickness and P dose will have the same dependence on the $POCl_3$ flow rate. Such a linear-parabolic model was originally developed to account for the growth kinetics of SiO_2 on Si substrates [94, 76]. However, in the PSG system, it cannot explain an important observation: the larger dependence of dose on $POCl_3$ flow compared to that of the PSG thickness. This is evident when fitting Eqs. (6.8) - (6.13) to experiment, shown as dashed lines in Figure 6.14.

The reason for the unsatisfactory fits of the linear-parabolic model is two-fold: (a)

Table 6.2: Definition and values of lumped parameters for the simple and improved models obtained by fitting the experimental data via the least square method. The simple model has 3 lumped parameters: K_0, K_1, and K_2. The improved model has 3 additional parameters: K_3, K_4, and K_5. H_P and H_O are Henry constants associated with $POCl_3$ and O_2 respectively. The phosphorus and oxygen concentration at the top PSG surface is calculated as $C_P^G = H_P\, p_{\mathrm{POCl_3}}$, $C_O^G = H_O\, p_{\mathrm{O_2}}$, where p denotes the partial pressure (in atm) of the gases. k_P^R is the equilibrium constants for the reaction at the PSG-SiO_2 interface as defined in Eq. (6.5), and k_O^R is the corresponding constant for oxygen. r_P^{S1} and r_P^{S2} are segregation coefficients of P at the PSG-SiO_2 and SiO_2-Si interfaces respectively. Diffusivities are denoted by D, with subscript indicating species (P, O) and superscript indicating region (G stands for PSG and X stands for oxide). x_X is the thickness of the oxide (treated as a fixed parameter). λ is the ratio of the P dose in Si to the peak P concentration in Si. N_P is the number of P atoms incorporated per unit volume of PSG grown, with a value of 6.5×10^{21} cm^{-3} extracted from our RBS measurements.

Parameter	Definition		Value		Unit
	Simple model	Improved model	Simple model	Improved model	
K_0	$\frac{k_P^R H_O H_P}{N_P}$		4.50×10^{-5}	4.41×10^{-5}	$\mathrm{cm \cdot s^{-1} \cdot atm^2}$
K_1	$\frac{k_P^R H_O}{D_P^G}$		2.88×10^7	1.06×10^7	$\mathrm{cm^{-1} \cdot atm}$
K_2	$\frac{r_P^{S1} D_P^X}{x_X D_P^G}$		4.30×10^5	1.44×10^5	$\mathrm{cm^{-1}}$
K_3	− − −	$\frac{D_P^X}{\lambda r_P^{S2} D_P^G x_X H_P}$	− − −	1.84×10^{-14}	$\mathrm{cm \cdot atm^{-1}}$
K_4	− − −	$\frac{k_O^{R1} H_P}{D_O^G}$	− − −	2.99×10^8	$\mathrm{cm^{-1} \cdot atm}$
K_5	− − −	$\frac{r_O^{S1} D_O^X}{x_X D_O^G}$	− − −	2.73×10^3	$\mathrm{cm^{-1}}$

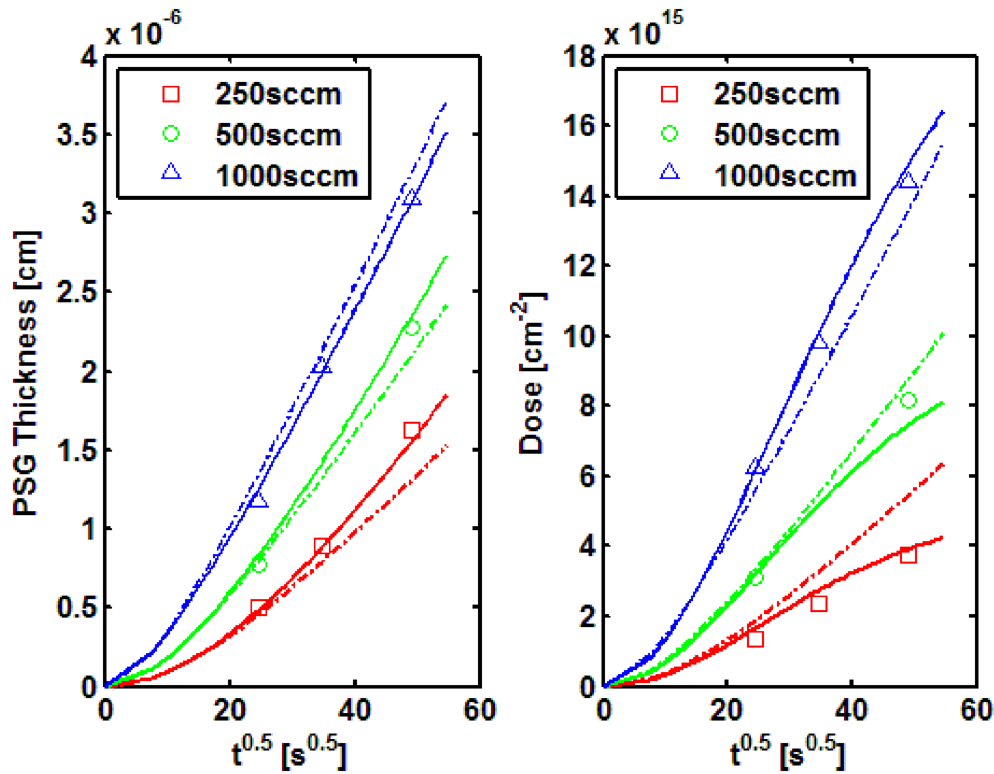

Figure 6.14: Growth of PSG thickness and phosphorus dose under different $POCl_3$ flow rates. Points: data from SIMS, dashed lines: fit from the simple linear-parabolic model, solid lines: fit from the improved model.

the inappropriate assumption of perfect sink, as a significant amount of phosphorus accumulates at the SiO_2-Si interface; and (b) neglecting the depletion of oxygen due to PSG formation at the PSG-SiO_2 interface. Qualitatively, higher $POCl_3$ flow rates lead to faster PSG growth, which in turn depletes the oxygen concentration. As oxygen is involved in the PSG formation at the interface, this allows less phosphorus to react with SiO_2 and form PSG, and thus more P to diffuse in and contribute to the dose in Si. This slows down the PSG growth rate, and accelerates the dose, as derived in the following.

2. Improved growth model

We first drop the assumption of perfect sink at the SiO_2-Si interface and assume that the peak phosphorus concentration in Si, denoted C_P^S, is proportional to the phosphorus dose in Si, denoted Q_P. Further assuming fast segregation at the SiO_2-Si interface, we get:

$$C_P^{X'} = \frac{Q_P}{\lambda r_P^{S2}} \tag{6.14}$$

where r_P^{S2} is the segregation coefficient of P at the PSG-SiO_2 interface, and λ is the ratio of P dose in Si to peak P concentration in Si. Combining Eqs. (6.5), (6.6) and (6.14), and again replacing $C_P^{G'}$ and $C_O^{G'}$ with $p_P^{'}$ and $p_O^{'}$, we obtain an expression for $p_P^{'}$ different from that of the simple model as in Eq. (6.11):

$$p_P^{'} = \frac{p_{\mathrm{POCl_3}} + K_3 x_G Q_P}{\left(K_1 p_O^{'} + K_2\right) x_G + 1} \tag{6.15}$$

where K_1, K_2, and K_3 are given in Table 6.2.

The oxygen process is parallel to that of phosphorus, except that O reacts with Si at the SiO_2-Si interface, rather than segregating into Si. Performing a similar analysis for the oxygen fluxes, we obtain an expression for $p_O^{'}$ similar to Eq. (6.11):

$$p_O^{'} = \frac{p_{\mathrm{O_2}}}{\left(K_4 p_P^{'} + K_5\right) x_G + 1} \tag{6.16}$$

where K_4 and K_5 are lumped parameters. The parameter values are again obtained by least-square fitting and are listed in Table 6.2.

Solving Eqs. (6.15) and (6.16), we get expressions for $p_P^{'}$ and $p_O^{'}$ in terms of x_G and Q_P. The two differential equations for the growth of PSG thickness and dose in Si now become

$$\frac{dx_G}{dt} = K_0 p_P^{'} p_O^{'} \tag{6.17}$$

$$\frac{dQ_P}{dt} = \left(\frac{K_0 K_2}{K_1} N_P\right)\left(p_P^{'} - \frac{K_3}{K_2} Q_P\right) \tag{6.18}$$

The negative term in Eq. (6.18) provides a saturation scheme for the growth of dose at longer times. Plugging in expressions for $p_P^{'}$ and $p_O^{'}$ obtained from solving Eqs. (6.15) and (6.16) and integrating Eqs. (6.17) and (6.18) numerically, we get solutions that substantially improve the fit to the experimental data shown in Figure 6.14 as solid lines.

6.5 Coupling with phosphorus diffusion and deactivation models in Si

The growth model gives the quantitative time dependence of phosphorus flux into Si, which is simply the right hand side of Eq. (6.18). Using the calculated flux $\frac{dQ_P}{dt}$ in Eq. (6.18) as the boundary condition at the SiO_2-Si interface, we further couple this growth model to the process models in Si described in Chapter 5, which include the pair diffusion models [5, 29], a phosphorus-vacancy clustering model, and a model for segregation of P to the SiO_2-Si interface [89]. Combining all these models, we are able to predict the diffused profiles of P in Si for various process conditions. The predicted emitter profiles in comparison with ECV measurements for predeposition time of 10, 20 and 40 min at 840 °C are plotted in Figure 6.15. From the plot, we can see that the predicted profiles from coupling the models agree well with the experimental data for longer predeposition times (20 min and 40 min). The deviation between model prediction and experimental data for the 10 min data may be due to the assumption of constant oxide thickness. Initially, oxide is very thin and thus allows more phosphorus to diffuse into the wafer. Fixing oxide thickness at 6 nm tends to underestimate the amount of phosphorus diffused into Si, causing a shallower tail in the emitter.

6.6 Summary

We have analyzed the concentration profiles and growth kinetics of phosphosilicate glass (PSG) for different gas flow rates in the $POCl_3$ deposition process. Time-of-flight (ToF) SIMS measurements indicate that a PSG layer forms during predeposition, whose composition is nearly independent of process conditions. We also observe a

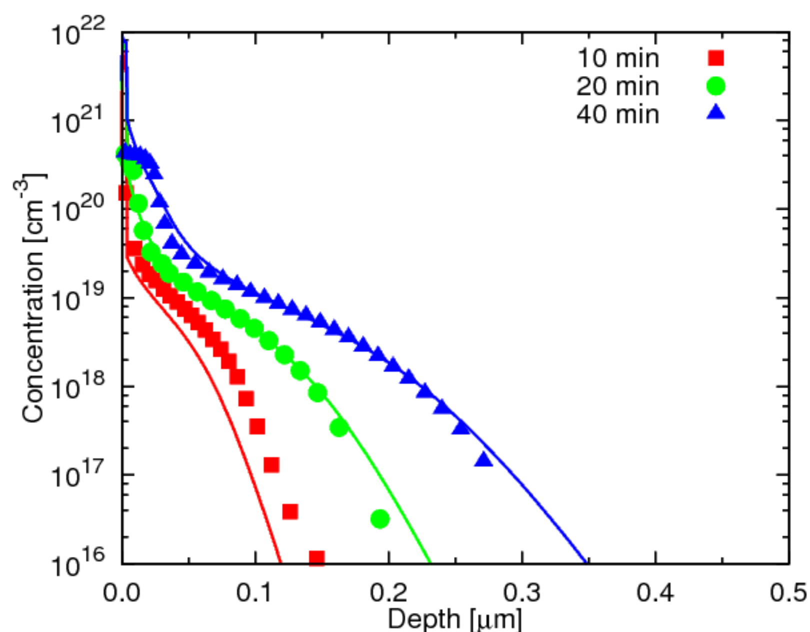

Figure 6.15: Comparison between simulated (lines) and experimental values measured by ECV (symbols) of phosphorus profiles for a $POCl_3$ flow rate of 250 sccm and deposition times of 10, 20, 40 min.

thin layer of SiO_2 sandwiched between the PSG and Si, and a strong accumulation of P at the SiO_2-Si interface. We have developed a growth model for $POCl_3$ deposition process that includes oxygen depletion and dose saturation. The predicted kinetics of PSG thickness and dose of diffused P into Si are in agreement with experimental data. We further couple this model with established diffusion models in Si and calculate the resulting emitter profiles, which agree well with experiments. This set of coupled models provides full modeling of the $POCl_3$ deposition process commonly used for emitter formation, and allows optimization of emitter diffusion to achieve solar cells with high performance, high yield, and low cost.

Chapter 7

DIFFUSION AND GETTERING OF METAL SPECIES

This chapter is adapted from a manuscript to be submitted for publication. Bart Trzynadlowski has contributed to the DFT calculations of metal binding to dislocations.

7.1 Introduction

Metal contamination in silicon has a detrimental effect on device performance. Metals are fast diffusers in silicon, with diffusivities many orders of magnitude larger than common dopants [76]. For this reason, metal contaminants can diffuse and redistribute throughout the whole wafer. Dissolved metals often possess many deep energy levels and are thus effective generation-recombination centers that deteriorate carrier lifetime. In silicon, generation and recombination processes predominately occur through the Shockley-Hall-Read (SHR) mechanism[95, 96]. The SHR generation and recombination rate is given as [97]

$$U = \frac{pn - n_i^2}{\tau_{n0}\left[p + n_i \exp\left(\frac{E_i - E_t}{kT}\right)\right] + \tau_{p0}\left[n + n_i \exp\left(\frac{E_t - E_i}{kT}\right)\right]} \tag{7.1}$$

where E_i is the intrinsic Fermi level located at mid-gap, and E_t is the trap level of the defect. τ_{n0} and τ_{p0} are carrier lifetime parameters defined as

$$\tau_{n0} = \frac{1}{N_t v_{th} \sigma_n} \tag{7.2}$$

$$\tau_{p0} = \frac{1}{N_t v_{th} \sigma_p} \tag{7.3}$$

where v_{th} is the thermal velocity, N_t is the concentration of centers, and σ_n and σ_p are the capture cross-section of electrons and holes. Eqs. (7.2, 7.3) describe the minority carrier lifetime in the material, which is inversely proportional to the density of generation-recombination centers (usually abbreviated as "recombination centers"). Under carrier excess conditions, $pn > n_i^2$ and U is the rate of carrier recombination. Under carrier deficit conditions, $pn < n_i^2$ and U is the rate of carrier generation.

There are many ways of contamination during the device manufacturing process, such as mechanical contact between the wafer and a metal, contact of wafer with contaminated liquid solutions for wafer cleaning, and vapor-phase contamination during oxidation, evaporation and sputtering [98]. Using cleaner materials and adopting cleaner processes can reduce impurity content to some extent, but it is simply not cost-effective to keep the levels below the ppb range using "cleaner" technologies. Another approach is called *gettering*, a process to remove unwanted contaminants away from the active device region so that they do minimum harm to device performance.

The idea of gettering lies in the fact that metals in silicon prefer to stay at or close to lattice imperfections, such as clusters, extended defects, and other precipitates. There are two gettering methods that are widely used: (a) extrinsic gettering, and (b) intrinsic gettering [76, 99]. Extrinsic gettering introduces gettering sites by mechanical damage [100, 101, 96] , substrate doping [102, 103, 104], and ion implantation [103, 105, 9] processes. Dislocations generated by ion implantation are common sites for metals to decorate. Intrinsic gettering uses the oxygen in Czochralski silicon to form SiO_2 precipitates and other extended defects under certain thermal conditions.

In this chapter, we focus on phosphorus diffusion gettering. To understand the gettering behavior, DFT calculations are carried out for various metal species, and their binding to phosphorus-vacancy complexes, which are assumed to be the dominating species under high doping conditions in Chapter 5. We focus on the properties of the seven most common transition metal contaminants in silicon devices (Ti, Cr, Fe, Ni, Cu, Mo, and W). Among these metals, 5 are 3d transition metals (Fe, Cu,

Figure 7.1: Periodic table including the transition metals included in this study (shaded).

Cr, Ni, Ti). The other 2 (Mo, W), together with Cr, belongs to the VIB group. The metals considered in this chapter are shown in shades on the periodic table in Figure 7.1.

7.2 Numerical details

All the *ab initio* calculations were done using the density functional theory (DFT) code VASP [13, 14, 15, 16] with the Perdew-Wang 1991 generalized gradient approximation functional [39] and ultrasoft Vanderbilt-type pseudopotentials [40, 41]. Calculations are performed in a nominally 64-atom supercell. A $2 \times 2 \times 2$ Monkhorst-Pack [18] k-point mesh for integrations over the Brillioun zone and a 400 eV energy cutoff in the plane-wave expansions are used throughout the calculations. The GGA equilibrium lattice constant of 5.4566 Å [65] were used and kept fixed throughout the calculations.

7.3 Favorable configurations and electric levels

Generally, transition metals mainly occupy interstitial sites and as the atomic number increases there's an increasing tendency to occupy substitutional lattice sites [106] . Ti, Cr and Fe mainly occupy interstitial sites, while substitutional defects have

been observed for Ni and Cu. Ni interstitial has no electric activity [107, 108]. It is also observed that Mo and W mainly occupy interstitial sites. We have done total energy calculations of various metal configurations with different charge states for these metals. To partially correct for the band-gap problem, we assume that donor levels scale with the valence band maximum and acceptor levels scale with the conduction band minimum when the band-gap opens up to the experimental value. Calculation indicates that metals prefer to occupy tetrahedral lattice sites, consistent with previous findings [106]. The calculated electric levels of these defects are shown in Table 7.1 in comparison with experimental measurements. We can see that the calculations give reasonable agreements with the experiment observations. DFT predicts that VIB group metals (Cr, Mo, W) have only a deep donor level in the band gap, with level locations very close to experimental findings within 0.1 eV. It gives a single and double donor level for Ti, consistent with experiments. The prediction of acceptor level for Ni is 0.16 eV shallower than the experiments, and it fails to give a deep donor level for this defect. The prediction of Fe and Cu levels is within 0.2 eV of that observed experimentally. The deviation from experimental findings might be due to the potentials used in the DFT calculations. Generally, projector augmented-wave pseudo-potentials [109, 110] give better results of electric levels than ultrasoft potentials because the radial cutoffs are smaller and the PAW potentials reconstruct the exact valence wavefunction [111].

7.4 Phosphorus diffusion gettering of metal species

We have performed DFT calculations on the binding energy of metals to various phosphorus species in Si. The results, listed in Table 7.2, indicate that metals do not bind with substitutional phosphorus at all, except a weak binding between Cr and P_S. This challenges the foundation of continuum models [112] that assume a strong binding of iron and substitutional phosphorus. On the other hand, metals exhibit strong binding with P_nV clusters. The binding to P_nV decreases as n becomes larger,

Table 7.1: Calculated deep transition levels of the metal interstitials in comparison with experimental values (unit: eV). d, dd, and a denote donor, double donor, and acceptor levels respectively. Donor levels are referenced to the valence band maximum and acceptor levels are referenced to the condution band minimum.

Metal	Level type	Calculated Levels	Experimental Levels [98]
Ti_T	d	+0.74	+0.85
	dd	+0.38	+0.28
Cr_T	d	+0.82	+0.90
Mo_T	d	+0.25	+0.28
W_T	d	+0.30	+0.40
Fe_T	d	+0.19	+0.39
Ni_S	d	−−	+0.17
	a	-0.25	-0.41
Cu_S	d	+0.11	+0.22
	a	-0.47	-0.66

but since the formation energy of P_nV clusters themselves decrease much faster as n becomes larger, M-P_4V will be the dominant complex under high P concentration. We also find that no gap states exist for this cluster, suggesting that M-P_4V is the gettered inactive M complex. The gettering mechanism can be described by the reaction

$$\mathrm{M} + \mathrm{P_4V} \Longleftrightarrow \mathrm{M} - \mathrm{P_4V} \tag{7.4}$$

7.4.1 Gettering behavior under phosphorus implants

Experimental data [9] indicate that under phosphorus implants, some metals (Ni, Cu) segregate to high P content region, while others (Fe, Cr) segregate to the end-of-range region, a region of high concentration of dislocation cores. Such dislocation cores are formed from initial damage caused by phosphorus implantation during damage annealing. Figure 7.2 shows the gettering behavior for various metals under phosphorus implants.

Table 7.2: Binding energy of metals to various phosphorus species (unit: eV). When a metal binds with a P_nV cluster, it occupies the vacancy site. The values are referenced to isolated tetrahedral metal and neutral phosphorus species. Negative values indicate binding, while positive values indicate repulsion.

	P_S	P_1V	P_2V	P_3V	P_4V
Cr	-0.22	-3.11	-2.48	-2.23	-1.99
Cu	-0.07	-3.25	-3.17	-3.19	-2.36
Fe	-0.02	-2.75	-2.44	-2.30	-1.52
Mo	0.01	-2.41	-2.29	-1.80	-0.90
Ni	-0.10	-2.84	-2.56	-2.34	-1.92
Ti	-0.08	-2.57	-2.39	-2.12	-1.53
W	0.09	-2.70	-2.55	-2.05	-1.22

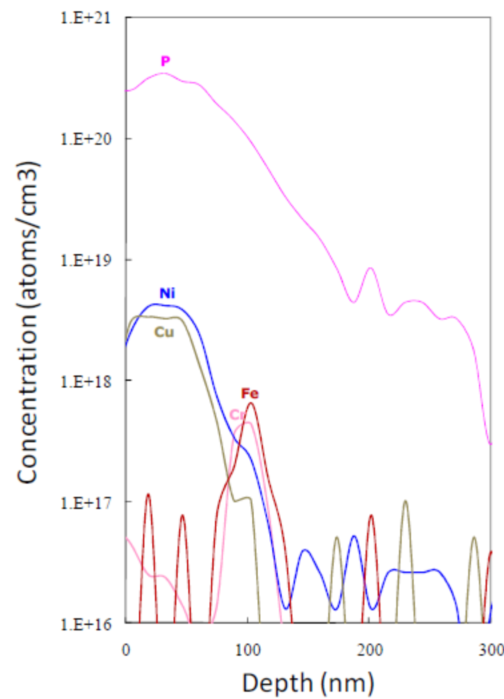

Figure 7.2: SIMS depth profiles of silicon wafers implanted with phosphorous followed by annealing [9].

Table 7.3: Comparison of binding to P_4V and dislocation cores for various metal species (unit: eV). Calculations of binding to dislocation cores were done by Bart Trzynadlowski.

	P_4V	Dislocation cores
Cr	-2.21	-1.14
Cu	-2.41	-0.82
Fe	-1.57	-1.85
Mo	-1.00	-1.07
Ni	-1.93	-1.19
Ti	-1.49	-3.40
W	-1.24	-1.50

As dislocation cores provide additional gettering sites, there is a competition between phosphorus gettering and dislocation gettering. Binding of metals to dislocation cores were also investigated and shown in comparison to binding to P_4V in Table7.3. The DFT predictions are in agreement with experimental observations in Ref. [9]. Our calculation results indicate that Ni and Cu have a larger binding to P_4V, consistent with the segregation of Ni and Cu to high phosphorus content region as observed. The tendency of Fe to segregate to dislocations are also consistent with a higher binding to the dislocation cores. There seems to be discrepancy of Cr between experiments and DFT values. The reason for this might be that DFT fails to find the most stable decoration site for Cr to sit on dislocations, due to the many available sites present. The DFT also predicts that Ni may segregate to P_4V while Mo and W have comparable segregation tendencies to both traps.

Chapter 8

INTRINSIC DEFECTS AND IMPURITIES IN β-GA_2O_3

This chapter is the result of a collaboration between Tracy C. Lovejoy in the Olmstead/Ohuchi group and me. I did all the related VASP calculations, but Tracy and I worked together to decide on which calculations to do, and interpret the calculation results. The experimental findings mentioned in the chapter to compare with DFT results were all carried out by Tracy. The details can also be found in Tracy's thesis [113]. The DFT results, together with experimental findings, were published in *Applied Physics Letters* and *Journal of Applied Physics* [114, 115].

8.1 Introduction

Wide band gap semiconductors have many interesting properties and can be used in many applications such as gate insulators, transparent conductors and chemical sensors. β-Ga_2O_3, with a large band gap of 4.9 eV [116] and thermal stability up to its melting point [117], has attracted considerable attention for potential applications in transparent conductive materials [118, 119], ultraviolet photodetectors [120, 121], gas sensors [122, 123], and dilute magnetic semiconductors [124, 125]. Successful application of β-Ga_2O_3 based devices requires atomic-scale understanding of the source of conductivity under both intrinsic and doped conditions.

8.2 β-Ga_2O_3 crystal structure

β-Ga_2O_3 has a base-centered monoclinic crystal structure with lattice parameters $a = 12.23$ Å, $b = 3.04$ Å, $c = 5.80$ Å, and $\beta = 103.7°$ [126]. Depending on the local arrangement of Ga-O bonds, there are two distinct kinds of Ga sites and three distinct

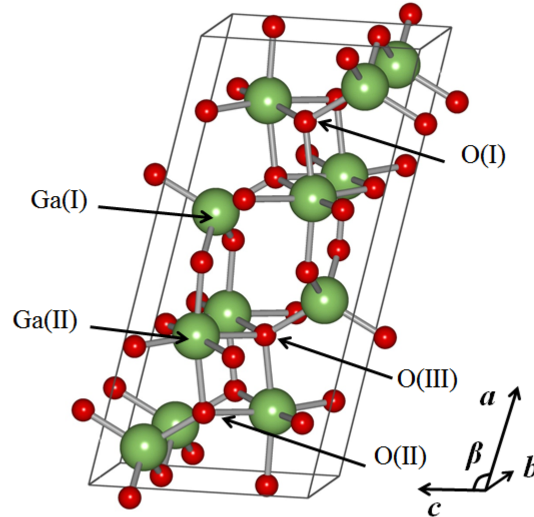

Figure 8.1: 20 atom unit cell of β-Ga_2O_3 (twice the primitive cell) showing two distinct gallium sites (big, green spheres) and three distinct oxygen sites (small, red spheres).

kinds of O sites. The tetrahedral Ga(I) site and octahedral Ga(II) site have four and six oxygen nearest neighbors respectively. The O(I) site is threefold coordinated with 1 Ga(I) and 2 Ga(II) nearest neighbors. The O(II) site is also threefold coordinated but has 2 Ga(I) and 1 Ga(II) nearest neighbors. The O(III) site is fourfold coordinated with 1 Ga(I) and 3 Ga(II) nearest neighbors. Figure 8.1 illustrates the crystal structure of β-Ga_2O_3 in its 20-atom conventional unit cell, which is twice the size of the base centered monoclinic primitive cell. Band structure calculations indicate that this material has a *direct* band gap, a small and isotropic electron effective mass, and a much larger hole effective mass resulting from the almost flat valence bands [127, 128, 129].

8.3 Numerical details

The total energies of various defect configurations in this chapter are obtained through spin-polarized DFT calculations using VASP [13, 14, 15, 16] with the Perdew-Wang 1991 (PW91) generalized gradient approximation (GGA) functional [39]. The ultra-

soft Vanderbilt-type pseudopotentials [40, 41] are used, including the $10d$ semicore electrons of Ga. A 400 eV energy cutoff in the plane-wave expansions are used. Geometry relaxations are carried out using the conjugate gradient method while the lattice dimensions are kept fixed at the theoretical equilibrium values of β-Ga_2O_3 predicted by DFT, which is within 1% of experimental data.

For intrinsic point defect calculations in 8.4, a 160-atom supercell with roughly equal dimensions ($1a \times 4b \times 2c \sim 12 \times 12 \times 12$ Å^3) and a $2 \times 2 \times 2$ Monkhorst-Pack *[18]* k-point mesh are used. For transition metal defect calculations in 8.5, a 40-atom supercell with roughly equal dimensions ($1a \times 2b \times 1c \sim 12 \times 6 \times 6$ Å^3) and a $2 \times 4 \times 4$ Monkhorst-Pack [18] k-point mesh is used. The 40-atom supercell is enough to avoid any spurious interactions of metal dopant with its neighboring images. When calculating static band structures, the end points of the k-point sampling paths are expressed in terms of the reciprocal lattice vectors $\mathbf{a}^*$, $\mathbf{b}^*$ and $\mathbf{c}^*$. The path through the Brillioun zone is a line parallel to $\mathbf{c}^*$ from $\mathbf{c}^*/2$ to Γ followed by a rectangle starting with a line parallel to $\mathbf{b}^*$ from Γ to $\mathbf{b}^*/2$ and ending with a line parallel to $\mathbf{a}^*$ from $\mathbf{a}^*/2$ to Γ.

8.4 Intrinsic point defects in β-Ga_2O_3

High purity β-Ga_2O_3 has unintentional n-type conductivity. This is commonly attributed to the presence of oxygen vacancies [130]. However this model has been challenged by recent experimental and theoretical investigations [127, 131]. Using hybrid functionals, Varley *et al* have performed DFT calculations on the role of oxygen vacancies in the electrical properties of β-Ga_2O_3 and find that oxygen vacancies are deep donors, and thus cannot explain the unintentional n-type conductivity. We have performed DFT calculations with GGA functionals on the intrinsic vacancy defects, both oxygen and gallium vacancies. The results are in agreement with those of Varley *et al.*

The bulk formation energy of a defect is an important quantity in determining its

concentration in a material under equilibrium conditions. The formation energy of an intrinsic defect X (i.e. Ga interstitial, O vacancy) in charge state q is defined as [132]

$$E^f[\mathrm{X}^q] = E_{tot}[\mathrm{X}^q] - E_{tot}[\mathrm{Ga_2O_3, bulk}] - n_{\mathrm{O}}\mu_{\mathrm{O}} - n_{\mathrm{Ga}}\mu_{\mathrm{Ga}} + q[E_F + E_V + \Delta V] \quad (8.1)$$

where $E_{tot}[\mathrm{Ga_2O_3, bulk}]$ and $E_{tot}[\mathrm{X}^q]$ are the total energies associated with the perfect $\mathrm{Ga_2O_3}$ supercell and the supercell including the defect X^q respectively. The rest of the terms account for the difference in the number of atoms and electrons when the energies of the aforementioned supercells are compared. n is the number of atoms that is added to ($n > 0$) or removed from ($n < 0$) the perfect supercell to form the defected supercell. For instance, for an oxygen vacancy structure, $n_{\mathrm{O}} = -1$, $n_{\mathrm{Ga}} = 0$.

μ is the chemical potential, which represents the energy of the reservoirs (reference energy) of the atoms being exchanged. Chemical potential depends on the experimental conditions, which can be either Ga-rich, O-rich, or in between. Under the extreme Ga-rich conditions, the μ_{Ga} reaches its upper bound, which is the total energy per atom of the Ga metal. Under the extreme O-rich conditions, μ_{O} reaches its upper bound, which is the total energy per atom of the $\mathrm{O_2}$ molecule. μ_{Ga} and μ_{O} are related by the following relation,

$$2\mu_{\mathrm{Ga}} + 3\mu_{\mathrm{O}} = E_{\mathrm{tot}}^{\mathrm{f.u.}}[\mathrm{Ga_2O_3}] \quad (8.2)$$

where $E_{\mathrm{tot}}^{\mathrm{f.u.}}[\mathrm{Ga_2O_3}]$ is the total energy of one formula unit of bulk $\mathrm{Ga_2O_3}$. This relation and the higher bounds place the lower bounds on both μ_{Ga} and μ_{O}, so that we have

$$\frac{E_{\mathrm{tot}}[\mathrm{Ga_2O_3}] - 3\mu_{\mathrm{O[O_2]}}}{2} \leq \mu_{\mathrm{Ga}} \leq \mu_{\mathrm{Ga[bulk]}} \quad (8.3)$$

$$\frac{E_{\mathrm{tot}}[\mathrm{Ga_2O_3}] - 2\mu_{\mathrm{Ga[bulk]}}}{3} \leq \mu_{\mathrm{O}} \leq \mu_{\mathrm{O[O_2]}} \quad (8.4)$$

Table 8.1: Gallium and oxygen chemical potentials under extreme Ga-rich and O-rich conditions.

Condition	μ_{Ga} (eV)	μ_{O} (eV)
extreme Ga-rich	-2.94	-8.12
extreme O-rich	-7.76	-4.91

Table 8.1 gives the upper and lower bounds of Ga and O chemical potentials derived from total energy calculations of Ga metal[1], oxygen molecule and bulk Ga_2O_3.

E_F is the Fermi level, referenced to the valence band maximum (VBM) of the bulk structure; and E_V is the energy of the VBM. The correction term ΔV is added to align the reference potential in the defect supercell with that of the bulk. The reason for adding this term is as follows. The E_V term in Eq. 8.1 is supposed to be extracted from calculations of the defected supercell. However, the defect may introduce additional bands near the VBM and thus make the evaluation of E_V difficult. Due to the fact that the defect introduces a constant shift (ΔV) to the electrostatic potential of the supercell, an alternative approach is to find the value of E_V of the bulk, and then add this shift term to obtain the "aligned" E_V value.

There are many ways to find the ΔV term for a given defect. most obvious choice is the VBM. One way is to compare the location on the energy scale of Ga pseudo-core d-states of the defect supercell with that of the bulk. In this study, we first calculate the electrostatic potential at three points far away from the defect location. This is done for both the defect and the bulk supercells. Then, ΔV is extracted by averaging the potential difference over all sample points.

For the charged supercell calculations, the usual correction methods are not used here as they lead to overestimation of image interaction energies [132]. Thus we do not include the correction terms in this study.

---

[1]Monoclinic α-Ga, for visualization and coordinates refer to `http://cst-www.nrl.navy.mil/lattice/struk/a11.html`.

The transition level $\epsilon(q/q')$ is defined as the Fermi level where the formation energies of the two charge states are equal, i.e. $E^f[\mathrm{X}^q] = E^f[\mathrm{X}^{q'}]$. If the formation energy of all charge states of a given defect X is plotted against the Fermi level, the transition level $\epsilon(q/q')$ simply corresponds to the intersection of the two lines representing X^q and $\mathrm{X}^{q'}$. The difference between the transition level and band edge for a given defect is called its activation energy.

We have calculated the formation energies of various distinct vacancy structures and extracted the associated electric levels. Band structure calculations predict the band-gap of β-Ga_2O_3 to be 2.13 eV, which is much smaller than the experimental band-gap of 4.9 eV. Underestimating the band-gap is an intrinsic band-gap problem of DFT.

Figure 8.2 shows the computed formation energies as a function of Fermi level for the three distinct oxygen vacancy ($\mathrm{V}_{\mathrm{O(I)}}$, $\mathrm{V}_{\mathrm{O(II)}}$, $\mathrm{V}_{\mathrm{O(III)}}$) and two distinct gallium vacancy ($\mathrm{Ga}_{\mathrm{O(I)}}$, $\mathrm{Ga}_{\mathrm{O(II)}}$) structures under Ga-rich and O-rich conditions. For all three oxygen vacancy structures, the $+1$ charge state is always unfavorable. This implies that oxygen vacancies are either doubly-ionized (e.g. in p-type material where $E_F = E_V$) or neutral (e.g. in n-type material where $E_F = E_C$) depending on the Fermi level location. In n-type β-Ga_2O_3 ,$\mathrm{V}^0_{\mathrm{O(II)}}$ has the lowest formation energy of 0.6 eV compared to the other two neutral vacancy configurations and is thus the favorable configuration. In p-type material, $\mathrm{V}^{2+}_{\mathrm{O(I)}}$ and $\mathrm{V}^{2+}_{\mathrm{O(III)}}$ are the favorable configuration with almost identical formation energies, as seen from Figure 8.2 in which blue and red lines stay close to each other for small E_F values. The $\epsilon(2+/0)$ electric level of $\mathrm{V}^0_{\mathrm{O(II)}}$ is rather deep, at $E_V + 1.10$ eV. Although its formation energy is 0.72 eV higher than $\mathrm{V}_{\mathrm{O(II)}}$ in n-type material, $\mathrm{V}_{\mathrm{O(III)}}$ has the highest $\epsilon(2+/0)$ level of $E_V + 1.81$ eV, 0.32 eV below the uncorrected E_C. Thus, the smallest activation energy for oxygen vacancies in β-Ga_2O_3 is 0.32 eV for the uncorrected DFT band gap of 2.13 eV.

For the two types of Gallium vacancies, both can take the form of 4 charge states as the Fermi level varies within the band gap: neutral, singly negative, doubly negative,

and triply negative. The tetrahedral $V^0_{Ga(I)}$ is 0.34 eV more stable than the octahedral $V^0_{Ga(II)}$ in p-type material, while the octahedral $V^{3-}_{Ga(II)}$ is 0.5 eV more stable than the tetrahedral $V^{3-}_{Ga(I)}$ in n-type material. The $\epsilon(3-/2-)$ level for $V_{Ga(I)}$ and $V_{Ga(II)}$ are $E_C - 0.60$ eV and $E_C - 0.86$ eV. Thus the smallest activation energy for gallium vacancies is 0.60 eV.

The formation energies of Ga vacancies are much higher than O vacancies for Ga-rich conditions. Under O-rich conditions, the formation energies of Ga vacancies become comparable to O vacancies when Fermi level is around mid gap. As Fermi level moves toward the conduction band minimum (the material becomes more and more n-type), the formation energies of the Ga vacancies fall quickly, becoming >2 eV smaller than O vacancies in strongly n-type materials.

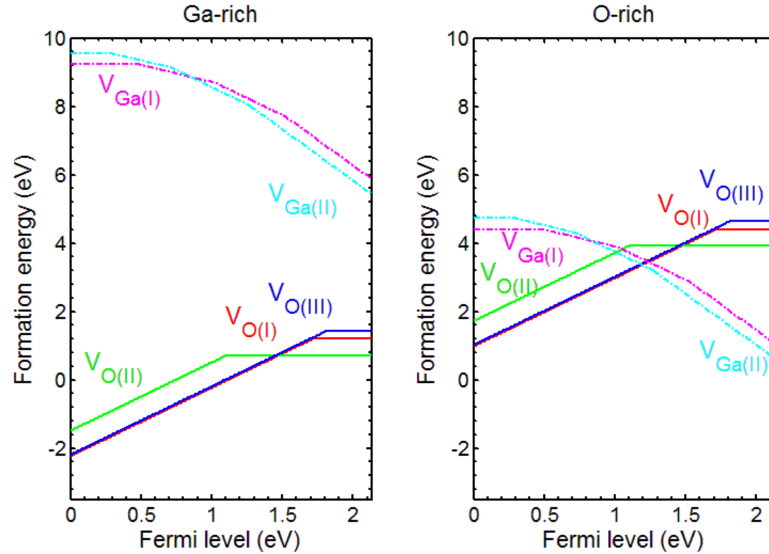

Figure 8.2: Formation energy of vacancy defects Ga-rich and O-rich conditions as a function of Fermi level. The slope of a given line segment corresponds to the charge state.

In this study, the smallest activation energy of oxygen donors is predicted to be at least 0.32 eV. Since DFT severely underestimates the band gap, the actual

activation energy can be much greater than 0.32 eV. This is much larger than $k_B T$ ($\sim$0.03 eV) at room temperature. Thus, we can conclude that oxygen vacancies can not give substantial contributions to the n-type conduction of β-Ga_2O_3. The results for oxygen vacancies are consistent with recent DFT calculations by Varley *et al.* [127] using hybrid exchange correlation functionals. In their study, they use hybrid functionals and fitting the mixing parameters to produce the correct band gap of 4.9 eV, then calculates the smallest activation energy to be 1.2 eV. Both studies lead to the same conclusion denying the contribution of oxygen vacancies in n-type conduction of β-Ga_2O_3.

Even though oxygen vacancies don't play a role in bulk conductivity, it may affect conductivity at the surface. It is observed from hard x-ray photoemission spectroscopy (HXPS) measurements that there exist an upward band bending of at least 0.5 eV for high purity β-Ga_2O_3 [114]. This band bending can change the equilibrium balance between neutral and doubly positive oxygen vacancies, effectively causing neutral species to donate electrons and become doubly positive at the surface. This can potentially lead to β-Ga_2O_3 gas sensing properties at the β-Ga_2O_3 surface [114].

8.5 Transition metal impurities in β-Ga_2O_3

With transition metal (TM) doping, oxides exhibits many interesting electronic, optical, and magnetic properties. For example, TM-doping at the percent level can lead to diluted magnetic semiconductors (DMS) [124, 125], which show great potential for future spintronics devices. Ga_2O_3 has been shown to exhibit room temperature ferromagnetism when doped with Mn to 7-8 % [133, 134]. Electron spin resonance (ESR) and electron paramagnetic resonance (EPR) studies have suggested that Mn 2+ ions occupy the octahedrally-coordinated Ga 3+ lattice site [135, 136]. Previous DFT calculations show that Mn in β-Ga_2O_3 is more stable in octahedrally-coordinated Ga sites [137], but the accuracy of the result is questionable due to the very small periodic cell (20 atom) used, which may lead to spurious Mn-Mn interactions. Apart

from this, there are still many unknowns regarding the properties of transition metal dopants in β-Ga_2O_3, such as the occupation site of dopant atoms in the lattice, their valence state, and influence to the conductivity. In this section, we study the atomic and electronic structure of bulk single crystals of Mn-doped and Cr-doped β-Ga_2O_3 using the density functional theory. Calculations indicate that for both dopants prefer octahedral site occupation. Cr mainly shows 3+ valence, while Mn shows a mixed 2+ and 3+ valence. The DFT prediction is consistent with experimental measurements.

We have calculated the formation energy of the dopants on tetrahedral and octahedral gallium sites and found that the octahedral site is energetically favorable for both Cr and Mn. The tetrahedral site is 1.57 eV higher in energy for Cr, and 0.63 eV higher for Mn. This results qualitatively agrees with the XANES data and is also consistent with ESR measurements [115, 135, 136]. .

We have also calculated the electronic structure of the most favorable dopant configurations, namely octahedral Cr and Mn as shown in Figure 8.4. Calculations are performed for neutral cells, which corresponds to 3+ valence for Cr and Mn. In order to understand the changes in electronic structure brought about by the dopants, the electronic structure of pure β-Ga_2O_3 was also computed and shown in Figure 8.3. Comparing the band structures, we found that both dopants introduce new energy levels within the β-Ga_2O_3 band gap as well as in the valence and conduction bands. Octahedral Cr introduces three bands with energy values between 1.0 eV and 1.5 eV, all of which are filled with electrons (red/dark bands in 8.4 (a)). Octahedral Mn introduces two new bands with energy values between 1.5 eV and 2.0 eV. One of these new states is occupied (the red/dark band in 8.4 (b)), and the other unoccupied (the green/light band in 8.4 (b)). These values are with respect to the DFT band-gap of 2.13 eV, however these levels are still interpreted as deep levels for the real band-gap of 4.9 eV, as we assume that they remain at the similar relative location to the valence band maximum.

Pure β-Ga_2O_3 exhibits n-type conductivity, with Fermi level located close to the

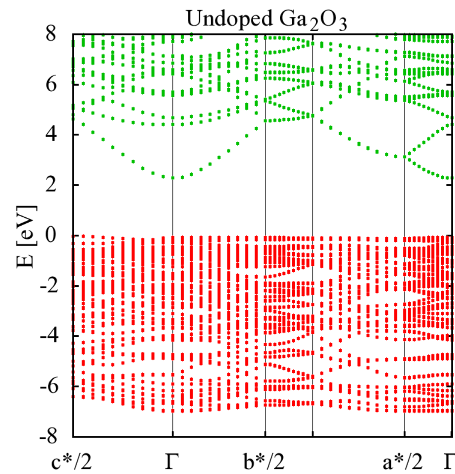

Figure 8.3: DFT:GGA band structure plot for relaxed, neutral, 40-atom cell of undefected β-Ga_2O_3. Filled states are shown in green dots (lighter) and unfilled states in red dots (darker).

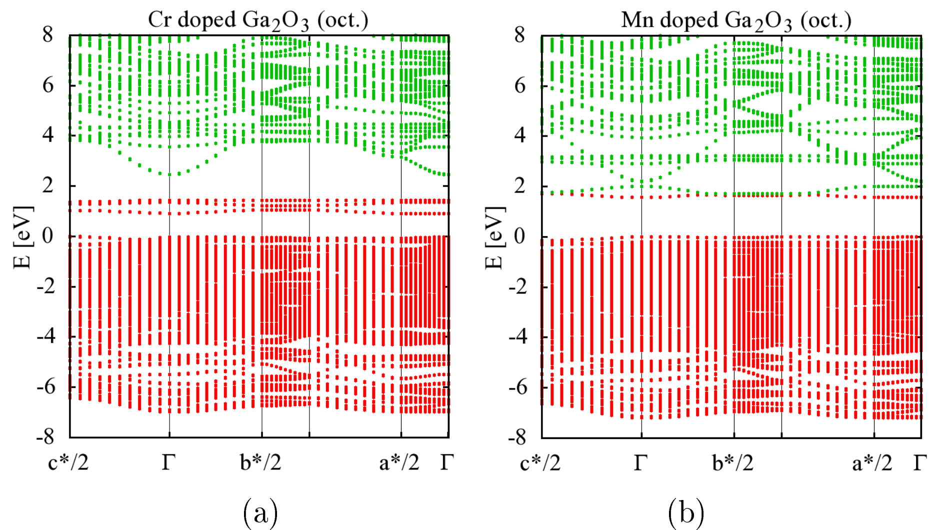

Figure 8.4: DFT:GGA band structure plot for relaxed, neutral, 40-atom cell of β-Ga_2O_3 with one Cr replacing an octahedral Ga . Filled states are shown in green dots (lighter) and unfilled states in red dots (darker).

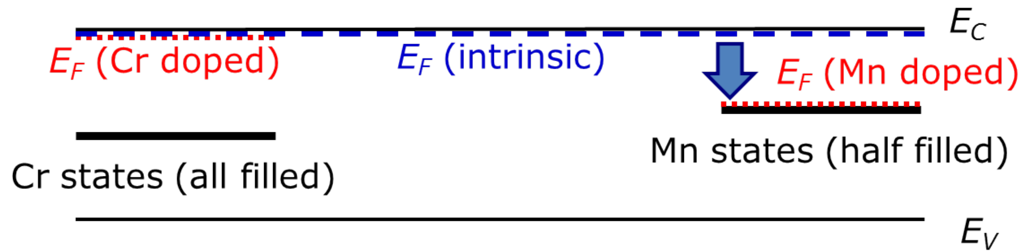

Figure 8.5: Energy band diagram of β-Ga_2O_3 under Cr or Mn doping.

conduction band minimum. Since octahedral Cr has three filled mid-gap defect states far from the Fermi level, they are unlikely to affect the electronic properties of the material. This implies that Cr will remain its 3+ valence as Ga in the material, and the Cr doped β-Ga_2O_3 still remains its n-type conductivity. This is consistent with experimental findings [115]. For octahedral Mn, since it introduces half filled states in the mid-gap, it can accept electrons from the Fermi level at the conduction band minimum. When this happens, the Mn changes from 3+ valence to 2+. In other words, Mn behaves like an acceptor, compensating the n-type intrinsic conduction. If Mn is the dominant doping species and it's concentration is higher than whatever the source of intrinsic conduction, the Fermi level will be effectively pinned at the Mn 2+/3+ level, at $E_V + 1.8$ eV predicted by DFT. In this way, Mn should exhibit both 2+ and 3+ valence. The above analysis also implies that Mn doped β-Ga_2O_3 should have a reduced conductivity compared to the pure material, which is confirmed by resistivity measurements [115]. Figure 8.5 illustrates the Fermi level positions for Cr and Mn doped β-Ga_2O_3.

Chapter 9

SUMMARY AND FUTURE DIRECTIONS

In this thesis, we use multi-scale modeling approaches to investigate generation and diffusion of defects in semiconductor materials, with a wide range of technology applications in semiconductor electronics, crystalline silicon photovoltaics, and future electronics devices based on wide-band-gap semiconductor materials. In this chapter, we summarize the work presented in this dissertation, and conclude with suggestions for future work.

9.1 Summary

In the following sections, our primary achievements are summarized by topic.

9.1.1 KLMC simulations of self-diffusion and interdiffusion in Si

1. The correlation factors of various hopping mechanisms on different networks in the diamond lattice have been calculated. The correlation factor of Si interstitial-mediated self-diffusion is found to be temperature dependent, with predicted values of 0.6 at 1000-1100 °C in agreement with experimental results.

2. The stress and alloy effects of Ge on the interdiffusion process in SiGe have been separated. The extracted coefficient quantifying both effects qualitatively agrees with experiments.

9.1.2 DFT calculations of life-time limiting defects in Si

1. The stability and electronic properties of seven metal impurities (Cu, Cr, Fe, Ni, W, Mo, Ti) in Si have been investigated. The DFT binding energies give predictions on the gettering behavior of metals in the presence of phosphorus implants and agrees qualitatively with experimental observations.

9.1.3 Numerical models for coupled PSG growth and P diffusion in $POCl_3$ diffusion process

1. Analyzing SIMS profiles, we find that a PSG layer with composition nearly independent of process conditions forms during predeposition. There is also a thin layer of SiO_2 sandwiched between the PSG and Si, and a strong accumulation of P at the SiO_2-Si interface is also observed.

2. A growth model for $POCl_3$ deposition process that includes oxygen dependence and dose saturation is developed. The predicted kinetics of PSG thickness and dose of diffused P into Si are in agreement with experimental data. We further couple this model to to the process models in Si and calculated the resulting emitter profiles, which agree well with experiments. This set of coupled models provides full modeling of the $POCl_3$ deposition process for emitters formation in crystalline Si solar cell structures.

9.1.4 DFT calculations of intrinsic and metal impurities in β-Ga_2O_3

1. We have carried out DFT calculations on the intrinsic vacancy defects in β-Ga_2O_3 and concluded that oxygen can't contribute to its n-type intrinsic conductivity under normal conditions.

2. We also calculated the properties of transition-metal (Cr, Mn) dopants inβ-Ga_2O_3 and gave predictions on the valance state and conductivity which agree

well with experimental observations.

9.2 Suggestions for future work

9.2.1 Kinetic lattice Monte Carlo process simulations

Currently the KLMC code is limited to simulations of point defect mediated diffusion processes. Its functionality can be further extended to include extended defects such as {311} defects and dislocation loops. However, it is challenging to simulate the full atomic details of the kinetics of these defects efficiently. One way of realizing this is to use a coarse-graining scheme. For example, a {311} defect has a capture cross section, and once an interstitial is within the cross section, it will be captured, and automatically attached to the end of the {311} defect. This process happens at a large time-scale (10^{-3} s) and the detailed atomic process of capturing and migrating to the end of the defect can be ignored for the sake of efficiency.

9.2.2 Phosphorus deactivation and gettering of metals

In Chapter 6 we have performed DFT calculations on various metal complexes. Based on this, continuum models can be developed to quantify the phosphorus diffusion gettering of metals to predict the metal distribution in silicon solar cells after solid state diffusion of phosphorus. The models can be further coupled with moment based models for extended defects (i.e. {311} defects and dislocation loops) formation to predict the gettering behavior of metals with implanted phosphorus profiles.

9.2.3 $POCl_3$ emitter diffusion

In Chapter 7 we have built models that give reasonable predictions of diffused emitter profiles and calibrated parameters against process conditions with varying predeposition time and $POCl_3$ flow. Further calibration of the parameters can be done by analyzing more samples with different $POCl_3$ doping conditions . Another set of

samples fabricated by Applied Materials will be characterized soon and this allows calibration of parameters for different temperatures and oxygen flow rates. Besides, even if the simulations were essentially performed in 1D domain, it can be easily extended to 2D or 3D for the simulation of pyramid structures, which are typical in cells with textured surfaces for better light absorption. Preliminary simulations using an a simpler version of our model have proven the robustness of the model in 3D simulations [138]. Special care must be taken in the generation of meshes in 3D simulations, which should give results with acceptable accuracy with reasonable CPU hours and memory usage. Lastly, these models can be further coupled to device simulations to predict the effect of process conditions on cell performances.

9.2.4 Impurities in β-Ga_2O_3

In addition to investigating vacancy defects in β-Ga_2O_3 in Chapter 8, it is natural to extend the approach to look at interstitial defects and anti-site defects. Formation energy analysis can give stability of various defects under different chemical conditions. Using NEB method, migration barriers can be found, which can shed light on the important transport mechanisms that contributes to the intrinsic n-type conductivity of the material.

9.3 Final conclusion

In this dissertation, we demonstrated how multiscale modeling approaches can be applied to simulate various properties and processes in semiconductor devices. With the combination of ab-initio, KLMC, and continuum approaches etc., TCAD will continue exhibit great potential in the integrated circuit as well as photovoltaics industries.

Appendix A
KLMC SIMULATOR LAMOCA

We have developed a C++ based simulator LAMOCA, which is capable of simulating the diffusion processes in silicon and silicon germanium involving impurities and point defects. Here we give a brief introduction of this simulator.

A.1 Simulation Domain

The unit cell of the simulation domain is the crystalline silicon cubic structure. A notable feature of this simulator is the incorporation of the augmented lattice that includes not only substitutional lattice sites that silicon atoms normally occupy, but also high symmetry interstitial sites (i.e. tetrahedral, hexagonal, bond-centered sites). Illustration of the augmented lattice sites in a conventional unit cell of the diamond lattice structure is shown in Fig. A.1. Table A.1 lists the number of these sites per unit cell. The augmented lattice domain allows capturing the various transition pathways involved in the interstitial-mediated diffusion processes. The simulation domain includes a three-dimensional array of such cubic cells with periodic boundary conditions on all dimensions.

Table A.1: The augmented lattice sites and their numbers per unit cell.

Sites	Numbers
Substitutional (S)	8
Tetrahedral (T)	8
Hexagonal (H)	16
Bond-centered (B)	16

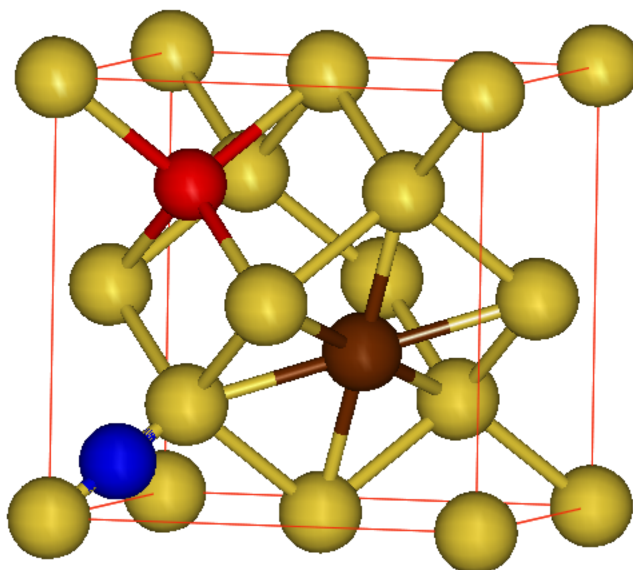

Figure A.1: Illustration of the augmented lattice sites in the silicon conventional unit cell. A substitutional site (light/yellow) is simply the silicon lattice site. A tetrahedral site (dark/red, upper left) is at the center of a tetrahedron formed by four substitutional sites. A hexagonal site (dark/brown, right) is at the center of a hexagonal ring formed by six substitutional sites. A bond-centered site (dark/blue, lower left) is at the center of a Si-Si bond. Reduced lattice coordinates for typical substitutional, tetrahedral, hexagonal, and bond-centered sites are (0, 0, 0), (1/4, 1/4, 3/4), (5/8, 3/8, 3/8), and (1/8, 1/8, 1/8), respectively.

A.2 Numerical Details

In its current version, LAMOCA is capable of simulating diffusion processes involving major impurities in silicon. Each defect species is characterized by three properties: constituent atom, occupying sites, and orientation. Some definitions are below:

- Simple defect: A defect that is composed only one constituent atom, such as a phosphorus, a vacancy etc.

- Complex defect: A defect that is composed two atoms. It is also called an interstitialcy.

- Intrinsic defect: A defect that is composed of only silicon and vacancy, e.g. as a vacancy, a silicon interstitial on a hexagonal site.

- Extrinsic defect: A defect that is composed of impurity atoms, e.g. a carbon silicon interstitialcy on substitutional sites.

The atom species included now are listed Table A.2. Complex defects may include two of the atom species. For example a silicon-silicon interstitialcy contains two silicon atoms.

Table A.2: The augmented lattice sites and their numbers per unit cell.

Atom species	Symbol
Phosphorus	P
Arsenic	As
Boron	B
Silicon	Si
Germanium	Ge
Carbon	C
Vacancy	V

During the simulation, the coordinates of point defects and impurity atoms are tracked. The diffusivity of a given species is calculated as

$$D = \frac{\langle \Delta \mathbf{r}^2 \rangle}{6\Delta t} \tag{A.1}$$

where $\langle \Delta \mathbf{r}^2 \rangle$ is the average squared displacement of the species and Δt is the corresponding time period.

Updating the rate catalog is the most time-consuming operation of in the KLMC simulations. Therefore, the entries should be easy to calculate from a given system configuration The migration barriers generally varies with surrounding conditions due to presence of other defects (extra binding energy) and presence of strain (extra strain

energy). In our KLMC code, only an unbiased energy barrier E_m^0 is stored for each transition. The modified barrier due to change of formation energies of initial and final states are evaluated by

$$E_m = E_m^0 + \frac{1}{2}\left(\Delta E_{fi} - \Delta E_{in}\right) \tag{A.2}$$

Transition barriers calculated in this way still obey the detailed balance condition. Figure A.2 illustrates the how to determine the barrier change.

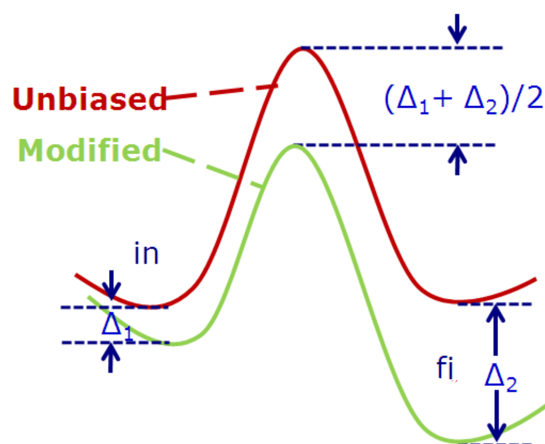

Figure A.2: Change of migration barrier due to change of formation energies of initial and final states.

Appendix B

5-STREAM PAIR-DIFFUSION MODEL

Here we go through the derivation of the 5-stream diffusion model. We use a donor species P as an example.

B.1 Model species

The 5-stream model considers 5 species as solution variables in the partial differential equation set. P_S is substitutional electrically active phosphorus, PI and PV are the associated defect pairs, which are the diffusing species. The concentration of these species is a sum of all charged states.

The reactions are

$$P_S + I \Longleftrightarrow PI \tag{B.1}$$

$$P_S + V \Longleftrightarrow PV \tag{B.2}$$

$$PI + V \Longleftrightarrow P_S \tag{B.3}$$

$$PV + I \Longleftrightarrow P_S \tag{B.4}$$

Table B.1: Species in the 5-stream model.

Name	Definition	Reference Charge State
P_S	unpaired substitutional atom	P_S^+
I	unpaired interstitial	I^0
V	unpaired vacancy	V^0
PI	acceptor-interstitial pair	$(PI)^+$
PV	acceptor-vacancy pair	$(PV)^+$

$$\mathrm{PI} + \mathrm{PV} \Longleftrightarrow 2\mathrm{P_S} \tag{B.5}$$

where the diffusing species are PI, PV, I, and V. We can write out the model equations as:

$$\frac{\partial C_\mathrm{P}}{\partial t} = -R_\mathrm{P/I} - R_\mathrm{P/V} + R_\mathrm{PI/V} + R_\mathrm{PV/I} + 2R_\mathrm{PI/PV} \tag{B.6}$$

$$\frac{\partial C_\mathrm{PI}}{\partial t} = -\nabla \cdot J_\mathrm{PI} + R_\mathrm{P/I} - R_\mathrm{PI/V} - R_\mathrm{PI/PV} \tag{B.7}$$

$$\frac{\partial C_\mathrm{PV}}{\partial t} = -\nabla \cdot J_\mathrm{PV} + R_\mathrm{P/V} - R_\mathrm{PV/I} - R_\mathrm{PI/PV} \tag{B.8}$$

$$\frac{\partial C_\mathrm{I}}{\partial t} = -\nabla \cdot J_\mathrm{I} - R_\mathrm{P/I} - R_\mathrm{PV/I} - R_\mathrm{I/V} \tag{B.9}$$

$$\frac{\partial C_\mathrm{V}}{\partial t} = -\nabla \cdot J_\mathrm{V} - R_\mathrm{P/V} - R_\mathrm{PI/V} - R_\mathrm{I/V} \tag{B.10}$$

In the following, we will derive the expression of each of the reaction term and diffusion flux terms.

B.2 Assumptions

There are several assumptions used in the model.

1. All ionization reactions are near equilibrium ('int' = intrinsic), which gives

$$C_{\mathrm{X}^i} = K_{\mathrm{X}^i} C_{\mathrm{X}^0} \left(\frac{n_i}{n}\right)^i = \left(C_{\mathrm{X}^i}\right)_\mathrm{int} \left(\frac{n_i}{n}\right)^i \tag{B.11}$$

$$C_{(\mathrm{PX})^i} = K_{(\mathrm{PX})^i} C_{(\mathrm{PX})^+} \left(\frac{n_i}{n}\right)^{i-1} = \left(C_{(\mathrm{PX})^i}\right)_\mathrm{int} \left(\frac{n_i}{n}\right)^{i-1} \tag{B.12}$$

2. Boltzmann statistics.

$$E = -\nabla V = -\frac{kT}{q} \nabla \ln\left(\frac{n}{n_i}\right) \tag{B.13}$$

3. Einstein equation

$$\frac{d}{\mu} = \frac{kT}{q} \tag{B.14}$$

4. All charge states have the same diffusivity coefficient.

$$d_{\mathrm{X}^i} = d_{\mathrm{X}},\ d_{(\mathrm{PX})^i} = d_{(\mathrm{PX})} \tag{B.15}$$

5. All reactions are diffusion limited (i.e. no barriers for the kinetic factor) except for the I/V recombination.

6. Usually the diffusivities of the pairs are assumed to be the same as the corresponding point defects

$$d_{\mathrm{PX}} = d_{\mathrm{X}} \tag{B.16}$$

B.3 Definition of some terms

B.3.1 Carrier concentration

The carrier concentration is determined by charge neutrality condition ($C_{\mathrm{P}} + p = n$) and the mass reaction law ($np = n_i^2$). Thus we have,

$$\frac{n}{n_i} = \frac{C_{\mathrm{P}}}{2n_i} + \sqrt{\left(\frac{C_{\mathrm{P}}}{2n_i}\right)^2 + 1} \tag{B.17}$$

B.3.2 Point defect property χ_I and χ_V

Here we define

$$\chi_{\mathrm{X}} = \sum_i K_{\mathrm{X}^i} \left(\frac{n_i}{n}\right)^i \tag{B.18}$$

So that $C_{\mathrm{X}} = \chi_{\mathrm{X}} C_{\mathrm{X}^0}$. The parameters K_{X^i} are closely related to the states of the defects in the band gap and can in principle be determined from ab initio calculations.

B.3.3 Dopant-defect pair property π_I and π_V

Here we define

$$\pi_{\mathrm{X}} = \sum_i K_{\mathrm{P}^+/\mathrm{X}^i} K_{\mathrm{X}^i} \left(\frac{n_i}{n}\right)^i \tag{B.19}$$

where $K_{\mathrm{P}^+/\mathrm{X}^i}$ is the equilibrium constant for reaction between P^+ and X^i. Thus in equilibrium conditions

$$C_{\mathrm{PX}} = \pi_{\mathrm{X}} C_{\mathrm{X}^0} C_{\mathrm{P}} \tag{B.20}$$

A more general equation gives

$$C_{\mathrm{PX}} = \frac{\pi_{\mathrm{X}}}{K_{\mathrm{P}^+/\mathrm{X}^0}} \pi_X C_{(\mathrm{PX})^+} \tag{B.21}$$

It is actually more convenient to not specifying the $K_{\mathrm{P}^+/\mathrm{X}^i}$ factors directly; rather, we use experimental observed values and some assumptions. As phosphorus diffuses only through pairing with point defects of various charge states, we can obtain the total (experimentally observed) diffusivity by summing the contribution of individual charge states:

$$D_{\mathrm{P}} = D_{\mathrm{P}}^{\mathrm{I}} + D_{\mathrm{P}}^{\mathrm{V}} = \sum_i D_{\mathrm{P}}^{\mathrm{I}^i} + \sum_i D_{\mathrm{P}}^{\mathrm{V}^i} \tag{B.22}$$

The individual diffusivities can be decomposed to an intrinsic term and another term that depends on Fermi level (n/n_i).

$$D_{\mathrm{P}}^{\mathrm{X}^i} = \left(D_{\mathrm{P}}^{\mathrm{X}^i}\right)_{\mathrm{int}} \left(\frac{n_i}{n}\right)^i \tag{B.23}$$

The convenience of this expression is two-folded: first, it provides a direct link to the experiments where these intrinsic diffusivity values are measured; second, we can actually represent π_{X} by $\left(D_{\mathrm{P}}^{\mathrm{X}^i}\right)_{\mathrm{int}}$ instead of specifying the factors. From assumption (d), we can see easily from the above two equations that $D_{\mathrm{P}}^{\mathrm{X}^i}$ varies with $C_{(\mathrm{PX})^{i+1}}$, thus,

$$\pi_{\mathrm{X}} = K_{\mathrm{P}^+/\mathrm{X}^0} \frac{D_{\mathrm{P}}^{\mathrm{X}}}{D_{\mathrm{P}}^{\mathrm{X}^0}} \tag{B.24}$$

The $K_{\mathrm{P}^+/\mathrm{X}^i}$ factors are not needed expect for $K_{\mathrm{P}^+/\mathrm{X}^0}$, despite the fact that the final result is not sensitive to its value.

In the code, the intrinsic diffusivities $\left(D_{\mathrm{P}}^{\mathrm{X}^i}\right)_{\mathrm{int}}$ are provided, they are used to

calculate the total diffusivity with the Fermi level dependence $(n_i/n)^i$ as the weighting factor. Then the quantity π_{X} is calculated with Eq. (28).

B.4 Determination of flux terms

B.4.1 Flux of point defects

For each charge state of X^i

$$J_{\mathrm{X}^i} = -d_{\mathrm{X}^i} \nabla C_{\mathrm{X}^i} + i\mu_{\mathrm{X}^i} E C_{\mathrm{X}^i} \tag{B.25}$$

From Assumption (a), we rewrite the gradient term in terms of C_{X^0}, and canceling terms using assumptions (b,c), we get

$$J_{\mathrm{X}} = -d_{\mathrm{X}} \chi_{\mathrm{X}} \nabla C_{\mathrm{X}^0} \tag{B.26}$$

This is the same result as the case of pure diffusion. The extra drift term is canceled by the C_{X^0} dependence on n in the diffusion term.

B.4.2 Flux of impurity-defect pairs

For each charge state of $(\mathrm{PX})^i$, we can write a similar equation. Summing up all the charge state contributions, we have

$$J_{(\mathrm{PX})} = -\frac{D_{\mathrm{P}}^{\mathrm{X}}}{C_{\mathrm{X}^0}^*} \left[\nabla \left(\frac{C_{\mathrm{PX}}}{\pi_{\mathrm{X}}} \right) + \left(\frac{C_{\mathrm{PX}}}{\pi_{\mathrm{X}}} \right) \nabla \ln \left(\frac{n}{n_i} \right) \right] \tag{B.27}$$

For acceptors, the plot should be changed to minus sign.

B.5 Reaction rates

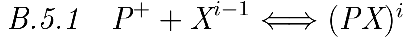

B.5.1 $P^{+} + X^{i-1} \Longleftrightarrow (PX)^{i}$

Reaction rate is

$$R_{\mathrm{P^+/X^{\mathit{i}-1}}} = 4\pi a d_{\mathrm{X^{\mathit{i}-1}}} \left[C_{\mathrm{P^+}} C_{\mathrm{X^{\mathit{i}-1}}} - \frac{C_{\mathrm{(PX)^{\mathit{i}}}}}{K_{\mathrm{P^+/X^{\mathit{i}-1}}}} \right] \tag{B.28}$$

Summing over all charge states, we have

$$R_{\mathrm{P/I}} = 4\pi a d_{\mathrm{I}} \left[C_{\mathrm{P}} C_{\mathrm{I}} - \frac{\chi_{\mathrm{I}}}{\pi_{\mathrm{I}}} \cdot C_{\mathrm{PI}} \right] \tag{B.29}$$

$$R_{\mathrm{P/V}} = 4\pi a d_{\mathrm{V}} \left[C_{\mathrm{P}} C_{\mathrm{V}} - \frac{\chi_{\mathrm{V}}}{\pi_{\mathrm{V}}} \cdot C_{\mathrm{PV}} \right] \tag{B.30}$$

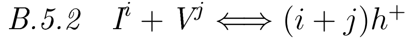

B.5.2 $I^{i} + V^{j} \Longleftrightarrow (i+j)h^{+}$

Summing over all charge reactions, we have

$$R_{\mathrm{I/V}} = 4\pi a \left(d_{\mathrm{I}} + d_{\mathrm{V}} \right) \left[C_{\mathrm{I}} C_{\mathrm{V}} - \chi_{\mathrm{I}} \chi_{\mathrm{V}} C^{*}_{\mathrm{I^0}} C^{*}_{\mathrm{V^0}} \right] \tag{B.31}$$

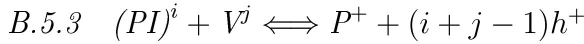

B.5.3 $(PI)^{i} + V^{j} \Longleftrightarrow P^{+} + (i+j-1)h^{+}$

Summing over all charge reactions, we have

$$R_{\mathrm{PI/V}} = 4\pi a \left(d_{\mathrm{PI}} + d_{\mathrm{V}} \right) \left[C_{\mathrm{PI}} C_{\mathrm{V}} - \pi_{\mathrm{I}} \chi_{\mathrm{V}} C^{*}_{\mathrm{I^0}} C^{*}_{\mathrm{V^0}} \cdot C_{\mathrm{P_S}} \right] \tag{B.32}$$

$$R_{\mathrm{PV/I}} = 4\pi a \left(d_{\mathrm{PV}} + d_{\mathrm{I}} \right) \left[C_{\mathrm{PV}} C_{\mathrm{I}} - \chi_{\mathrm{I}} \pi_{\mathrm{V}} C^{*}_{\mathrm{I^0}} C^{*}_{\mathrm{V^0}} \cdot C_{\mathrm{P_S}} \right] \tag{B.33}$$

$$R_{\mathrm{PI/PV}} = 4\pi a \left(d_{\mathrm{PI}} + d_{\mathrm{PV}} \right) \left[C_{\mathrm{PI}} C_{\mathrm{PV}} - \pi_{\mathrm{I}} \pi_{\mathrm{V}} C^{*}_{\mathrm{I^0}} C^{*}_{\mathrm{V^0}} \cdot C^{2}_{\mathrm{P_S}} \right] \tag{B.34}$$

BIBLIOGRAPHY

[1] R. M. Swanson, "A vision for crystalline silicon photovoltaics," *Progress in Photovoltaics*, vol. 14, no. 5, pp. 443–453, 2006.

[2] S. E. Thompson, M. Armstrong, C. Auth, S. Cea, R. Chau, G. Glass, T. Hoffman, J. Klaus, Z. Y. Ma, B. McIntyre, A. Murthy, B. Obradovic, L. Shifren, S. Sivakumar, S. Tyagi, T. Ghani, K. Mistry, M. Bohr, and Y. El-Mansy, "A logic nanotechnology featuring strained-silicon," *IEEE Electron Device Lett.*, vol. 25, no. 4, pp. 191–193, 2004.

[3] M. Gavelle, E. M. Bazizi, E. Scheid, P. F. Fazzini, F. Cristiano, C. Armand, W. Lerch, S. Paul, Y. Campidelli, and A. Halimaoui, "Detailed investigation of Ge-Si interdiffusion in the full range of $Si_{1-x}Ge_x (0 \leq x \leq 1)$ composition," *J. Appl. Phys.*, vol. 104, no. 11, p. 7, 2008.

[4] G. R. Xia, M. Canonico, and J. L. Hoyt, "Interdiffusion in strained Si/strained SiGe epitaxial heterostructures," *Semicond. Sci. Technol.*, vol. 22, no. 1, pp. S55–S58, 2007.

[5] S. T. Dunham, "A quantitative model for the coupled diffusion of phosphorus and point defects in silicon," *Journal of the Electrochemical Society.*, vol. 139, no. 9, p. 2628, 1992.

[6] Plasma Physics Research Center, "Secondary ion mass spectrometry theory tutorial." http://pprco.tripod.com/SIMS/Theory.htm (accessed July 18, 2012).

[7] C. Honsberg and S. Bowden, "PVCDROM." http://www.pveducation.org/pvcdrom/solar-cell-operation/solar-cell-structure (accessed July 18, 2012).

[8] P. P. Altermatt, "Emitter and BSF profiles," Workshop on characterization and modeling of solar cells, May 2012, Tempe, Arizona, USA.

[9] K. Saga, "Gettering behavior of transition metals in low energy, high dose ion implanted silicon," *Solid State Phenomena*, vol. 187, pp. 283–286, 2012.

[10] Intel, "Intel 22nm 3-D Tri-Gate transistor technology," May 2011. http://newsroom.intel.com (accessed July 18, 2012).

[11] R. O. Jones and O. Gunnarsson, "The density functional formalism, its applications and prospects," *Reviews of Modern Physics*, vol. 61, no. 3, pp. 689–746, 1989.

[12] D. S. Sholl and J. A. Steckel, *Density functional theory a practical introduction.* Hoboken, N.J.: Wiley, 2009.

[13] G. Kresse and J. Hafner, "Abinitio molecular-dynamics for liquid-metals," *Phys. Rev. B*, vol. 47, no. 1, pp. 558–561, 1993.

[14] G. Kresse and J. Hafner, "Ab initio molecular-dynamics simulation of the liquid-metal-amorphous-semiconductor transition in germanium," *Physical Review B*, vol. 49, no. 20, p. 14251, 1994.

[15] G. Kresse and J. Furthmueller, "Efficiency of ab-initio total energy calculations for metals and semiconductors using a plane-wave basis set," *Computational Materials Science*, vol. 6, no. 1, pp. 15–50, 1996.

[16] G. Kresse and J. Furthmuller, "Efficient iterative schemes for ab initio total-energy calculations using a plane-wave basis set," *Phys. Rev. B*, vol. 54, no. 16, pp. 11169–11186, 1996.

[17] G. Kresse, M. Marsman, and J. Furthmuller, *VASP the GUIDE.* Computational Physics, Faculty of Physics, Universitšat Wien, Sensengasse 8, A-1130 Wien, Austria.

[18] H. J. Monkhorst and J. D. Pack, "Special points for Brillouin-zone integrations," *Phys. Rev. B*, vol. 13, no. 12, p. 5188, 1976.

[19] G. Henkelman, B. P. Uberuaga, and H. Jonsson, "A climbing image nudged elastic band method for finding saddle points and minimum energy paths," *J. Chem. Phys.*, vol. 113, no. 22, pp. 9901–9904, 2000.

[20] G. Henkelman and H. Jonsson, "Improved tangent estimate in the nudged elastic band method for finding minimum energy paths and saddle points," *Journal of Chemical Physics*, vol. 113, no. 22, pp. 9978–9985, 2000.

[21] A. F. Voter, "Introduction to the kinetic monte carlo method," in *Radiation Effects in Solids* (K. E. Sickafus and E. A. Kotomin, eds.), Dordrecht, The Netherlands: Springer, NATO Publishing Unit, 2005.

[22] E. Wigner *Z. Phys. Chem. B*, vol. 19, p. 203, 1932.

[23] R. Marcelin *Ann. Physique*, vol. 3, p. 120, 1915.

[24] H. Eyring, "The activated complex in chemical reactions," *J. Chem. Phys.*, vol. 3, p. 107, 1935.

[25] A. B. Bortz, M. H. Kalos, and J. L. Lebowitz, "New algorithm for Monte-Carlo simulation of Ising spin systems," *J. Comput. Phys.*, vol. 17, p. 10, 1975.

[26] A. Leon-Garcia, *Probability and random processes for electrical engineering.* Reading, Mass.: Addison-Wesley, 1994.

[27] R. Chen and S. T. Dunham, "Correlation factors for interstitial-mediated self-diffusion in the diamond lattice: Kinetic lattice Monte Carlo approach," *Physical Review B*, vol. 83, no. 13, p. 134124, 2011.

[28] H. Bracht, "Advanced dopant and self-diffusion studies in silicon," *Nucl. Instrum. Methods Phys. Res., Sect. B*, vol. 253, pp. 105–112, 2006.

[29] H. Bracht, H. H. Silvestri, I. D. Sharp, and E. E. Haller, "Self- and foreign-atom diffusion in semiconductor isotope heterostructures. II. Experimental results for silicons," *Phys. Rev. B*, vol. 75, p. 035211, 2007.

[30] A. Seeger and K. P. Chik, "Diffusion mechanisms and point defects in silicon and germanium," *Physica Status Solidi*, vol. 29, no. 2, pp. 455–&, 1968.

[31] U. Gosele and T. Y. Tan, "The nature of point defects and their influence on diffusion processes in silicon at high temperatures," in *Mat. Res. Soc. Symp. Proc.* (S. Mahajan and J. W. Corbett, eds.), vol. 14, pp. 45–59, 1983.

[32] P. Pichler, *Intrinsic point defects, impurities, and their diffusion in silicon.* Computational microelectronics, Wien; New York: Springer, 2004.

[33] K. Compaan and Y. Haven, "Correlation factors for diffusion in solids. Part 2. Indirect interstitial mechanism," *Trans. Faraday Soc.*, vol. 54, pp. 1498–1508, 1958.

[34] K. Compaan and Y. Haven, "Correlation factors for diffusion in solids," *Trans. Faraday Soc.*, vol. 52, no. 6, pp. 786–801, 1956.

[35] V. V. Voronkov and R. Falster, "Intrinsic point defects in silicon: a unified view from crystal growth, wafer processing and metal diffusion," in *Gettering and Defect Engineering in Semiconductor Technology XI* (B. Pichaud, A. Claverie, D. Alquier, H. Richter, and M. Kittler, eds.), vol. 108-109 of *Solid State Phenomena*, pp. 1–10, Zurich-Uetikon: Trans Tech Publications Ltd, 2005.

[36] M. Posselt, F. Gao, and D. Zwicker, "Atomistic study of the migration of di- and tri-interstitials in silicon," *Phys. Rev. B*, vol. 71, no. 24, p. 245202, 2005.

[37] M. Posselt, F. Gao, and H. Bracht, "Correlation between self-diffusion in Si and the migration mechanisms of vacancies and self-interstitials: An atomistic study," *Phys. Rev. B*, vol. 78, no. 3, p. 035208, 2008.

[38] B. Sahli and W. Fichtner, "Ab initio molecular dynamics simulation of self-interstitial diffusion in silicon," *Phys. Rev. B*, vol. 72, no. 24, p. 245210, 2005.

[39] J. P. Perdew, J. A. Chevary, S. H. Vosko, K. A. Jackson, M. R. Pederson, D. J. Singh, and C. Fiolhais, "Atoms, molecules, solids, and surfaces - applications of the generalized gradient approximation for exchange and correlation," *Phys. Rev. B*, vol. 46, no. 11, pp. 6671–6687, 1992.

[40] D. Vanderbilt, "Soft self-consistent pseudopotentials in a generalized eigenvalue formalism," *Phys. Rev. B*, vol. 41, no. 11, pp. 7892–7895, 1990.

[41] G. Kresse and J. Hafner, "Norm-conserving and ultrasoft pseudopotentials for first-row and transition-elements," *J. Phys. Condens. Matter*, vol. 6, no. 40, pp. 8245–8257, 1994.

[42] E. Koch and C. Wagner, "The mechanics of the ionic conduction in solid salts on the basis of imperfection perceptions I," *Z. Phys. Chem. B-Chem. Elem. Aufbau. Mater.*, vol. 38, no. 5, pp. 295–324, 1937.

[43] Y. Bar-Yam and J. D. Joannopoulos, "Barrier to migration of the silicon self-interstitial," *Phys. Rev. Lett.*, vol. 52, no. 13, pp. 1129–1132, 1984.

[44] P. E. Blochl, E. Smargiassi, R. Car, D. B. Laks, W. Andreoni, and S. T. Pantelides, "1st-principles calculations of self-diffusion constants in silicon," *Phys. Rev. Lett.*, vol. 70, no. 16, pp. 2435–2438, 1993.

[45] D. Caliste, P. Pochet, T. Deutsch, and F. Lancon, "Germanium diffusion mechanisms in silicon from first principles," *Phys. Rev. B*, vol. 75, no. 12, p. 125203, 2007.

[46] R. J. Needs, "First-principles calculations of self-interstitial defect structures and diffusion paths in silicon," *J. Phys. Condens. Matter*, vol. 11, no. 50, pp. 10437–10450, 1999.

[47] S. Goedecker, T. Deutsch, and L. Billard, "A fourfold coordinated point defect in silicon," *Phys. Rev. Lett.*, vol. 88, no. 23, p. 235501, 2002.

[48] S. Y. Ma and S. Q. Wang, "Ab initio study of self-diffusion in silicon over a wide temperature range: Point defect states and migration mechanisms," *Phys. Rev. B*, vol. 81, no. 19, p. 193203, 2010.

[49] R. Chen and S. T. Dunham, "Kinetic lattice monte carlo simulations of interdiffusion in strained silicon germanium alloys," *J. Vac. Sci. Technol., B*, vol. 28, no. 1, pp. C1G18–C1G23, 2010.

[50] G. Hock, E. Kohn, C. Rosenblad, H. von Kanel, H. J. Herzog, and U. Konig, "High hole mobility in $Si_{0.17}Ge_{0.83}$ channel metal-oxide-semiconductor field-effect transistors grown by plasma-enhanced chemical vapor deposition," *Appl. Phys. Lett.*, vol. 76, no. 26, pp. 3920–3922, 2000.

[51] C. W. Leitz, M. T. Currie, M. L. Lee, Z. Y. Cheng, D. A. Antoniadis, and E. A. Fitzgerald, "Hole mobility enhancements in strained $Si/Si_{1-y}Ge_y$ p-type metal-oxide-semiconductor field-effect transistors grown on relaxed $Si_{1-x}Ge_x$ (x $<$ y) virtual substrates," *Appl. Phys. Lett.*, vol. 79, no. 25, pp. 4246–4248, 2001.

[52] J. W. Jung, S. F. Yu, O. O. Olubuyide, J. L. Hoyt, D. A. Antoniadis, M. L. Lee, and E. A. Fitzgerald, "Effect of thermal processing on mobility in strained Si/strained $Si_{1-y}Ge_y$ on relaxed $Si_{1-x}Ge_x$ (x $<$ y) virtual substrates," *Appl. Phys. Lett.*, vol. 84, no. 17, pp. 3319–3321, 2004.

[53] J. D. Cressler and G. Niu, *Silicon-germanium heterojunction bipolar transistors*. Boston, MA: Artech House, 2003.

[54] S. Maine, D. M. Morini, L. Vivien, E. Cassan, and S. Laval, "Design optimization of a SiGe/Si quantum-well optical modulator," *J. Lightwave Technol.*, vol. 26, no. 5-8, pp. 678–684, 2008.

[55] J. E. Roth, O. Fidaner, R. K. Schaevitz, Y. H. Kuo, T. I. Kamins, J. S. Harris, and D. A. B. Miller, "Optical modulator on silicon employing germanium quantum wells," *Opt. Express*, vol. 15, no. 9, pp. 5851–5859, 2007.

[56] D. Marris, E. Cassan, and L. Vivien, “Response time analysis of SiGe/Si modulation-doped multiple-quantum-well structures for optical modulation,” *J. Appl. Phys.*, vol. 96, no. 11, pp. 6109–6112, 2004.

[57] M. Miyao, K. Nakagawa, N. Sugii, and S. Yamaguchi, “Atomically flat interface in SiGe/Si heterostructures formed by solid phase epitaxy: Significant increase in two-dimensional electron mobility,” *Microelectron. Eng.*, vol. 47, no. 1-4, pp. 221–223, 1999.

[58] C. W. Leitz, M. T. Currie, M. L. Lee, Z. Y. Cheng, D. A. Antoniadis, and E. A. Fitzgerald, “Hole mobility enhancements and alloy scattering-limited mobility in tensile strained Si/SiGe surface channel metal-oxide-semiconductor field-effect transistors,” *J. Appl. Phys.*, vol. 92, no. 7, pp. 3745–3751, 2002.

[59] M. T. Currie, C. W. Leitz, T. A. Langdo, G. Taraschi, E. A. Fitzgerald, and D. A. Antoniadis, “Carrier mobilities and process stability of strained Si n- and p-MOSFETs on SiGe virtual substrates,” *J. Vac. Sci. Technol. B*, vol. 19, no. 6, pp. 2268–2279, 2001.

[60] A. Benedetti, D. J. Norris, C. J. D. Hetherington, A. G. Cullis, D. J. Robbins, and D. J. Wallis, “Strain and Ge concentration determinations in SiGe/Si multiple quantum wells by transmission electron microscopy methods,” *J. Appl. Phys.*, vol. 93, no. 7, pp. 3893–3899, 2003.

[61] N. E. B. Cowern, P. C. Zalm, P. Vandersluis, D. J. Gravesteijn, and W. B. Deboer, “Diffusion in strained Si(Ge),” *Physical Review Letters*, vol. 72, no. 16, pp. 2585–2588, 1994.

[62] N. E. B. Cowern, W. J. Kersten, R. C. M. de Kruif, J. G. M. van Berkum, W. B. de Boer, D. J. Gravesteijn, and C. W. T. Buille-Liewma, “Interdiffusion mechanisms in coherently strained Si-Ge multilayers,” *Proceedings - Electrochemical Society*, vol. 96-4, no. Process Physics and Modeling in Semiconductor Technology, pp. 195–209, 1996.

[63] P. Fahey, S. S. Iyer, and G. J. Scilla, “Experimental-evidence of both interstitial-assisted and vacancy-assisted diffusion of Ge in Si,” *Appl. Phys. Lett.*, vol. 54, no. 9, pp. 843–845, 1989.

[64] B. P. Uberuaga, *Diffusion in semiconductors: A theoretical study.* PhD thesis, University of Washington, 2000.

[65] C. Ahn, *Atomic scale modeling of stress and pairing effects on dopant behavior in silicon.* PhD thesis, University of Washington, 2007.

[66] M. Diebel, *Application of ab-initio calculations to modeling of nanoscale diffusion and activation in silicon.* PhD thesis, University of Washington, 2004.

[67] C. Ahn, J. Song, and S. T. Dunham *Materials Research Society symposia proceedings.*, vol. 913, pp. 179–184, 2006.

[68] R. M. Jones, *Mechanics of composite materials.* Philadelphia, PA: Taylor & Francis, 1999.

[69] L. Boltzmann *Wiedemanns Ann. Physik*, vol. 53, p. 959, 1894.

[70] C. Matano, "On the relation between the diffusion-coefficients and concentrations of solid metals (the nickel-copper system)," vol. 8, pp. 109–113, 1933.

[71] P. Dierckx, "Algorithm/algorithmus 42 an algorithm for cubic spline fitting with convexity constraints," *Computing*, vol. 24, no. 4, pp. 349–371, 1980.

[72] M. Yoshida, "Numerical-solution of phosphorus diffusion equation in silicon," *Japanese Journal of Applied Physics*, vol. 18, no. 3, pp. 479–489, 1979.

[73] M. Yoshida, "Diffusion of phosphorus in silicon," *Japanese Journal of Applied Physics Part 1-Regular Papers Short Notes & Review Papers*, vol. 22, no. 9, pp. 1404–1413, 1983.

[74] D. Mathiot and J. C. Pfister, "Influence of the non-equilibrium vacancies on the diffusion of phosphorus into silicon," *Journal of Applied Physics*, vol. 53, no. 4, pp. 3053–3058, 1982.

[75] D. Mathiot and J. C. Pfister, "Dopant diffusion in silicon - a consistent view involving nonequilibrium defects," *Journal of Applied Physics*, vol. 55, no. 10, pp. 3518–3530, 1984.

[76] J. D. Plummer, M. D. Deal, and P. B. Griffin, *Silicon VLSI technology : fundamentals, practice, and modeling.* Upper Saddle River, NJ: Prentice Hall, 2000.

[77] S. Solmi, A. Parisini, R. Angelucci, A. Armigliato, D. Nobili, and L. Moro, "Dopant and carrier concentration in Si in equilibrium with monoclinic SiP precipitates," *Physical Review B*, vol. 53, no. 12, pp. 7836–7841, 1996.

[78] P. B. Griffin, S. W. Crowder, and J. M. Knight, "Dose loss in phosphorus implants due to transient diffusion and interface segregation," *Applied Physics Letters*, vol. 67, no. 4, pp. 482–484, 1995.

[79] G. Stingeder, "Determination of phosphorus distribution in the silicon dioxide silicon layer system by secondary ion mass-spectrometry," *Analytical Chemistry*, vol. 60, no. 15, pp. 1524–1529, 1988.

[80] P. Blood, "Capacitance-voltage profiling and the characterisation of III-V semiconductors using electrolyte barriers," *Semiconductor Science and Technology*, vol. 1, no. 1, pp. 7–27, 1986.

[81] R. B. Fair and G. R. Weber, "Effect of complex-formation on diffusion of arsenic in silicon," *Journal of Applied Physics*, vol. 44, no. 1, pp. 273–279, 1973.

[82] E. Guerrero, H. Potzl, R. Tielert, M. Grasserbauer, and G. Stingeder, "Generalized-model for the clustering of as dopants in si," *Journal of the Electrochemical Society*, vol. 129, no. 8, pp. 1826–1831, 1982.

[83] D. Nobili, S. Solmi, M. Merli, and J. Shao, "Deactivation kinetics in heavily arsenic-doped silicon," *Journal of the Electrochemical Society*, vol. 146, no. 11, pp. 4246–4252, 1999.

[84] K. C. Pandey, A. Erbil, G. S. Cargill, R. F. Boehme, and D. Vanderbilt, "Annealing of heavily arsenic-doped silicon - electrical deactivation and a new defect complex," *Physical Review Letters*, vol. 61, no. 11, pp. 1282–1285, 1988.

[85] M. Ramamoorthy and S. T. Pantelides, "Complex dynamical phenomena in heavily arsenic doped silicon," *Physical Review Letters*, vol. 76, no. 25, pp. 4753–4756, 1996.

[86] P. M. Rousseau, P. B. Griffin, W. T. Fang, and J. D. Plummer, "Arsenic deactivation enhanced diffusion: A time, temperature, and concentration study," *Journal of Applied Physics*, vol. 84, no. 7, pp. 3593–3601, 1998.

[87] Y. Takamura, S. H. Jain, P. B. Griffin, and J. D. Plummer, "Thermal stability of dopants in laser annealed silicon," *Journal of Applied Physics*, vol. 92, no. 1, pp. 230–234, 2002.

[88] Y. Takamura, P. B. Griffin, and J. D. Plummer, "Physical processes associated with the deactivation of dopants in laser annealed silicon," *Journal of Applied Physics*, vol. 92, no. 1, pp. 235–244, 2002.

[89] H. Wagner, A. Dastgheib-Shirazi, R. Chen, S. T. Dunham, M. Kessler, and P. P. Altermatt, "Improving the predictive power of modeling the emitter diffusion by fully including the phosphosilicate glass (psg) layer," in *37th IEEE Photovoltaic Specialists Conference*, 2011.

[90] C. S. Solanski, *Solar photovoltaics : fundamentals, technologies and applications.* New Delhi: PHI Learning, 2009.

[91] P. Negrini, D. Nobili, and S. Solmi, "Kinetics of phosphorus predeposition in silicon using $POCL_3$," *Journal of the Electrochemical Society*, vol. 122, no. 9, pp. 1254–1260, 1975.

[92] J. M. Eldridge and P. Balk, "Formation of phosphosilicate glass films on silicon dioxide," *Transactions of the Metallurgical Society of Aime*, vol. 242, no. 3, p. 539, 1968.

[93] Sciencelab.com, Inc., "Phosphorus oxychloride MSDS." https://www.sciencelab.com/msds.php?msdsId=9927394 (accessed July 18, 2012).

[94] B. E. Deal and A. S. Grove, "General relationship for the thermal oxidation of silicon," *Journal of Applied Physics*, vol. 36, no. 12, pp. 3770–3778, 1965.

[95] W. Shockley and J. Read, W. T., "Statistics of the recombinations of holes and electrons," *Physical Review*, vol. 87, no. 5, pp. 835–842, 1952.

[96] C. L. Reed and K. M. Mar, "The effects of abrasion gettering on silicon material with swirl defects," *Journal of the Electrochemical Society*, vol. 127, no. 9, pp. 2058–2062, 1980.

[97] R. S. Muller and T. I. Kamins, *Device electronics for integrated circuits.* New York: Wiley, 1986.

[98] K. Graff, *Metal impurities in silicon-device fabrication.* Berlin; New York: Springer-Verlag, 1995.

[99] J. S. Kang and D. K. Schroder, "Gettering in silicon," *Journal of Applied Physics*, vol. 65, no. 8, pp. 2974–2985, 1989.

[100] L. Baldi, G. Cerofolini, and G. Ferla, "Heavy-metal gettering in silicon-device processing," *Journal of the Electrochemical Society*, vol. 127, no. 1, pp. 164–169, 1980.

[101] E. J. Mets, "Poisoning and gettering effects in silicon junctions," *Journal of the Electrochemical Society*, vol. 112, no. 4, pp. 420–&, 1965.

[102] M. Aoki, T. Itakura, and N. Sasaki, "Gettering of iron impurities in p/p(+) epitaxial silicon-wafers with heavily boron-doped substrates," *Applied Physics Letters*, vol. 66, no. 20, pp. 2709–2711, 1995.

[103] J. L. Benton, P. A. Stolk, D. J. Eaglesham, D. C. Jacobson, J. Y. Cheng, J. M. Poate, N. T. Ha, T. E. Haynes, and S. M. Myers, "Iron gettering mechanisms in silicon," *Journal of Applied Physics*, vol. 80, no. 6, pp. 3275–3284, 1996.

[104] P. A. Stolk, J. L. Benton, D. J. Eaglesham, D. C. Jacobson, J. Y. Cheng, J. M. Poate, S. M. Myers, and T. E. Haynes, "The mechanism of iron gettering in boron-doped silicon," *Applied Physics Letters*, vol. 68, no. 1, pp. 51–53, 1996.

[105] T. M. Buck, C. M. Hsieh, J. M. Poate, and K. A. Pickar, "Gettering rates of various fast-diffusing metal impurities at ion-damaged layers on silicon," *Applied Physics Letters*, vol. 21, no. 10, pp. 485–&, 1972.

[106] F. Beeler, O. K. Andersen, and M. Scheffler, "Theoretical evidence for low-spin ground states of early interstitial and late substitutional 3d transition-metal ions in silicon," *Physical Review Letters*, vol. 55, no. 14, p. 1498, 1985.

[107] M. Yoshida and K. Saito, "Dissociative diffusion of nickel in silicon and self-diffusion of silicon," *Japanese Journal of Applied Physics*, vol. 6, no. 5, pp. 573–&, 1967.

[108] H. Kitagawa, "Diffusion and electrical properties of 3d transition-metal impurities in silicon," *Solid State Phenomena*, vol. 71, pp. 51–72, 2000.

[109] G. Kresse and D. Joubert, "From ultrasoft pseudopotentials to the projector augmented-wave method," *Physical Review B*, vol. 59, no. 3, pp. 1758–1775, 1999.

[110] P. E. Blochl, "Projector augmented-wave method," *Physical Review B*, vol. 50, no. 24, pp. 17953–17979, 1994.

[111] S. K. Estreicher, M. Sanati, and N. Gonzalez Szwacki, "Iron in silicon: Interactions with radiation defects, carbon, and oxygen," *Phys. Rev. B*, vol. 77, no. 12, p. 125214, 2008.

[112] J. Schon, M. C. Schubert, W. Warta, H. Savin, and A. Haarahiltunen, "Analysis of simultaneous boron and phosphorus diffusion gettering in silicon," *Phys. Status Solidi A-Appl. Mat.*, vol. 207, no. 11, pp. 2589–2592, 2010.

[113] T. C. Lovejoy, *III-VI Semiconductors and Oxides: Electronic Structure, Surface Morphology, and Transition Metal Doping of Ga_2Se_3, In_2Se_3, and Ga_2O_3*. PhD thesis, University of Washington, 2010.

[114] T. C. Lovejoy, R. Chen, X. Zheng, E. G. Villora, K. Shimamura, H. Yoshikawa, Y. Yamashita, S. Ueda, K. Kobayashi, S. T. Dunham, F. S. Ohuchi, and M. A. Olmstead, "Band bending and surface defects in β-Ga_2O_3," *Applied Physics Letters*, vol. 100, p. 181602, 2012.

[115] T. C. Lovejoy, R. Chen, E. N. Yitamen, V. Shutthanadan, S. M. Heald, E. G. Villora, K. Shimamura, S. Zheng, S. T. Dunham, F. S. Ohuchi, and M. A. Olmstead, "Incorporation, valence state, and electronic structure of Mn and Cr in bulk single crystal β-Ga_2O_3," *J. Appl. Phys.*, vol. 111, p. 123716, 2012.

[116] M. Orita, H. Ohta, M. Hirano, and H. Hosono, "Deep-ultraviolet transparent conductive β-Ga_2O_3 thin films," *Applied Physics Letters*, vol. 77, no. 25, pp. 4166–4168, 2000.

[117] J. H. Kim and K. H. Yoon, "Influence of post-deposition annealing on the microstructure and properties of Ga_2O_3: Mn thin films deposited by rf planar magnetron sputtering," *Journal of Materials Science-Materials in Electronics*, vol. 20, no. 9, pp. 879–884, 2009.

[118] Y. Tomm, J. M. Ko, A. Yoshikawa, and T. Fukuda, "Floating zone growth of β-Ga_2O_3: A new window material for optoelectronic device applications," *Solar Energy Materials and Solar Cells*, vol. 66, no. 1-4, pp. 369–374, 2001.

[119] K. Shimamura, E. G. Villora, K. Aoki, and N. Ichinose, "Growth and characterization of β-Ga_2O_3 single crystals as transparent conductive substrates for GaN," *Proceedings - SPIE the International Society for Optical Engineering*, vol. 5722, pp. 380–391, 2005.

[120] Z. G. Ji, J. Du, J. Fan, and W. Wang, "Gallium oxide films for filter and solar-blind UV detector," *Optical Materials*, vol. 28, no. 4, pp. 415–417, 2006.

[121] T. Oshima, T. Okuno, N. Arai, N. Suzuki, H. Hino, and S. Fujita, "Flame detection by a β-Ga_2O_3-based sensor," *Japanese Journal of Applied Physics*, vol. 48, no. 1, 2009.

[122] C. Baban, Y. Toyoda, and M. Ogita, "Oxygen sensing at high temperatures using Ga_2O_3 films," *Thin Solid Films*, vol. 484, no. 1-2, pp. 369–373, 2005.

[123] R. Moos, K. Sahner, M. Fleischer, U. Guth, N. Barsan, and U. Weimar, "Solid state gas sensor research in Germany - a status report," *Sensors*, vol. 9, no. 6, pp. 4323–4365, 2009.

[124] H. Ohno, A. Shen, F. Matsukura, A. Oiwa, A. Endo, S. Katsumoto, and Y. Iye, "(Ga,Mn)As: A new diluted magnetic semiconductor based on GaAs," *Applied Physics Letters*, vol. 69, no. 3, pp. 363–365, 1996.

[125] H. Ohno, "Making nonmagnetic semiconductors ferromagnetic," *Science*, vol. 281, no. 5379, pp. 951–956, 1998.

[126] S. Geller, "Crystal structure of β-Ga_2O_3," *Journal of Chemical Physics*, vol. 33, no. 3, p. 676, 1960.

[127] J. B. Varley, J. R. Weber, A. Janotti, and C. G. Van de Walle, "Oxygen vacancies and donor impurities in β-Ga_2O_3," *Applied Physics Letters*, vol. 97, no. 14, 2010.

[128] K. Yamaguchi, "First principles study on electronic structure of β-Ga_2O_3," *Solid State Communications*, vol. 131, no. 12, pp. 739–744, 2004.

[129] H. Y. He, R. Orlando, M. A. Blanco, R. Pandey, E. Amzallag, I. Baraille, and M. Rerat, "First-principles study of the structural, electronic, and optical properties of ga2o3 in its monoclinic and hexagonal phases," *Physical Review B*, vol. 74, no. 19, 2006.

[130] K. Bernhardt, M. Fleischer, and H. Meixner, "Breakthrough in gas sensors: Innovative sensor materials open up new markets," *Siemens Components*, vol. 30, no. 4, p. 35, 1995.

[131] E. G. Villora, K. Shimamura, Y. Yoshikawa, T. Ujiie, and K. Aoki, "Electrical conductivity and carrier concentration control in β-Ga_2O_3 by Si doping," *Applied Physics Letters*, vol. 92, no. 20, 2008.

[132] C. G. Van de Walle and J. Neugebauer, "First-principles calculations for defects and impurities: Applications to III-nitrides," *J. Appl. Phys.*, vol. 95, no. 8, pp. 3851–3879, 2004.

[133] H. Hayashi, R. Huang, H. Ikeno, F. Oba, S. Yoshioka, I. Tanaka, and S. Sonoda, "Room temperature ferromagnetism in Mn-doped γ-Ga_2O_3 with spinel structure," *Applied Physics Letters*, vol. 89, no. 18, 2006.

[134] R. Huang, H. Hayashi, F. Oba, and I. Tanaka, “Microstructure of Mn-doped γ-Ga_2O_3 epitaxial film on sapphire (0001) with room temperature ferromagnetism,” *Journal of Applied Physics*, vol. 101, no. 6, 2007.

[135] V. J. Folen, “Electron-spin-resonance spectrum of Mn^{2+} in β-Ga_2O_3,” *Physical Review*, vol. 139, no. 6A, pp. A1961–A1964, 1965.

[136] I. G. Kim, T. H. Yeom, S. H. Lee, Y. M. Yu, H. W. Shin, and S. H. Choh, “Electron paramagnetic resonance studies of Mn^{2+} ions in β-Ga_2O_3 single crystal,” *Journal of Applied Physics*, vol. 89, no. 8, pp. 4470–4475, 2001.

[137] G. Q. Pei, C. T. Xia, Y. J. Dong, B. Wu, T. Wang, and J. Xu, “Studies of magnetic interactions in Mn-doped β-Ga_2O_3 from first-principles calculations,” *Scripta Materialia*, vol. 58, no. 11, pp. 943–946, 2008.

[138] H. Wagner, S. Steingrube, B. Wolpensinger, A. Dastgheib-Shirazi, R. Chen, S. T. Dunham, and P. P. Altermatt, “Analyzing emitter dopant inhomogeneities at textured si surfaces by using 3D process and device simulations in combination with SEM imaging,” in *38th IEEE Photovoltaic Specialists Conference*, 2012.

VITA

- Education

  Ph.D. Electrical Engineering and Nanotechnology (dual), University of Washington, Seattle, WA, USA (2012).

  M.S. Applied Mathematics, University of Washington, Seattle, WA, USA (2011).

  B.S. Physics, Peking University, Beijing, China (2007).

- Journal publications

1. T. C. Lovejoy, R. Chen, et. al., "Incorporation and Valence State of Mn and Cr in Bulk Single Crystal β-Ga_2O_3," *J. App. Phys.* **111**, 123716 (2012)
2. T. C. Lovejoy, R. Chen, et. al., "Band Bending and Surface Defects in β-Ga_2O_3," *Appl. Phys. Lett.* **100**, 181602 (2012)
3. R. Chen, and S. T. Dunham, "Correlation factors for interstitial-mediated self-diffusion in the diamond lattice: Kinetic lattice Monte Carlo approach," *Phys. Rev. B* **83**, 134124 (2011)
4. S. E. Vasko, W. Jiang, R. Chen, R. Hanlen, J. D. Torrey, S. T. Dunham, and M. Rolandi, "Insights into Scanning Probe High-field Chemistry of Diphenylgermane," *Phys. Chem. Chem. Phys.* **13**, 4842 (2011)
5. R. Chen, and S. T. Dunham, "Kinetic Lattice Monte Carlo Simulations of Interdiffusion in Strained Silicon Germanium Alloys," *J. Vac. Sci. Technol. B* **28**, C1G18 (2010)

6. R. Chen, L. Wang, L. Lai, J. Lu, G. Luo, J. Zhou, and Z. Gao, "Stability, Electronic Structure, and Optical Property of Surface Passivated Silicon Nanowires: Density Functional Calculation," *J. Nanosci. Nanotechnol.* **9**, 1754 (2009)

- Conference presentations

1. R. Chen et. al., "Understanding Coupled Oxide Growth and Phosphorus Diffusion in $POCl_3$ Deposition for Control of Phosphorus Emitter Diffusion," in 38th IEEE Photovoltaic Specialists Conference, Austin, June 2012
2. S. T. Dunham, R. Chen, et. al., "Revisiting Models for Lifetime Degradation in Si Due to B/O Complexes," in 38th IEEE Photovoltaic Specialists Conference, Austin, June 2012
3. S. T. Dunham, B. Tryznadlowski, A. Yazdani, and R. Chen, "Coupled Modeling of Evolution of Impurity/Defect Distribution and Cell Performance," in 38th IEEE Photovoltaic Specialists Conference, Austin, June 2012
4. R. Chen and S. T. Dunham, "Kinetic Lattice Monte Carlo Simulations of Diffusion Processes in Si and SiGe Alloys," in Beyond Molecular Dynamics: Long Time Atomic-Scale Simulations International Workshop, Dresden, March 2012
5. H. Wagner, A. Dastgheib-Shirazi, R. Chen, et. al., "Improving the Predictive Power of Modeling the Emitter Diffusion by Fully Including the Phosphosilicate Glass (PSG) Layer," in 37th IEEE Photovoltaic Specialists Conference, Seattle, June 2011
6. B. C. Trzynadlowski, W. Jiang, R. Chen et. al., "Solar Cell Performance: From Process Recipe to Device Simulation," in 37th IEEE Photovoltaic Specialists Conference, Seattle, June 2011

7. S. Steingrube, H. Wagner, H. Hannebauer, S. Gatz, R. Chen et. al., "Loss Analysis and Improvement of Industrially Fabricated Cz-Si Solar Cells by Means of Process and Device Simulations," Silicon PV: 1st International Conference on Silicon Photovoltaics, Freiburg, April 2011

8. T. Ohrdesa, S. Steingrube, H. Wagner, C. Zechner, G. Letay, R. Chen, et. al., "Solar cell Emitter Design with PV-Tailored Implantation," Silicon PV: 1st International Conference on Silicon Photovoltaics, Freiburg, April 2011

9. S. T. Dunham and R. Chen, "Hierarchical Modeling for Ordered Binding of Peptides to Solid Surfaces," 8th Annual Conference on Foundations of Nanoscience: Self-assembled Architectures and Devices, 2011

10. T. C. Lovejoy, R. Chen, et. al, "Band Bending and Surface Defects in Ga_2O_3," AVS 57th International Symposium & Exhibition, Oct. 2010

11. R. Chen and S. T. Dunham, "Ab Initio Calculations of Crystalline and Amorphous In_2Se_3 Compounds for Chalcogenide Phase Change Memory," MRS Spring Meeting Symposium H, San Francisco, April 2010

12. R. Chen and S. T. Dunham, "Kinetic Lattice Monte Carlo Simulations of Diffusion in Strained Silicon Germanium Alloys," Proceeding of the International Workshop on INSIGHT in Semiconductor Device Fabrication, Metrology, and Modeling, 2009